12-1-2019

Baseline free structural health monitoring using modified time reversal method and wavelet spectral finite element models

Nimesh Jayakody

Recommended Citation

Jayakody, Nimesh, "Baseline free structural health monitoring using modified time reversal method and wavelet spectral finite element models" (2019). *Theses and Dissertations*. 850.
https://scholarsjunction.msstate.edu/td/850

Baseline free structural health monitoring using modified time reversal method and wavelet spectral finite element models

By

Nimesh Akalanka Jayakody

A Dissertation
Submitted to the Faculty of Engineering
Mississippi State University
in Partial Fulfillment of the Requirements
for the Degree of Doctor of Philosophy
in Aerospace Engineering
in the Department of Aerospace Engineering

Mississippi State, Mississippi

December 2019

Baseline free structural health monitoring using modified time reversal method and wavelet spectral finite element models

By

Nimesh Akalanka Jayakody

Approved:

Ratneshwar Jha
(Co-Major Professor)

Davy M. Belk
(Co-Major Professor)

Rani W. Sullivan
(Committee Member)

James C. Newman, Jr.
(Committee Member)

Dulip Samaratunga
(Committee Member)

David S. Thompson
(Graduate Coordinator)

Jason M. Keith
Dean
Bagley College of Engineering

Name: Nimesh Akalanka Jayakody

Date of Degree: December 13, 2019

Institution: Mississippi State University

Major Field: Aerospace Engineering

Major Professors: Ratneshwar Jha and Davy M. Belk

Title of Study: Baseline free structural health monitoring using modified time reversal method and wavelet spectral finite element models

Pages in Study: 156

Candidate for Degree of Doctor of Philosophy

The Lamb wave based, non-contact damage detection techniques are developed using the Modified Time Reversal (MTR) method and the model based inverse problem approach. In the first part of this work, the Lamb wave-based MTR method along with the non-contacting sensors is used for structural damage detection. The use of non-contact measurements for MTR method is validated through experimental results and finite element simulations. A novel technique in frequency-time domain is developed to detect linear damages using the MTR method. The technique is highly suitable for the detection of damages in large metallic structures, even when the damage is superficial, and the severity is low. In this technique, no baseline data are used, and all the wave motion measurements are made remotely using a laser vibrometer. Additionally, this novel MTR based technique is not affected due to changes in the material properties of a structure, environmental conditions, or structural loading conditions. Further, the MTR method is improved for two-dimensional damage imaging. The damage imaging technique is successfully tested through experimental results and finite element simulations.

In the second part of this work, an inverse problem approach is developed for the detection and estimation of major damage types experienced in adhesive joints. The inverse

problem solution is obtained through an optimization algorithm wherein the objective function is formulated using the Lamb wave propagation data. The technique is successfully used for the detection/estimation of cohesive damages, micro-voids, debonds, and weak bonds. Further, the inverse problem solution is separately obtained through a fully connected artificial neural network. The neural network is trained using the Lamb wave propagation data generated from a Wavelet Spectral Finite Element (WSFE) model which is computationally much faster than a conventional finite element model. This inverse problem approach technique requires a single point measurement for the inspection of the entire width of the adhesive joint. The proposed technique can be used as an automated quality assurance tool during the manufacturing process, and as an inspection tool during the operational life of adhesively bonded structures.

ACKNOWLEDGEMENTS

I am sincerely grateful to my dissertation adviser, Prof. Ratneshwar Jha, for giving me the opportunity to conduct research at the department of aerospace engineering in pursuit of my doctoral degree. Prof. Jha's constant encouragement and patience have successfully guided me through these years. I would like to thank to my academic adviser, Prof. Davy Belk for his support and guidance. I also gratefully acknowledge the advice and support I got from my dissertation committee members, Prof. Rani Sullivan, Prof. James Newman, and Dr. Dulip Samaratunga. Specially, I thank Dr. Samaratunga for his constant support.

I am grateful to my lab mates Ashkan Khalili, Prateek Jolly and Aniket Mote for their constant encouragement, discussions and friendship. I would like to thank Rodney Lincoln, Clay Shires, Jo McKenzie and Edward Skinner for their support during my time in Rapet Flight Research Laboratory at Mississippi State University.

I would like to thank my parents, and my sister for their steady support. Also, I would always appreciate the endless support from my wife Noupama being with me and helping me in many ways during my studies.

TABLE OF CONTENTS

CHAPTER

LIST OF TABLES

LIST OF FIGURES

CHAPTER I

INTRODUCTION

1.1 Structural health monitoring

The Structural Health Monitoring (SHM) evaluates the condition of structures through an interrogation process of data processing and interpretation. A general SHM process is comprised of four major steps [1]: determination that a damage is present in the structure, determination of the geometric location of the damage, qualitative (type) and quantitative (severity) estimation of the damage, and the prediction of the remaining operational life of the structure. The SHM systems are divided into two major categories as passive and active SHM systems. The passive SHM systems utilize the internal sensors (e.g.: fiber Bragg grating, strain gauges) and external sensors (e.g.: laser Doppler vibrometer) in order to measure various operational parameters of the structure. The measured parameters are then used for the calculation of the remaining life of the structure. For instance, strain gauges may be employed to record the stresses in a structure, and the cumulative fatigue damage due to the loading history is estimated. The number of loading cycles that the structure is able to withstand prior to a failure is then estimated. Contrastingly, the active SHM systems directly examine the structures for detection and estimation of possible damages. The structural health condition of the structure is then determined from the damage information obtained from the active SHM systems. The current practice of scheduled-based maintenance systems results unnecessary downtimes, early structural retirements, and sometimes, the catastrophic failures without early warnings [2]. On the other hand, the SHM systems offer a tremendous benefit in terms of life-cycle costs by detecting damages earlier and allowing a much more efficient maintenance schedule (condition-based maintenance). Therefore, SHM systems which are capable of detecting the structural damages, estimating the location and the severity of defects, are critically important for the cost-effective, continued safe operation of structures.

A number of structural interrogation techniques are being practiced in industry which include; the ultrasonic bulk wave methods, the magnet field methods, radiographs, the eddy-current methods, and the thermal field methods. A common disadvantage of aforementioned technique is that the vicinity of the damage is known a priori [3] and the damage vicinity should ready be accessible. Hence, these techniques are considerably expensive or/and time consuming.

On the other hand, the wave propagation and vibration characteristics-based interrogation techniques do not require a prior knowledge about the possible structural damages. The vibration characteristics such as the natural frequencies, the mode shapes, and the modal damping are profoundly governed by the physical properties of the structure (stiffness, mass distribution, and damping ratio). The changes of the vibration characteristics indicate the changes of the physical parameters. Therefore, the physical parameter variations are predicted from the variations of the vibration characteristics of structures. Given the fact that the vibration is a global phenomenon, the vibration based structural interrogation techniques generally reveal only the global-scale damages. On the other hand, both local-scale and global-scale structural damages influence the wave propagation along a wave guide (structure). The local damages may reflect and scatter the waves, and the global damages alter the wave propagation speed. Therefore, the wave propagation-based interrogation techniques are capable of detecting both local and global damages. Particularly, the ultrasonic guided waves gained much attention due to their long-range wave propagation with minimum attenuation.

1.2 Structural health monitoring using Lamb waves

1.2.1 Fundamentals of Lamb waves

The waves are the local disturbances that propagate in space as functions of time. Several wave types occur in an elastic medium, which include: the pressure waves, the shear waves, the flexural waves, the Rayleigh waves, and the Lamb waves. The shear waves are divided in to two categories: The Shear Vertical (SV) and the Shear Horizontal (or Love waves, discovered by Love in 1911). The Rayleigh and the Lamb waves are categorized under the Guided Waves (GW) which are guided by the traction free surfaces. Particularly, the Lamb waves, discovered by Horance Lamb in 1917, exist in elastic bodies which consist of two parallel free surfaces, (e.g. upper and lower surfaces of a plate). The Lamb waves are polarized, and the through thickness particle motion is elliptical with respect to the mid plane of the free surfaces. The Lamb exists in two distinct types depending upon the nature of the through- thickness particle motion; which are the Symmetric (S), and the Antisymmetric (A) waves. Each Lamb wave type has a number of unique wave modes. The symmetric wave modes designated with S_0, S_1, S_2…, whilst the Antisymmetric wave modes are designated with A_0, A_1, A_2 …. S_0 and A_0 are called the fundamental Lamb wave modes. As the wave mode number increases the through thickness particle motion tends to be more complex.

At lower frequencies, the *A₀* wave mode resembles the basic flexural wave of which the particle motion is purely transverse and perpendicular to the wave propagation direction. The *S₀* wave mode resembles the axial wave of which the particle motion is parallel to the wave propagation direction. The Lamb wave propagation is best described in terms of the dispersion relations given by the Rayleigh-Lamb equation. A complete derivation of Rayleigh – Lamb wave equation from 3D unbounded wave equation is presented in [4]. The Rayleigh-Lamb equation for antisymmetric and symmetric waves are given by Eq. (1.1) and Eq. (1.2), respectively.

$$\frac{\tan pd}{\tan qd} = -\frac{(\xi^2 - q^2)^2}{4\xi^2 pq} \tag{1.1}$$

$$\frac{\tan pd}{\tan qd} = -\frac{4\xi^2 pq}{(\xi^2 - q^2)^2} \tag{2.2}$$

$$p = \frac{\omega^2}{C_p} - \xi^2, q = \frac{\omega^2}{C_s} - \xi^2$$

$$C_p = \frac{\mu}{\rho}, C_s = \frac{\lambda + 2\mu}{\rho}$$

Where, $\boldsymbol{\mu}$, $\boldsymbol{\lambda}$, and $\boldsymbol{\rho}$ are the Lamé constants and the density of the wave guide. $\boldsymbol{d}$ is the half thickness of the plate, and **ω** is the angular frequency. The dispersion relations are obtained from the numerical solution of Eq. (1.1) and Eq. (1.2). Figure 1.1 presents the dispersion relations of an Aluminum wave guide (plate).

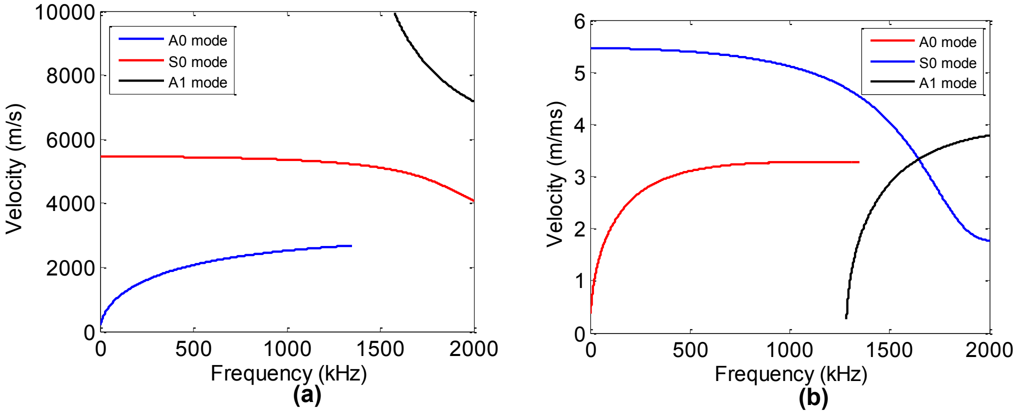

Figure 1.1 Dispersion curve for aluminum plate (a) group velocity (b) phase velocity

As illustrated in the figure, for each wave mode, the group velocity varies with the frequency-thickness product. Additionally, at least two wave modes co-exist for any given frequency.

The S_0 wave mode exhibit an approximately flat dispersion curve at low frequency-thickness values. Therefore, the S_0 wave mode is non-dispersive at low frequency-thickness values. Many SHM techniques employ S_0 wave modes for damage detections due to its non-dispersive nature at low frequencies. However, we used the A_0 wave mode (that is dispersive) because of its superiority sensitive for superficial damages compared to that of the S_0 wave mode.

1.2.2 Selection of suitable Lamb wave

The selection of a particular Lamb wave mode for a structural interrogation based on (1) dispersion, (2) attenuation, (3) sensitivity, (4) excitability, and (5) detectability [5] [6] characteristics of that particular Lamb wave mode. The dispersive nature of the Lamb waves distorts the overall shape of the wave as it propagates along a wave guide. The dispersion decreases the wave amplitude and consequently limits the wave propagation distance (useful). Further, the dispersion increases the time length of the wave and hence reduces the spatial resolution of damage detection.

The narrow bandwidth wave packets are widely used in order to minimize the wave dispersion. Generally, the bandwidth of a wave shrinks as the number of cycles increases, resulting a diminution of dispersion. On the other hand, having a large number of cycles widens the time-length of the wave, which decreases the spatial resolution of damage detection. Therefore, the selection of number of cycles should be a compromising between the signal's bandwidth and time length [5]. The attenuation of the Lamb waves is the reduction of wave amplitude with the distance it propagates. The Lamb waves exhibit considerably low attenuations compared to other wave types [4]. The Lamb wave are subjected to damping as it propagates through elastic mediums due to five main mechanisms: signal spreading due to dispersion, signal spreading due to beam divergence, material damping, scattering due to structural features and boundaries, and leakage in to surrounding media. Certain Lamb wave modes show higher attenuation compared to that of the other Lamb wave modes [5]. Therefore, a pre-inspection test is conducted to identify the best Lamb wave modes which have the lowest attenuations for the given structural configuration. The sensitivity of the Lamb wave modes to different damage types is crucial in the selection of a particular Lamb wave mode for damage detection. The through thickness Strain Energy Distribution (SED) of the Lamb wave modes determines the reflection and the transmission of Lamb wave through structural damages. For an example, the S_0 waves at low frequencies (approximates to axial waves) have fairy constant SED through the thickness. Therefore, the S_0 wave mode is more suitable for the through-thickness damage detection (e.g. a transverse crack). On the other hand, SED of the A_0 wave mode is concentrated at the free surfaces. Hence, A_0 wave mode is more suitable for the detection of surface defects (e.g. corrosion, surface cracks).

1.2.3 Actuation and sensing of Lamb waves

The ultrasonic transducers coupled with angle-adjustable Perspex wedges is one of the most popular and widely used technique, which generate straight crest Lamb waves. The same arrangement is employed to sense/capture the propagating Lamb waves. However, given the size and the complexity of the arrangement, the system under interrogation needs to be offline. The Laser-Based Ultrasonics (LBU) have also been commonly used for the excitation of the Lamb waves in thin structures. Here, a direct contact with the structure is not required, and therefore, this technique is more applicable for the structures with constricted accessibility. The Laser Dopplar Vibrometer (LDV) is widely used for the Lamb wave sensing. Similar to the LBU, the LDV offer non-contact sensing which is highly desirable for structures with less accessibility. Additionally, Electro Magnetic Acoustic Transducers (EMATs) are also utilized for the non-contact wave generations and measurements. Compared to the conventional sensing techniques, the LDV offers a significantly high spatial resolution, and is highly desirable in grid type inspection. Further, the LDVs yield a very high precision even for the wave measurements taken on curved surfaces or on complex structural features. Due its non-contact nature, the structure under interrogation does not necessarily need to be offline during the interrogation. All of the experimental works presented in this dissertation are conducted using LDV. Piezoelectric lead Zirconate Titanate (PZT) is the most commonly used transducer type for the Lamb wave generation and acquisition. Given its miniature nature, the PZTs are ideal to be permanently mounted to the host structure.

1.2.4 Signal processing for damage detection

The Lamb wave excitation and consequential signal acquisition are followed by a well-tailored signal processing method for an accurate interpretation of the captured wave signal. The interpretation of the captured signal may include the information about the presence of a damage, the damage severity, and the damage location. Many unique and diverse signal processing techniques have been reported in literature. However, the common signal processing techniques can be divided in to three major categories as time domain analysis, frequency domain analysis, and time frequency analysis. The time domain signal processing is the basic form of the signal processing. However, prior to any type of analysis, the captured wave signal may be fed through specific filers in order to cut-off any undesirable frequencies. Generally, the residual signal (error) which is the difference between the captured wave motion and the baseline (described in preceding chapter) is calculated. The damage details are then determined from the residual signal. However, the time domain analyses inherit many drawbacks including the fact that the damage detection resolution from the residual error decreases as the distance between the damage and the sensor increases. Additionally, time domain analyses are incapable of revealing the constituents of mixed signals. The time reversing method, which is discussed in a later section, has been limited to the time domain analysis. However, in this work, the time reversed signal is analyzed in frequency and frequency-time domain to extract more damage details. Frequency domain analyses involve the transformation of the captured wave motion data into the frequency domain by following an appropriate conversion method. The most popular and computationally efficient conversion method is the Fast Fourier Transformation (FFT). The frequency analyses reveal the hidden/dormant signals composed within the captured signals. These types of analyses are particularly suitable for the detection of the presence of non-linear damages where multipliers of the original wave frequency are observable. Depending upon the nature of the captured wave motion, the transformation may be extended to more than one dimension. For an example, in case where the spatially acquired wave signals (in time domain) are available, the transformation may be extended to two-dimensional Fourier transformation. The transformation results a three-dimensional complex matrix of which each value represents the spectral energy distribution in frequency- wave number domain. These analyses transform the entire wave signal into the frequency/wave-number domain. Therefore, localized (in time) frequency variations cannot separately be identified. The time-frequency analysis is the short-time version of the frequency analysis and is capable of exploring the instantaneous frequency distribution of wave signals. In time-frequency analysis, the wave signal (time signal) is broken down into pieces, and each piece is then transformed into the frequency domain.

CHAPTER II

MODIFIED TIME REVERSAL METHOD

2.1 Introduction

Most of the Lamb wave propagation based SHM systems compare the current wave propagation data with the baseline wave propagation data in order to determine the location, size, and the severity of possible damages. The baseline is the wave propagation data recorded in the structure in its pristine condition. However, the environmental conditions influence the Lamb wave propagation [7]. Generally, the structures operate under different environmental conditions. Therefore, recording of baseline data for every possible environmental condition is practically very difficult. The baseline-free SHM methods are therefore highly desirable [8] [9] [10].

The Time Reversal (TR) method is a widely used baseline-free damage detection technique, which requires no prior knowledge of the structure. In 1992, Fink [11] [12] introduced the TR method for the ultrasonic acoustic waves propagating in a lossless medium, in which the time reversal was utilized to refocus a pressure field emitted by a source, back to the original source location. Subsequently, the TR method has been implemented in a wide range of disciplines including the active sonar, medical imaging, and nondestructive testing [13] [14]. Ing et al. [15] [16] showed that the TR method is also applicable for the Lamb waves regardless of their dispersive nature and demonstrated the use of the TR method for flaw detection. The structural transfer function for a two dimensional plate with a finite size actuator was formulated using Mindlin plate theory [17], and thereby the time reversal operator was derived [18]. Wang et al. [18] utilized the TR method for damage imaging and showed that TR method does not effectively work for the broad-band signals due to the frequency-dependency of the time reversal operator (which was later experimentally demonstrated using the TR of a broad-band Gaussian pulse [19]). The Lamb waves are multi-modal in nature, and the existence of more than one wave mode complicates the TR process [20]. The appearance of multiple wave packets in the reconstructed waveform was shown theoretically [21] and experimentally [14]. Moreover, the structural boundaries hinder the use of the TR method considerably, and additional wave packets appear on the reconstructed waveform due to the reflections [14] and the mode conversions at the structural boundaries.

Park et al. [22] utilized the TR method for damage detection in composite plates in which a narrow-band, Morlet waveform was utilized in order to overcome the frequency-dependency of the TR operator. Xu et al. [21] experimentally demonstrated that as the number of cycles of a Hanning-windowed tone burst increases, the similarity index (indicating the ability of time reconstruction) increases considerably regardless of the number of wave modes present. Xu et al. [21] utilized the mode tuning process to minimize the multi-modal effects. The dominant frequency bandwidth of each wave mode, which depends on the actuator dimensions, were determined from the wave response. The TR process was then performed only within a prescribed frequency range in which a single wave mode is prevailing.

In the TR methods, Damage Indices (DI) are defined based on the time domain comparison between the excitation waveform and the reconstructed waveform. The DIs are used for the prediction of the presence of a damage, damage location, and its severity [20]. The DIs are better for the non-linear damages of which the transfer function is non-linear. Therefore, the DIs obtained from TR method cannot readily be used for the detection of linear structural damages (e.g. holes) which do not introduce nonlinearity to the system. Gangadharan et al. [19] experimentally demonstrated that the TR DIs do not exhibit a noticeable correlation with the damage size (for a notch type damage). In contrast, the structural damages which introduce significant nonlinearity to the system, such as an impact damage on a composite panel, profoundly correlate with the DI values [23].

The size or the shape of the actuator do not influence the TR process [14], and therefore, the Lamb waves generated by a damaged (e.g. cracked) actuator can be fully reconstructed [24]. However, a debond between an actuator and the host structure behaves like a nonlinear damage and distorts the TR process. The debond creates a kissing bond between the actuator and the host structure and produces the harmonics of the excitation frequency. Lee et al. [24] utilized this characteristic for the identification of debonds of an actuator. Further, the temperature effects have been shown to be considerably small on reconstruction process [24]. The TR method has also been used for the inspection of complex structures such as the stiffened composite panels [25] and the structural joints [25] [26] [27] [28]. Cai et al. [29] introduced the Virtual Time Reversal (VTR) method. Unlike the conventional TR method which requires dual excitation and reception, the VTR requires only a single excitation at the actuator and a single reception at the sensor which significantly reduces the instrumentation requirements. Lui et al. [30] utilized VTR along with air-coupled actuators and sensors for damage imaging of a composite plate.

Watkins and Jha [23] introduced a Modified Time Reversal (MTR) method that requires a single actuator and a single sensor, for each signal path. The signal path is defined as the shortest line between the sensor and the actuator. Unlike the conventional TR method, the MTR method does not require the sensors to work as actuators. Therefore, the MTR method improves the practical applicability of the TR concept by significantly reducing the hardware associated with actuation (signal generator, waveform amplifiers, wirings, etc.), and hence, reduces the cost of inspection. Additionally, the MTR allows the use of non-contact sensing techniques such as a Laser Doppler Vibrometer (LDV). Use of non-contact sensing enables long-range remote sensing, flexibility in measurements, and higher spatial resolution. Therefore, SHM of large structures, such as wind turbines, storage tanks, and etc. can be performed remotely, safely and efficiently through the MTR method. For example, Polytech RSV-150 remote sensing LDV is capable of measuring vibration/wave motions from up to 300m distance [31] which is ideal for the inspection of large structures. Additionally, complex structural features (curved surfaces) can be inspected very efficiently using non-contact measuring techniques.

This chapter consists of three main sections. In the first section, we introduce the MTR method using non-contacting sensing (laser vibrometer). A detailed analysis of MTR using laser vibrometer measurements is conducted in this section. The purpose this section is to provide the reader with the necessary theoretical background of MTR using non-contact measuring technique. The second part of this chapter focuses on the complexities in the MTR method arising from multi-modal Lamb wave characteristics and structural boundary reflections. Although some qualitative results covering these aspects for the conventional TR method are available in the published literature, quantitative investigations covering the MTR method have not been reported. The purpose of this section is to highlight the complexities arising from various factors and provide the means to quantify and minimize them.

Damage indices are used to determine the severity of damages by comparing the excitation and reconstructed signal in the time domain. The conventional TR method along with the damage index calculations is incapable to detect the damages which replicate certain structural features (e.g., a hole). Gangadharan et al. [19] experimentally showed that a notch type damage in a metallic structure does not break of time reversibility of Lamb waves. Additionally, the reconstructed signals obtained from the conventional TR failed to exhibit notable changes as the size of the damage varied. In contrast, the DI values show good correlation with the non-linear structural damages such as an impact damage on a composite panel [23]. This is a major disadvantage of the conventional TR method. In the third section, we introduce a novel technique to overcome this limitation. Therefore, we expand MTR capabilities for generic damage detection (linear and non-linear damages).

2.2 Modified time reversal method

Watkins and Jha [23] introduced the MTR method which requires a single actuator and a single sensor, for a given signal path. The conventional TR method and the MTR method were compared, and a minimum of 89.2% of similarity between the reconstructed waveforms using the two methods were observed [23]. Moreover, a theoretical analysis performed in the frequency domain proved that the excitation signal is fully reconstructed by the MTR method. To implement the MTR method for damage detection, the actuator and the sensor should be arranged in pitch-catch configuration. The process is composed of six steps as given below [23] [2] and the modified steps are shown in bold letters.

1. A narrow-banded wave is excited at an actuator at the location ***A***. This step initiates the “first-sensing cycle.”
2. A sensor at the location ***B*** records the resulting wave motion. This step completes the “first-sensing cycle.”
3. The recorded signal is then time reversed (i.e. $v_B(t) \rightarrow v_B(-t)$).
4. **The time-reversed signal is excited at *A* and response is recorded at *B*. This step initiates the “second-sensing cycle.”** In contrast in conventional TR method, the time-

reversed is excited at ***B***. Therefore, in conventional TR method each transducer should work as sensor as well as an actuator.

5. **The recorded signal at *B* is then time reversed. The resulting signal is called "reconstructed waveform." This step concludes the "second-sensing cycle."** In conventional TR method, the signal is captured at ***A***.
6. Finally, the reconstructed signal and the excitation signal are used for DI calculation (signals are normalized using their peak amplitudes.)

The steps involved in the MTR method is illustrated in Figure 2.1.

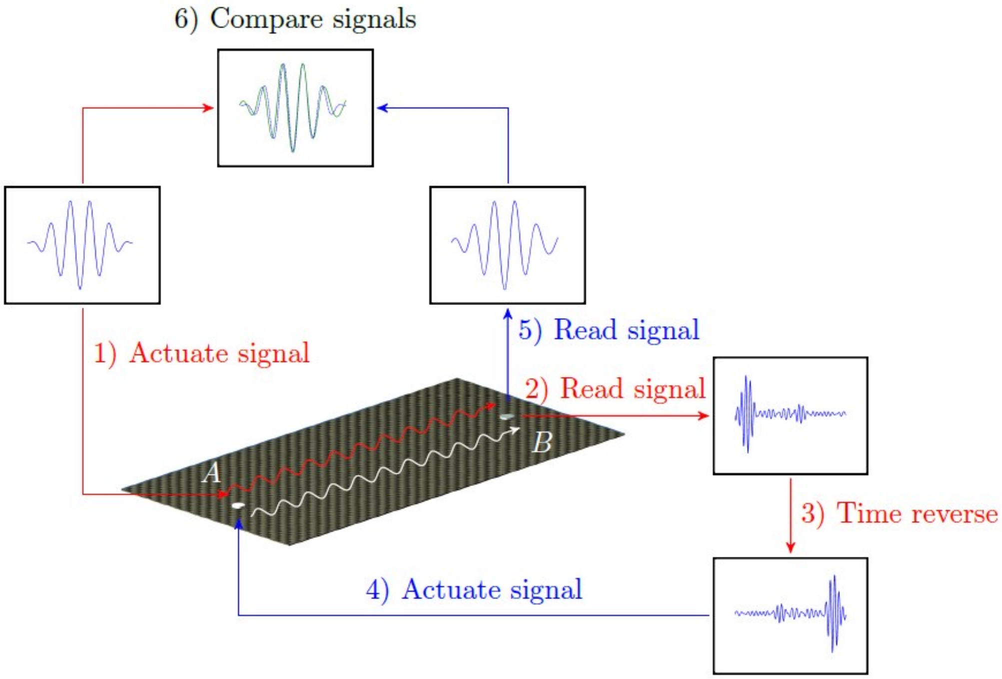

Figure 2.1 Steps involved in the MTR method

2.3 MTR method using laser doppler vibrometer as sensor

The concept of the time reversal of the Lamb waves has been developed and evolved by using the permanently bonded piezoelectric transducers and/or air coupled actuators/sensors [15] [30]. Similarly, the MTR method has also been developed by utilizing the permanently bonded piezoelectric transducers [23]. When piezoelectric transducers are being employed as sensors, the output signal is generated proportional to the average strain in the bonded area [32]. In contrast, the LDV measures the displacement, velocity, or the acceleration at a single point. The use of LDVs as sensor offers a higher spatial resolution, provides flexibility due to non-contact nature of measurements, and adds remote sensing capabilities. The use of LDVs for the MTR method involves the same steps given in above section .The transverse velocity is measured at point ***B*** (instead of strains) in steps 2 and 5. A frequency domain analysis of the MTR method using the transverse velocity as the type of measurement is given below.

Eq. (2.1) formulates the response $I_A(\omega)$ at location ***A*** due to the voltage signal $V_A(\omega)$ supplied to the piezoelectric actuator. In Eq. (1), $K_{PZT}(\omega)$ is the transfer function of the piezoelectric actuator. $K_{PZT}(\omega)$ is generally considered to be frequency-invariant, however, it tends to be frequency-dependent at the higher frequencies due to the inertia effects [14]. The response at ***B***, $I_B(\omega)$ due to $I_A(\omega)$ is given by Eq (2), where $G_{Vel}(\omega)$ is the structural transfer function. Note that the structural transfer function, $G_{Vel}(\omega)$ is analogous to, but not equivalent to, the structural transfer function derived for strain measurements in ref. [17]. As shown below, the structural transfer function $G_{Vel}(\omega)$ is not only frequency dependent, but also measurement-type dependent.

$$I_A(\omega) = K_{PZT}(\omega) V_A(\omega) \tag{2.1}$$

$$I_B(\omega) = G_{Vel}(\omega) I_A(\omega) = K_{PZT}(\omega) G_{Vel}(\omega) V_A(\omega) \tag{2.2}$$

The reading of LDV measured at point ***B***, $V_{B-vel}(\omega)$ is given in Eq. (2.2). $K_{LDV}(\omega)$ is the transfer function of LDV, and if scaling is not performed, the value of $K_{LDV}(\omega)$ equals unity.

$$V_{B-vel}(\omega) = K_{LDV}(\omega) I_B(\omega) = K_{LDV}(\omega) K_{PZT}(\omega) G_{Vel}(\omega) V_A(\omega) \tag{2.3}$$

The recorded signal is time-reversed ($v_{B-vel}(t) \rightarrow v_{B-vel}(-t)$), and the time-reversed signal in frequency domain is indicated by $V^{*}_{B-vel}(\omega)$. Here, $V^{*}_{B-vel}(\omega)$ is the complex conjugate of $V_{B-vel}(\omega)$. The time-reversed signal is supplied to the actuator, and the resulting response at ***A***, $\hat{I}_A(\omega)$ is given by Eq. (2.4). The response at ***B***, $\hat{I}_B(\omega)$ due to $\hat{I}_A(\omega)$ is given by Eq. (2.5) and LDV reading is given by (2.6).

$$\hat{I}_A(\omega) = K_{PZT}(\omega) V^{*}_{B-vel}(\omega) \tag{2.4}$$

$$\hat{I}_B(\omega) = G_{Vel}(\omega) \hat{I}_A(\omega) \tag{2.5}$$

$$\hat{V}_{B-Vel}(\omega) = K_{LDV}(\omega) \hat{I}_B(\omega) = K_{LDV}(\omega) K_{PZT}(\omega) G_{Vel}(\omega) V^{*}_{B-Vel}(\omega) \tag{2.6}$$

Finally, the recorded signal is time-reversed to obtain the reconstructed signal $V_R(\omega)$ as given by Eq. (2.7).

$$V_R(\omega) = \hat{V}^{*}_{B}(\omega) = \left|K^{2}_{PZT}(\omega)\right| \left|K^{2}_{LDV}(\omega)\right| \Gamma(\omega) V_A(\omega) \tag{2.7}$$

$$\left|K^{2}_{PZT}(\omega)\right| = K_{PZT}(\omega) K^{*}_{PZT}(\omega), \quad \left|K^{2}_{LDV}(\omega)\right| = K_{LDV}(\omega) K^{*}_{LDV}(\omega) \text{ and}$$

$$\Gamma(\omega) = \left|G_{Vel}{}^{2}(\omega)\right| = G_{Vel}(\omega) G_{Vel}{}^{*}(\omega)$$

Note that $\left|K^{2}_{PZT}(\omega)\right|$ and $\left|K^{2}_{LDV}(\omega)\right|$ are frequency invariant, especially in low frequencies. However, the time reversal operator $\Gamma(\omega)$ is frequency dependent. However, $\Gamma(\omega)$

is assumed to be a constant over the narrow frequency bandwidths (<10 kHz). If a narrow-band signal is employed, the reconstructed waveform, $V_R(\omega)$ has an identical shape (envelop) to the excitation signal $V_A(\omega)$. Finally, the reconstructed time signal $v_R(t)$ is given by Eq. (2.8).

$$v_R(t) = \int_{-\infty}^{\infty} \left|K^2_{PZT}(\omega)\right|\left|K^2_{LDV}(\omega)\right| \Gamma(\omega) V_A(\omega) dt \tag{2.8}$$

Though $V_R(\omega)$ and $V_A(\omega)$ have identical spectral energy distribution envelops, the reconstructed time signal $v_R(t)$ is not equal to the excitation signal $v_A(t)$. The main wave packet which contains the most of energy of the reconstructed wave [14], is equal to $v_A(t)$, after scaling.

2.3.1 Frequency dependency of the structural transfer function

The frequency-dependency of the structural transfer function for strain measurements has been discussed by several researchers [14] [21]. When employing a narrow-band excitation, this frequency-dependency can be neglected. In this section, we analyze the frequency dependency of the structural transfer function for transverse velocity measurements. To demonstrate the frequency-independence of the structural transfer function for transverse velocity measurements, experimental measurements and Finite Element (FE) simulations are performed. For both experiment and FE simulation, a 3.5 cycle, 70 kHz tone burst voltage signal was supplied to a piezoelectric actuator permanently bonded on a 1.2 mm thick aluminum plate. The material properties of the piezoelectric actuator and the aluminum plate are given in Table 2.1. The experimentally reconstructed signal using the transverse velocity is shown in Figure 2.2 (a) and the spectral energy of the velocity signal captured during the first sensing cycle is shown in Figure 2.2 (b). The spectral energy distribution of transverse velocity is almost identical to the excitation signal (voltage input to piezoelectric transducer), implying that the structural transfer function is linear within the signal bandwidth. Therefore, for narrow band signals, the structural transfer function for transverse velocity measurements can be considered to be frequency-invariant, and consequently, does not distort reconstruction of the excitation signal. However, the transverse acceleration energy spectrum shows differences with excitation spectrum, which is explained in the next section.

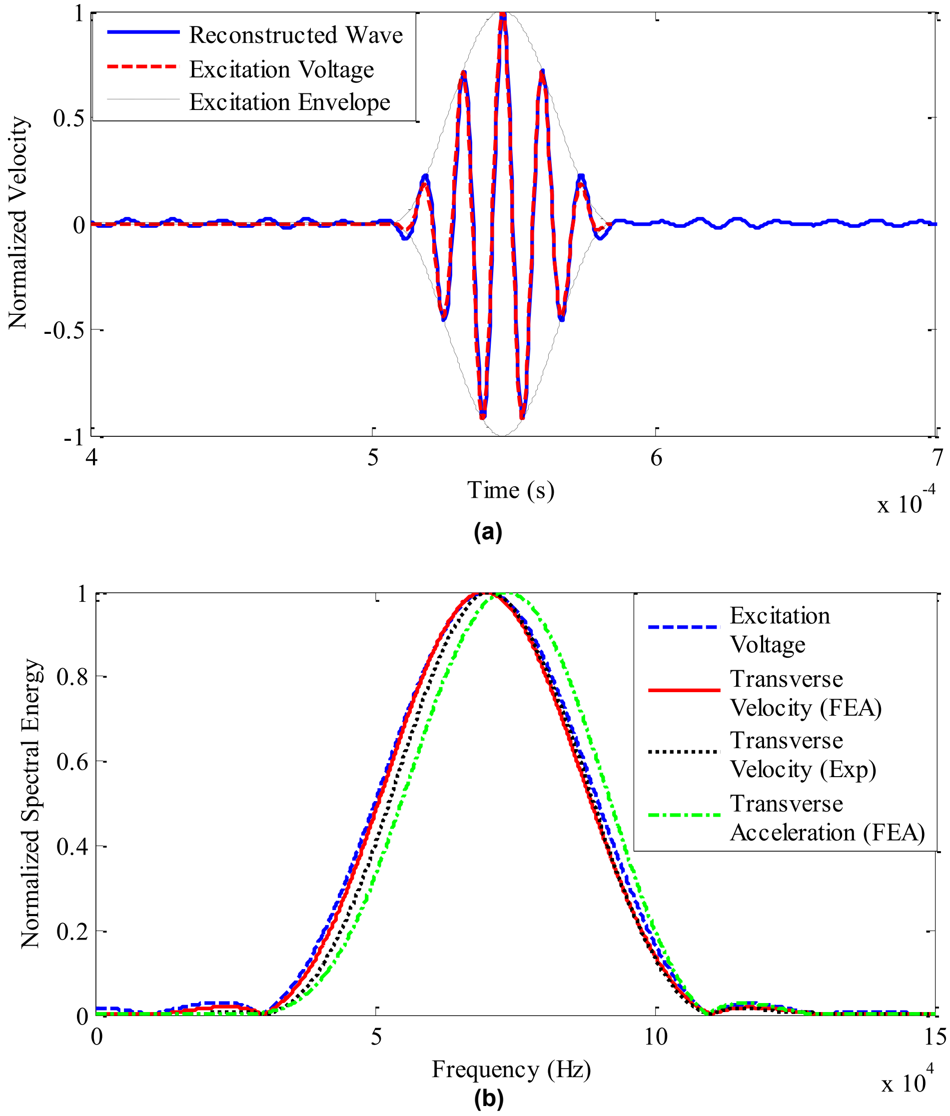

Figure 2.2 (a) Time reversed signal using transverse velocity as the measurement. The excitation signal is 3.5 cycle, 70kHz tone burst. (b) spectral energy of transverse velocity, transverse acceleration and excitation voltage

2.3.2 Measurement dependency of the structural transfer function

The use of LDV as sensor permits the acquisition of displacement, velocity and acceleration at any point on a structure. These quantities are related to each other; however, it is crucial to identify the most suitable measurement for the MTR method. In the previous section, it was shown that the transverse velocity has a nearly linear transfer function. Let us now consider the structural transfer functions for the transverse acceleration and transverse displacement. Eq. (2.3) is re-written for acceleration measurements, $V_{B-acl}(\omega)$ as

$$V_{B-acl}(\omega) = K_{LDV}(\omega)K_{PZT}(\omega)G_{Acl}(\omega)V_A(\omega) \tag{2.9}$$

Where $G_{Acl}(\omega)$ is the structural transfer function for transverse acceleration measurements. The time derivative of velocity data measured by LDV ($v_{B-vel}(t)$), equals acceleration measurements (v_{B-acl}) given in Eq. (2.10) and (2.11).

$$\frac{dv_{B-vel}(t)}{dt} = v_{B-acl}(t) \tag{2.10}$$

$$V_{B-acl}(\omega) = \int_{-\infty}^{\infty} v_{B-acl}(t)e^{i\omega t}dt = \int_{-\infty}^{\infty} \frac{dv_{B-vel}(t)}{dt}e^{i\omega t}dt \tag{2.11}$$

The term $V_{B-acl}(\omega)$ is rewritten as Eq. (2.12), wherein the first term on the right-hand side vanishes.

$$V_{B-acl}(\omega) = \left[v_{B-vel}(t)e^{i\omega t}\right]_{-\infty}^{+\infty} + i\omega V_{B-vel}(\omega) \tag{2.12}$$

Therefore, the relation between the structural transfer function for velocity $G_{Vel}(\omega)$ and the structural transfer function for the acceleration measurements $G_{Acl}(\omega)$ is given by Eq. (2.13) and Eq. (2.14).

$$G_{Acl}(\omega) = i\omega G_{Vel}(\omega) \tag{2.13}$$

$$|G_{Acl}(\omega)| = \omega |G_{Vel}(\omega)| \tag{2.14}$$

$G_{Vel}(\omega)$ was previously shown to be a constant over narrow frequency bandwidths. Eq. (13) and (14) clearly show the frequency dependency of $G_{Acl}(\omega)$, and this is illustrated in Figure 2.2 (b). Consequently, the central frequency is shifted to the right. The relationship between the structural transfer function for displacement measurements $G_{Dsp}(\omega)$ and $G_{Vel}(\omega)$ is given in Eq. (2.15) and Eq. (2.16).

$$G_{Dsp}(\omega) = \frac{-i}{\omega} G_{Vel}(\omega) \tag{2.15}$$

$$|G_{Dsp}(\omega)| = \frac{1}{\omega} |G_{Vel}(\omega)| \tag{2.16}$$

In Eq. (2.15) and (2.16), the higher frequencies are damped more than the lower frequencies, and the central frequency moves to the left. Therefore, given the considerable linearity of its transfer function, the transverse velocity is the most suitable measurement type for MTR method.

2.3.3 Damage index

The DIs are used to determine the presence, location, and severity of damages by comparing the excitation signal and the reconstructed signal in time domain. Generally, amplitude normalization is performed for both signals prior to DI computation. When multiple modes and boundary effects are present (that is more than one wave packet is visible in the reconstructed signal), the main wave packet is used for DI computation [14]. Here, two methods to calculate DIs are used as in our works [23] [2]. Both damage indices focus on shift in frequency and change in the overall shape of the reconstructed signal with respect to the excitation signal. The DIs are defined by Eq. (2.17) and (2.18).

$$DI_{sp} = 1 - \sqrt{\left[\int_{t_1}^{t_2} v_A(t) v_R(t) dt\right]^2 \Big/ \int_{t_1}^{t_2} v_A(t)^2 dt \int_{t_1}^{t_2} v_R(t)^2 dt} \tag{2.17}$$

$$DI_{L2} = \sqrt{\sum_N \left[v_R(t) - v_A(t)\right]^2 \Big/ \sum_N \left[v_A(t)\right]^2} \tag{2.18}$$

$v_A(t)$ is the excitation signal and $v_R(t)$ is the reconstructed signal. The terms t_1 and t_2 indicate the time interval between which the signals are compared. Based on this definition, DI_{sp} =0 indicates identical signals whereas DI_{sp}=1 represents very dissimilar signals. Higher DI values indicate the presence of damages and the DI values increase with the damage severity since the large damage introduces large non-linearity resulting a reconstructed waveform much dissimilar to the excitation signal. Similarly, DI_{L2}=0 indicates identical signals whereas DI_{L2} =1 represents very dissimilar signals. However, the multi-modal and boundary effects complicate the DI calculation, often leading to produce inaccurate results. Minimizing the multi-modal and boundary effects are discussed in following sections.

2.4 Modified time reversal method for damage detection

This section presents the experimental works conducted to determine the location of delamination of a composite fan blade using MTR method along with the transverse velocity as measurement. According to authors' knowledge, this is the first time that MTR method is used along with the LDV [2].

2.4.1 Experimental setup

The experimental set-up comprises a commercial engine fan blade (approximately 1250 x 600 x 17 mm) with two surfaces bonded PTZ disc transduces. The fan blade initially had a delamination and the delamination is visible from topside of the fan blade as shown in Figure 2.3. The depth of the delamination from the top of the fan blade is determined using a 0.038mm feeler gauge. Two PTZs are permanently bonded to the fan blade using epoxy adhesive. The transducers have dimensions of 12mm diameter and 0.5mm thickness. The excitation wave is generated by Agilent 33220A function/arbitrary waveform generator (10Vpp) and consequently amplified by A.A Lab Systems' A303 high voltage amplifier and modulator (up to 200Vpp). A LDV (Polytec OFV – 5000 with OFV – 500 laser head) is used to acquire the wave motion at equidistance points (10 mm apart) (Figure 2.4). The sampling frequency of the LDV is set to 2560 kHz and a low-pass frequency filter (200 kHz) is employed in reduces the high frequency noises. For each sensing location, the signals are recorded fifty times and then averaged. The experimental set up is shown in Figure 2.5.

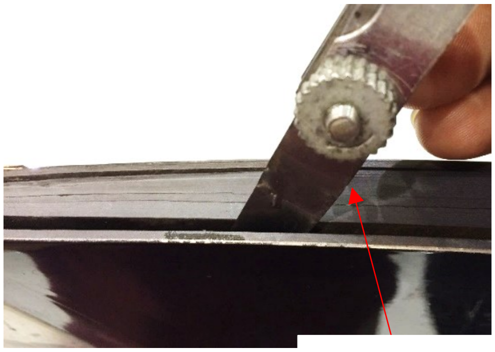
Feeler gauge

Figure 2.3 Delamination on the fan blade

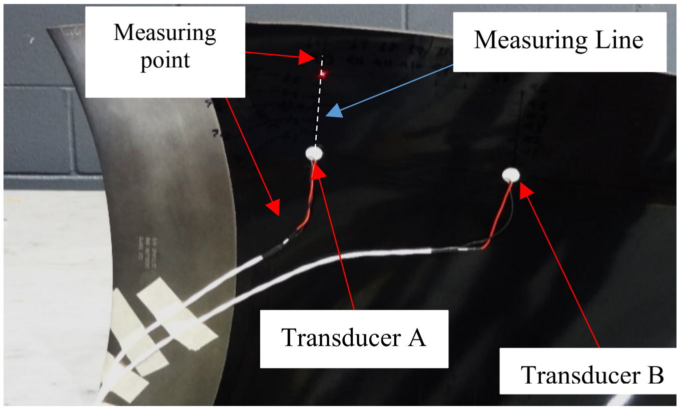

Figure 2.4 Fan blade

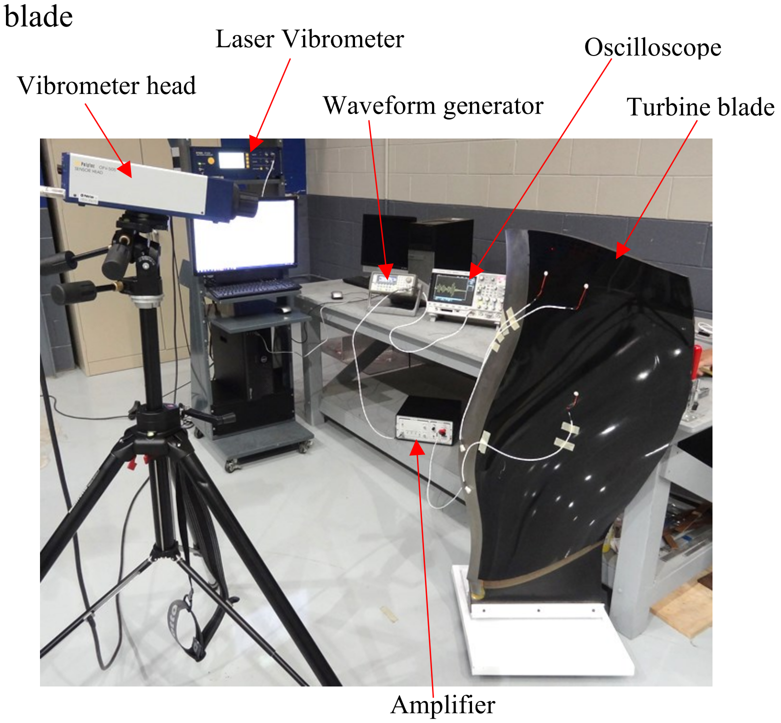

Figure 2.5 Experimental set up

2.4.2 Mode tuning

Due to the relative high thickness of the fan blade, the Lamb wave amplitude (transverse velocity) are considerably low which led to a decreased signal to noise ratio. Therefore, the system (fan blade with the piezoelectric transducers) is mode-tuned in order to obtain a better wave amplitude. It is shown that, at low frequencies, the amplitude of the asymmetric Lamb waves is considerably higher compared to that of the symmetric waves. The amplitude of the asymmetric Lamb waves increases with the excitation frequency up to a certain frequency level. At higher excitation frequencies, the amplitude of the asymmetric waves tends to decrease, while amplitude of the symmetric waves increases [3]. Signal to noise ratio is a crucial factor which affect the time reversibility; therefore, it is very important to use an optimum frequency which produces the highest amplitude. The transducer ***A*** (Figure 2.5) is excited with different excitation frequencies and the resulting wave motion at the point ***6*** is recorded. The maximum wave amplitude is then plotted against the excitation frequency. Figure 2.6 shows the results of the mode tuning process. The Lamb wave inherits the multimodal and dispersive characteristics. Therefore, time reversibility of high frequency excitation can be extremely difficult since multiple modes become evident as the excitation frequency increases. Thus, the peak with the lowest frequency is selected as the optimum frequency.

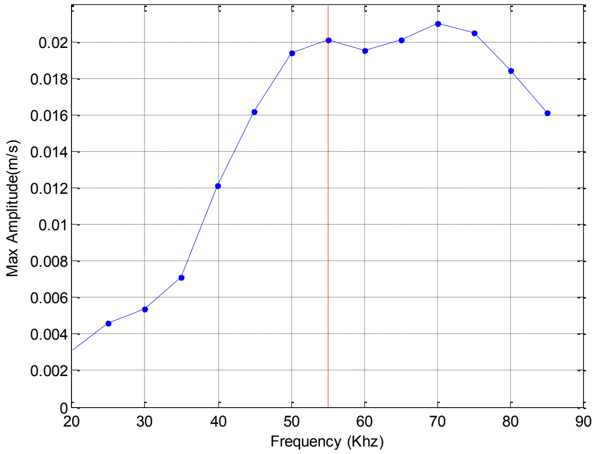

Figure 2.6 Mode tuning results

2.4.3 Delamination detection

Figure 2.7 shows the transducer locations, the measurement points and the signal paths. Six equidistance sensing points are marked on the fan blade (10 mm apart). A 55 kHz, 5.5 tone burst signal is excited with transducer ***A*** and the response is recorded at point ***1***. The recorded signal is time- reversed and re-emitted from transducer ***A***, and the response for the time reversed signal is captured at point ***1***. This procedure is repeated for the rest of points from point ***2*** through point ***6***. Then, while transducer ***A*** is not supplied, 55 kHz, 5.5 tone burst signal is excited with transducer ***B***, and the resulting wave motion is recorded at point ***1***. The recorded signal is time-reversed and re-emitted from transducer ***B***, and the response of the time reversed signal is captured at point ***1***. This procedure is continued for the rest of the points from point ***2*** to point ***6***.

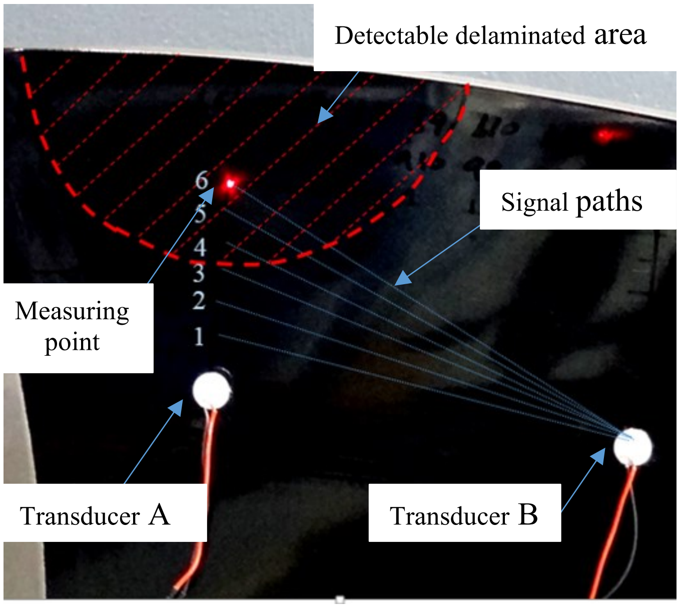

Figure 2.7 Measuring points

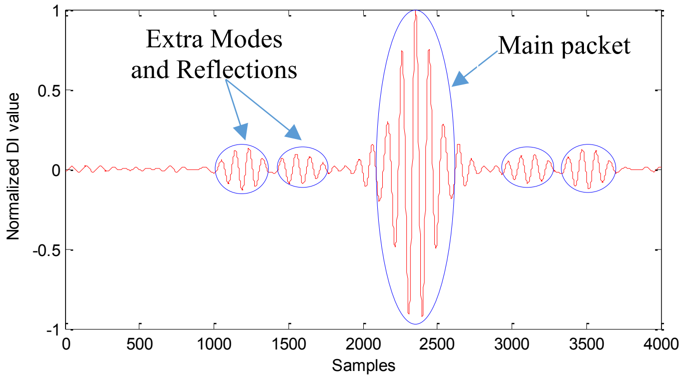

Figure 2.8 Reconstructed signal at point 1 using transducer **A**

The damage levels at the six points are examined along twelve district signal paths. Figure 2.8 shows the reconstructed signal (normalized with respect to the highest amplitude) at point ***1*** using transducer ***A***. The reconstructed signal consists of several wave packets due to the multi-model nature of the lamb wave and the boundary reflections. The main wave packet which represents the A_0 wave mode [3] is compared with the original excitation signal. The results obtained by exciting transducer ***A*** (Figure 2.9) shows relatively high DI values for the points located within the delaminated area as shown in Figure 2.9 (a) (Note that obtained DI values are normalized by the DI values calculated for point 1). It is also observable that the DI values show a slight reduction near the top of the fan blade. Figure 2.10 shows the DI values obtain by exciting transducer ***B*** (Note that obtained DI values were normalized with respect to the DI values calculated at point ***1***). The obtained DIs represent the level of flaws on the signal path and even the DI value measured on a healthy signal path may be nonzero [33]. If a same point is observed by two different transducers, the signal paths employed shall necessarily be distinct and therefore the DI values on a single point measured along two different signal paths can considerably be different depending on the flaws present on each signal path.

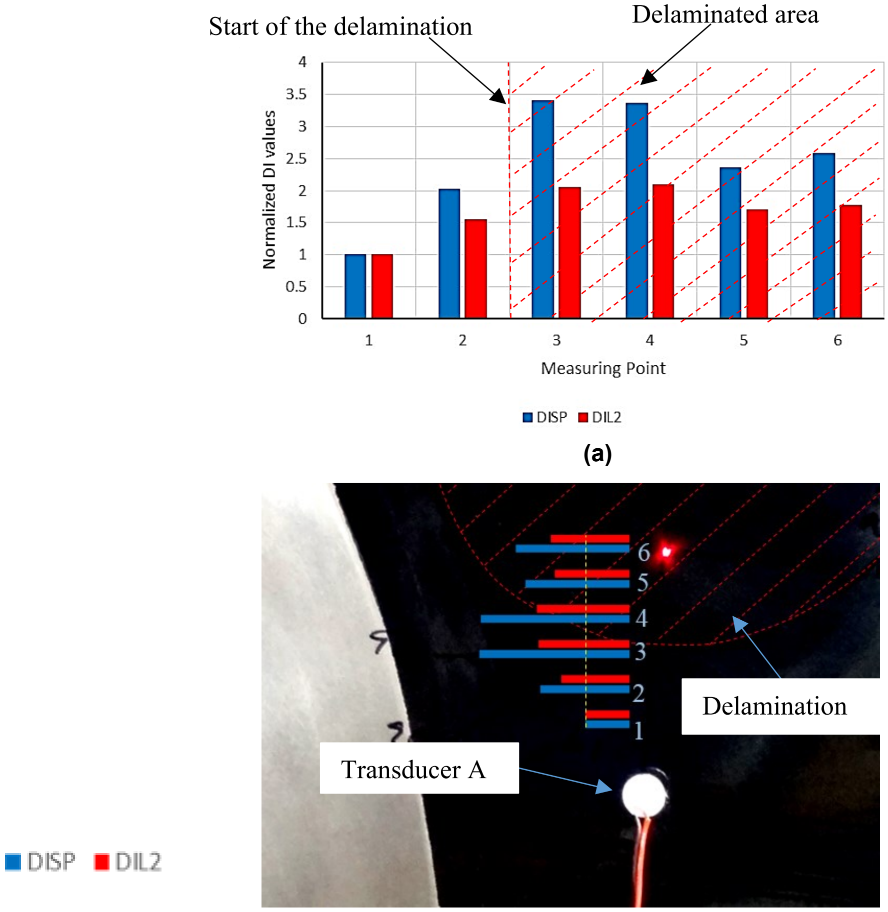

(b)

Figure 2.9 Damage indices obtained for transducer *A*: (a) DI plot, (b) DI value with respect to the measuring location

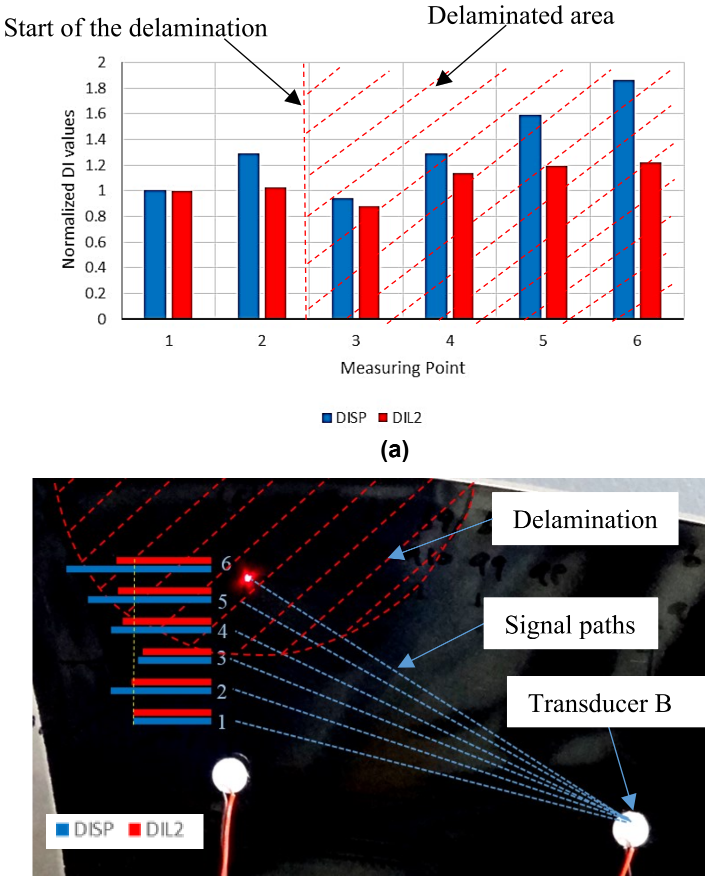

(a)

(b)

Figure 2.10 Damage indices obtained for Transducer ***B***: (a) DI plot, (b) DI value with respect to the measuring location

Above experimental results show the correlation of the DI values with the damage location. However, a strong correlation is not observed, and the DI values fluctuate considerably within the damaged area. This is mainly due to the complexities arising from the multiple wave modes and the boundary reflections. These complexities hinder the effective realization of MTR process and therefore should be treated or/and quantified.

2.5 Complexities in MTR method

2.5.1 Multi-modal effects on MTR method

The influence of the multiple wave modes on the conventional TR method have been investigated in several researches [14] [21] [32]. In this section, we analyze the influence of the multiple wave modes on the MTR method. Let us consider a Lamb wave which contains only the fundamental asymmetric and symmetric modes (A_0 and S_0). If an excitation voltage, $v_A(t)$, is supplied to the piezoelectric actuator A, two wave packets (A_0 and S_0) are created, and the wave packets arrive the sensing point B at different time instances due to differences in their velocities. In the MTR method, the transverse velocity of the wave at point B is recorded by LDV, time-reversed, and supplied to the actuator A as voltage signal. Thus, the excitation voltage has two peaks, one corresponds to A_0 wave packet and the other corresponds to S_0 wave packet. Consequently, the piezoelectric actuator is effectively excited twice creating four wave packets (two wave packets for each voltage peak). Therefore, four wave packets appear in the final (reconstructed) signal.

Park et al. [14] derived an equation for reconstructed waveform of TR process $v_R(t)$, which is given by Eq. (2.19). Here, $v_R^{A_pA_q}$ implies the reconstructed signal of p^{th} antisymmetric (A) wave packet recorded during the second sensing cycle, which is created because of q^{th} A wave packet recorded during the first sensing cycle. Similarly, $v_R^{A_pS_m}$ implies the reconstructed signal of p^{th} A_0 wave packet (recorded during the second sensing cycle) created because of m^th symmetric (S) wave packet recorded during the first sensing cycle. The terms $v_R^{S_pS_q}(t)$ and $v_R^{S_qA_p}(t)$ also follow the same notation. The terms n_A and n_S are the highest order of A and S modes present in the narrow band frequency under consideration.

$$v_R(t) = \sum_{p,q=0}^{n_A} \sum_{n,m=0}^{n_s} \left\{ v_R^{A_p A_q}(t) + v_R^{S_n S_m}(t) + v_R^{A_p S_m}(t) + v_R^{S_n A_p}(t) \right\} \tag{2.19}$$

Following Eq. (2.19), the time reversal operator $\Gamma(\omega)$ for MTR is written as Eq. (2.20). However, unlike ref [14], now for MTR, the structural transfer function for transverse velocity for distinct wave modes are not identical. Here, g_{A_p} represents the structural transfer function for p^{th} A mode and the superscript '*' indicates the complex conjugate. Rest of the terms in Eq. (2.20) follow the same notation.

$$\Gamma(\omega) = G(\omega)G^*(\omega) = \sum_{p=1}^{n_A} \sum_{q=1}^{n_s} \left\{ g_{A_p} g_{A_q}^* + g_{S_p} g_{S_q}^* + g_{A_p} g_{S_q}^* + g_{S_p} g_{A_q}^* \right\} \tag{2.20}$$

Following ref [21], the structural transfer functions can be written as function of frequency dependent amplitude and the natural response of the structure, given by Eq. (2.21). Here, A_p and S_m give the amplitude of p^{th} A wave mode and m^{th} S wave mode, respectively. The term ξ_{AP} indicates the wavenumber of p^{th} A wave mode, and the rest of terms follow the same notation. Finally, the time reversal operator can then be written as Eq. (2.22).

$$g_{A_p} = A_p e^{-i\xi_{AP}x} \quad , \quad g_{S_m} = S_m e^{-i\xi_{Sm}x} \tag{2.21}$$

$$\Gamma(\omega) = \sum_{p,q=0}^{n_A} \sum_{m,n=0}^{n_s} \left\{ A_p A_q e^{-ix(\xi_{Aq}-\xi_{Aq})} + S_m S_n e^{-ix(\xi_{Sm}-\xi_{Sn})} + A_p S_n e^{-ix(\xi_{Sn}-\xi_{Ap})} + S_m A_q e^{-ix(\xi_{Aq}-\xi_{Sm})} \right\} \tag{2.22}$$

The reconstructed waveform is given in Eq. (2.23).

$$v_R(t) = \frac{1}{2\pi} \int_{-\infty}^{\infty} K_{PZT}^2 K_{LDV}^2 \sum_{p,q=0}^{n_A} \sum_{m,n=0}^{n_s} \left\{ \begin{aligned} & A_p A_q e^{-ix(\xi_{Aq}-\xi_{Aq})} + S_m S_n e^{-ix(\xi_{Sm}-\xi_{Sn})} \\ & + A_p S_n e^{-ix(\xi_{Sn}-\xi_{Ap})} + S_m A_q e^{-ix(\xi_{Aq}-\xi_{Sm})} \end{aligned} \right\} V_A(\omega) e^{i\omega t} \, d\omega \tag{2.23}$$

Equation (2.23) produces $\{(n_A + 2)(n_S + 2)\}^2$ number of wave packets. As shown later, all the A_p / A_p and S_m / S_m wave packets have identical time locations on the reconstructed waveform and the rest of the wave packets are located on the sides of the A_p / A_q and S_m / S_n wave packets. Here, A_p / A_q implies the p^{th} A wave packet on the reconstructed signal which is create because of the q^{th} A wave packet recorded during the first sensing cycle. Terms S_m / S_n, A_p / S_n and S_m / A_q follow the same notation. Determination of the time locations of each wave packet on the reconstructed time signal is crucial in order to minimize the multi-modal effects on final DI calculation. For an example, let us consider a Lamb wave that contains only fundamental modes, A_0 and S_0. The distance between the actuator and sensing point is $\boldsymbol{L}$. The time required for A_0 and S_0 modes to reach the sensing point is given in Eq. (2.24);

$$t^0_{A0} = \frac{L}{C_{A0}}, \quad t^0_{S0} = \frac{L}{C_{S0}} \tag{2.24}$$

$\boldsymbol{C_{A0}}$ and $\boldsymbol{C_{S0}}$ are the group velocities of A_0 and S_0 modes, respectively. Suppose the wave is recorded for $\boldsymbol{T_1}$ seconds during the first signal cycle. For a meaningful data acquisition, the captured signal should encompass both wave packets and $\boldsymbol{T_1}$ should be given by;

$$T_1 \geq \max\left[\frac{L}{C_{A0}}, \frac{L}{C_{S0}}\right] \tag{2.25}$$

Once the recorded signal is time-reversed and used for exciting the actuator, the voltage signals corresponding to A_0 and S_0 wave packets are delayed by t^1_{A0} and t^1_{s0}, respectively.

$$t^{1}_{A0} = T_1 - \frac{L}{C_{A0}}, \quad t^{1}_{s0} = T_1 - \frac{L}{C_{S0}} \tag{2.26}$$

Each voltage signal produces two wave packets creating total of four wave packets. The arrival time of A_0 and S_0 wave packets are given by Eq. (2.27) and Eq. (2.28).

$$t_{AA} = t^{1}_{A0} + \frac{L}{C_{A0}} = T_1, \quad t_{AS} = t^{1}_{S0} + \frac{L}{C_{A0}} = T_1 + \left(\frac{L}{C_{A0}} - \frac{L}{C_{S0}}\right) \tag{2.27}$$

$$t_{SS} = t^{1}_{S0} + \frac{L}{C_{S0}} = T_1, \quad t_{SA} = t^{1}_{A0} + \frac{L}{C_{S0}} = T_1 - \left(\frac{L}{C_{A0}} - \frac{L}{C_{S0}}\right) \tag{2.28}$$

In Eq. (2.27) and (2.28), the subscript *AA* indicates the A_0 wave packet recorded during the second sensing cycle which is created because of A_0 wave packet recorded in the first sensing cycle. Other terms follow the same notation. Suppose the wave is recorded for $\boldsymbol{T_2}$ seconds during the second sensing cycle. For a meaningful data acquisition, the captured signal should encompass all the four wave packets. Therefore,

$$\boldsymbol{T_2 \geq max\left[T_1 + \left(\frac{L}{C_{A0}} - \frac{L}{C_{S0}}\right), T_1 - \left(\frac{L}{C_{A0}} - \frac{L}{C_{S0}}\right)\right]} \tag{2.29}$$

Finally, the captured signal is time-reversed, and the time location of each wave packet is given by;

$$\boldsymbol{t^{r}_{AA} = T_2 - T_1}, \quad \boldsymbol{t^{r}_{AS} = T_2 - T_1 - \left(\frac{L}{C_{A0}} - \frac{L}{C_{S0}}\right)} \tag{2.30}$$

$$\boldsymbol{t^{r}_{SS} = T_2 - T_1}, \quad \boldsymbol{t^{r}_{SA} = T_2 - T_1 + \left(\frac{L}{C_{A0}} - \frac{L}{C_{S0}}\right)} \tag{2.31}$$

According to Eq. (2.30) and (2.31), A_0/A_0 wave packet and S_0/S_0 wave packets overlap with each other, and they are located at $\boldsymbol{T_2 - T_1}$ seconds in the reconstructed signal. This combined wave packet is called the "main wave packet," and shown to be equal to the excitation signal, after the amplitudes are normalized [14] [23]. Additionally, the time location of A_0/S_0 and S_0/A_0 wave packets are symmetric around the main wave packet, and their amplitude are not necessarily identical. In the low frequency range, $\left(\frac{L}{C_{A0}} - \frac{L}{C_{S0}}\right) > 0$. Therefore, S_0/A_0 wave packet is located to the right of the main wave packet and A_0/S_0 wave packet is located to the left of the main wave packet. The relative time locations of the four wave packets are illustrated in Figure 2.11.

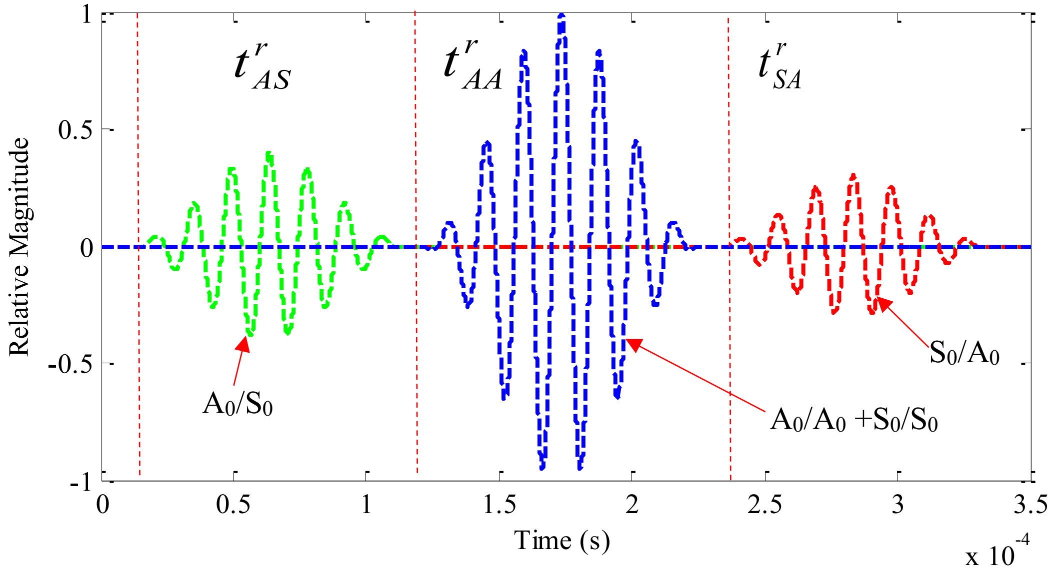

Figure 2.11 Time location of wave packets on the reconstructed signal

According to Eq. (2.30) and Eq. (2.31), time location of the main wave packet does not rely upon the group velocities. This implies that, the time-length of the excitation signal is preserved, regardless of the actuator sensor distance and the group velocities. However, the time length is not preserved in A_0/S_0 and S_0/A_0 wave packets. Existence of the side wave packets may cause inaccurate DI calculations. As depicted in Figure 2.12 (a), when the side wave packets do not interfere with the main wave packet, the time domain comparison is accurate. However, if the side wave packets interfere with the main wave packet, as shown in Figure 2.12 (b), the time domain comparison produces inaccurate DIs because in this scenario, side wave packets are also accounted for DI calculation. (In Figure 2.12 (a) and (b), Z vel and Exct indicate transverse velocity and excitation signal, respectively)

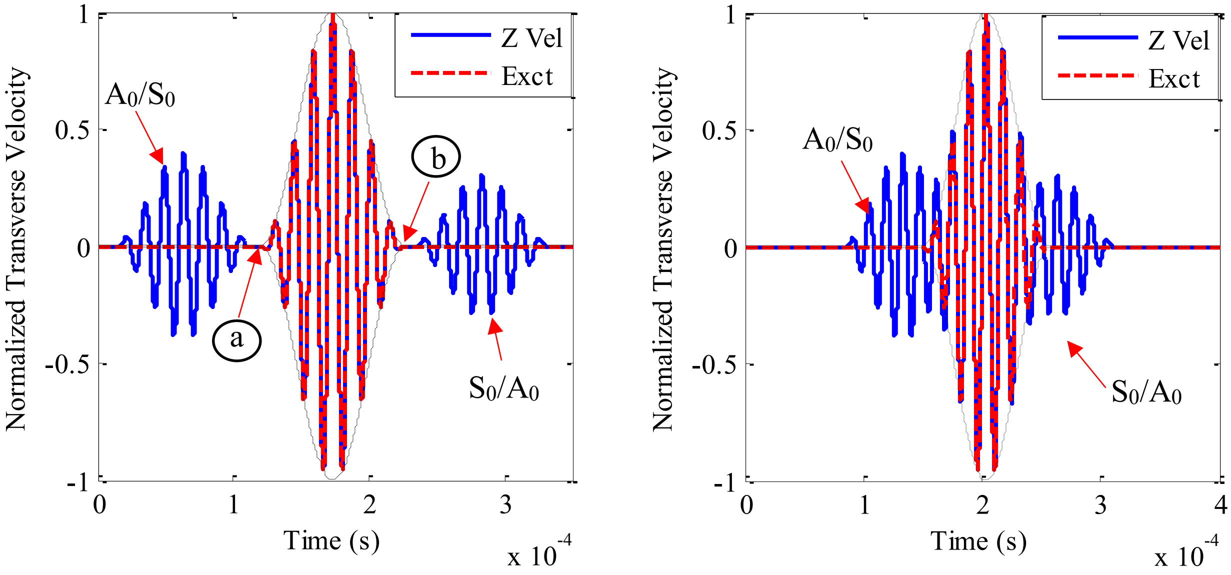

Figure 2.12 Reconstructed sigal (a) side wave packets separated from main wave packet (b) side wave packets overlap with main wave packet

From Eq. (2.30) and Eq. (2.31), in order to avoid wave packet overlapping, the minimum distance between the actuator and sensor is calculated as Eq. (2.32). Here, t_0 is the time-length of the excitation signal.

$$L \geq \frac{t_0}{\left(\frac{1}{C_{A0}} - \frac{1}{C_{S0}}\right)} \tag{2.32}$$

Note that Eq. (2.32) is valid not only for MTR, but equally applicable for conventional TR regardless of the choice of the measured quantity (strain or velocity). In order to demonstrate the validity of Eq. (2.32), a FE simulation is conducted. The FE model consists of a 1.2mm thick aluminum plate and two piezoelectric transducers. The material properties are given in Table 2.1. A 3.5cyle, 70 kHz voltage signal is given to actuator ***A*** and the signal (voltage output) is measured by at sensor location ***B***. The transverse velocity at t = 9×10^{-5} seconds is shown in Figure 2.13.

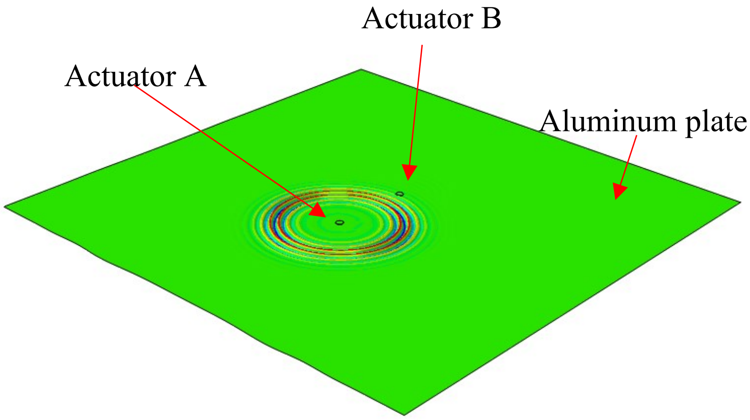

Figure 2.13 Transverse velocity from FE simulation (t = 9×10^{-5}s)

Table 2.1 Material Properties

Piezoelectric (S410) [34]			Aluminum	
Density (ρ)		7800 kg/m^3	Density (ρ)	2700 kg/m^3
Elastic modulus (E)		76Gpa	Elastic modulus (E)	68.9 Gpa
Poisson's ratio (υ)		0.2	Poisson's ratio (υ)	0.33
Piezoelectric constant	d_{31},d_{32}	-1.9×10^{-10} m/v		
	d_{33}	4.5×10^{-10} m/v		

For 70 kHz excitation frequency, wave speeds for the two modes are C_{A0}=1672 ms^{-1}, C_{S0}=5436ms^{-1}, and t_0=5×10^{-5}s. The minimum value of ***L*** is calculated as 0.1207 m in order to avoid wave packet overlapping. The simulation is conducted for two configurations, ***L*** = 0.05m and *L*=0.15m. The reconstructed waveforms for each configuration are shown in Figure 2.14 (a) and (b), which clearly shows that for ***L***=0.05m the side wave packets interfere with the main wave packet (Figure 2.14 (a)) whereas for ***L***=1.5m there is no overlap of wave packets (Figure 2.14 (b)).

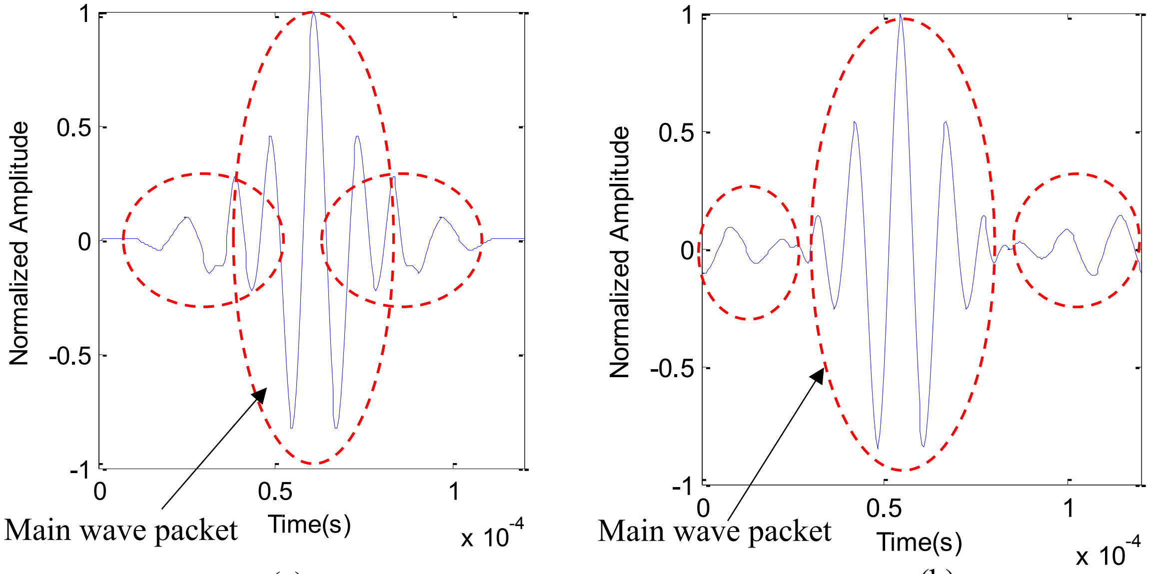

(a) (b)

Figure 2.14 Reconstructed waveform (a) ***L*** = 0.05m (b) ***L***=0.15m

2.5.2 Dispersion and multi-modal effects

Eq. (2.21) is valid only if the frequency range of the excitation signal is narrow so that dispersion effects are minimum. Suppose ω_L and ω_H are the lower and upper frequency bounds of the excitation signal and $C_{\omega_L A0}$, $C_{\omega_H A0}$, $C_{\omega_L S0}$ and $C_{\omega_H S0}$ are the corresponding group velocities of A_0 and S_0 modes. Within the MTR process, the fast-moving wave packets arrive at the sensing points earlier, followed by the slow-moving wave packets. However, after time-reversal (following the first sensing cycle), the later- arriving wave packets are emitted by the actuator earlier than the early-arriving wave packets. Thus, both fast- and slow-moving wave packets arrive at the sensing point at the same time during the second sensing cycle. Nevertheless, this is not applicable for A_0/S_0 and S_0/A_0 packets because they travel at different velocities during first and second sensing cycles. The time locations of A_0/S_0 and S_0/A_0 wave packets are given by Eq. (2.33) and Eq. (2.34).

$$t_a^r = max\left[T_2 - T_1 - \left(\frac{L}{C_{\omega_L A0}} - \frac{L}{C_{\omega_L S0}}\right), T_2 - T_1 - \left(\frac{L}{C_{\omega_H A0}} - \frac{L}{C_{\omega_H S0}}\right)\right] \tag{2.33}$$

$$t_b^r = min\left[T_2 - T_1 + \left(\frac{L}{C_{\omega_L A0}} - \frac{L}{C_{\omega_L S0}}\right), T_2 - T_1 + \left(\frac{L}{C_{\omega_H A0}} - \frac{L}{C_{\omega_H S0}}\right)\right] - t_0 \tag{2.34}$$

In order to prevent the side wave packets from overlapping with the main wave packet, the distance between the actuator and sensor must be selected according to Eq. (2.35).

$$L \geq \frac{t_0}{max\left[\left(\frac{1}{C_{A\omega_L 0}} - \frac{1}{C_{S\omega_L 0}}\right), \left(\frac{1}{C_{A\omega_H 0}} - \frac{1}{C_{S\omega_H 0}}\right)\right]} \tag{2.35}$$

In general, for a wave with $\boldsymbol{n_A}$ number of A modes and $\boldsymbol{n_S}$ number of S modes, distance $\boldsymbol{L}$ can be calculated using Eq. (2.34).

$$L \geq \frac{t_0}{min\left[\left(\frac{1}{C_{Ap}^H} - \frac{1}{C_{Sm}^L}\right), \left(\frac{1}{C_{Ap}^L} - \frac{1}{C_{Sm}^H}\right), \left(\frac{1}{C_{Ap}^H} - \frac{1}{C_{Aq}^L}\right), \left(\frac{1}{C_{Sm}^H} - \frac{1}{C_{Sn}^L}\right)\right]} \tag{2.36}$$

$$[p,q] \in [0,\dots,n_A],\ [m,n] \in [0,\dots,n_S] \text{ for } [C_{Ap}^H, C_{Ap}^L] \leq [C_{Sm}^H, C_{Sm}^L]$$

2.5.3 Boundary condition effects

Structural boundaries produce side wave packets in the reconstructed signal (similar to multi-modal excitation) leading to inaccurate DIs. Let us consider a wave with a single mode (A_0) propagating in a plate with a single structural boundary and suppose that the actuator produces only the A_0 mode once the excitation voltage is supplied. During the first sensing cycle, the LDV records the direct A_0 wave packet, the reflected A_0 wave packet and the mode converted

S_0 wave packet wherein the latter two wave packets are caused by the boundary. All the wave packets are recorded and time-reversed, and the time-revered signal is given to the actuator in the form of an excitation voltage. Such excitation produces corresponding A_0 and S_0 modes at the actuator giving six wave packets, and each of these six wave packets results in three wave packets (direct, reflection and mode-conversion) at the sensing point. Consequently, a total of 18 (9-A_0, 9-S_0) wave packets appear in the reconstructed waveform. However, at least two Lamb wave modes exist at any given frequency. Therefore, for the simplest Lamb wave, 36 wave packets constitute the reconstructed waveform. Many of the wave packets interfere with each other and they are not clearly distinguishable. The time-location of each wave packet for a general Lamb wave can be formulated as follows.

For Eq. (2.37), Eq. (2.38), and Eq. (2.39), following notation is used. The superscripts ***D***, ***R***, and ***C*** indicate direct wave packet, reflected wave packet, and the mode converted wave packet. The subscripts A_P, and S_m represent the p^{th} A mode, and the m^{th} S mode, respectively. The subscript ApAq indicates the A_p wave packet of the reflected/ mode converted $\boldsymbol{A_q}$ wave packet, and similarly SmAp indicates the $\mathrm{S_m}$ wave packet after the mode conversion of the $\boldsymbol{A_p}$ wave packet. $\boldsymbol{L}$, $\boldsymbol{L_1}$ and $\boldsymbol{L_2}$ are the distance between actuator and sensor, the distance between the actuator and the boundary is $\boldsymbol{L_1}$, and the distance between boundary and the sensor, respectively. The time-location of A and S wave packets in the first sensed signal are given by Eq. (2.37) and Eq. (2.38), respectively.

$$t^{D}_{A_pA_p} = \frac{L}{C_{Ap}},\quad t^{R}_{A_pA_q} = \frac{L_1}{C_{Aq}} + \frac{L_2}{C_{Ap}},\quad t^{C}_{A_pS_m} = \frac{L_2}{C_{Ap}} + \frac{L_1}{C_{Sm}} \tag{2.37}$$

$$t^{D}_{S_mS_m} = \frac{L}{C_{Sm}},\quad t^{R}_{S_mS_n} = \frac{L_1}{C_{Sn}} + \frac{L_2}{C_{Sm}},\quad t^{C}_{S_mA_p} = \frac{L_2}{C_{Sm}} + \frac{L_1}{C_{Ap}} \tag{2.38}$$

If the wave is recorded for T_1 seconds during the first sensing cycle and T_2 seconds during the second sensing cycle, the time locations of various wave packets in the reconstructed waveform are given by Eq. (2.39).

$$t = T_2 - T_1 + (t^{i}_{x_j y_k} - t^{u}_{x_v y_u}) \tag{2.39}$$

$x, y \in [A, S], j, u \in [D, R, C]$, $j, k, u, v \in [0, \ldots\ldots, n_S]$ for S modes, $j, k, u, v \in [0, \ldots\ldots, n_A]$ for A modes.

Note that the reconstructed signals in the directly sensed wave packets converge at $T_2 - T_1$ resulting in the main wave packet. The time-location of the main wave packet is independent of the group velocities and the distances (***L***, ***L₁*** and ***L₂***). The reflected and mode-converted wave packets produce side wave packets, depending on the group velocities and the distances. However, some of the reflected and mode-converted wave packets which satisfy, $t^{i}_{x_j y_k} = t^{u}_{x_v y_u}$ relationship also converge at $T_2 - T_1$. Therefore, the main wave packet of the reconstructed waveform is composed of waves which satisfy $t^{i}_{x_j y_k} = t^{u}_{x_v y_w}$ relationship, including some of the reflected and mode converted wave packets. As result, the boundary effects are included within the main wave packet (and affects DI calculation), regardless of the location of the boundaries. Additionally, the interference between the side wave packets and the main wave packet may result in inaccurate DIs. In order to prevent such interference, the actuator – sensor distances should be selected to satisfy the relationship given in Eq. (2.40).

$$(t^{i}_{x_j y_k} - t^{u}_{x_v y_w}) \geq t_0 \tag{2.40}$$

Numerically generated structural boundary locations which satisfy Eq. (2.40) is shown in Figure 2.15 (a). For this particular example, the coordinate system is defined with respect to the actuator location (*0, 0*), and the distance between the actuator and the sensing point (*0.2m,0m*) is preselected. According to Eq. (2.37), (2.38) and (2.39), the numerical difference between L_1 and L_2 should be sufficiently large in order to satisfy Eq (2. 40). For 70 kHz wave, the difference between L_2 and L_1 should satisfy $\left|L_2 - L_1\right| \geq t_0 / \left(1/C_{A0} - 1/C_{S0}\right)$ relationship. However, in region ***A*** and ***B*** this relationship is not satisfied at all. At low frequencies, Lamb wave mode S_0 resemble axial wave [32], and if LDV is employed, only the transverse velocities are measured. Therefore, for low frequency velocity measurements, the presence of the S_0 wave mode can be neglected. The boundaries that satisfy Eq. (2.40) is now given in Figure 2.15 (b).

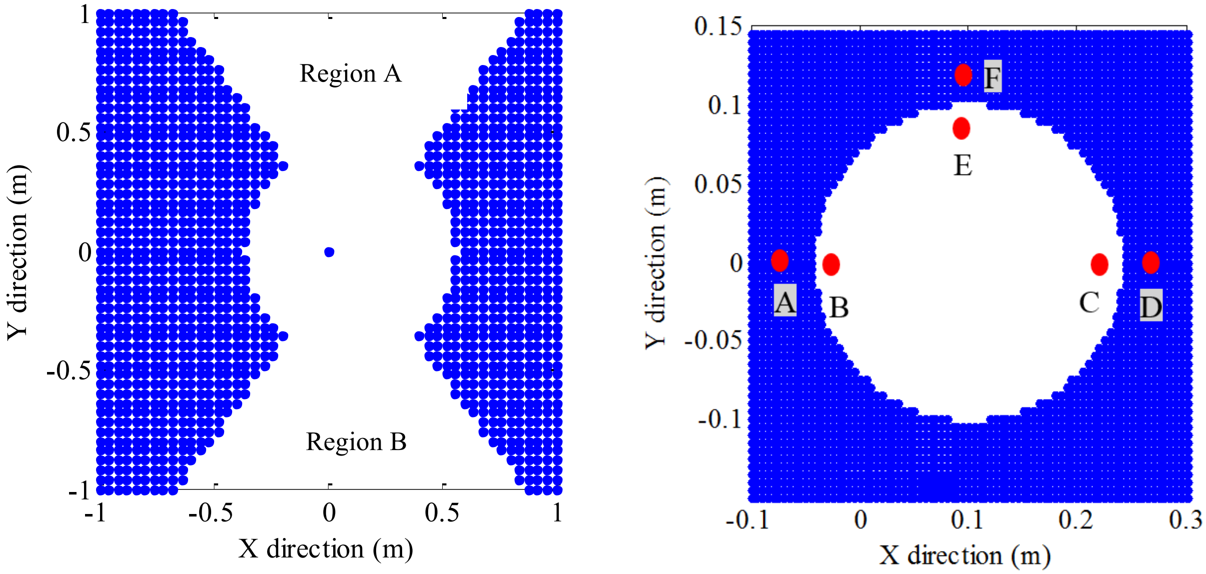

(a) (b)

Figure 2.15 Numerically generated (a) boundary when both A_0 and S_0 are dominant (70 kHz, 5.5 cycle) (b) boundary when A_0 is dominant (70 kHz, 5.5 cycle) or LDV is used for transverse velocity measurements

2.5.4 Experimental quantification of boundary effects

The experimental setup (shown in Figure 2.16) comprises of a 1.2mm thick, rolled formed, 6000 series aluminum plate and a disc type piezoelectric transducer (material: SM412) permanently bonded to the plate. The actuator has dimensions of 12mm diameter and 0.5mm thickness. The excitation voltage is generated by Agilent 33220A function/arbitrary waveform generator (5Vpp) and amplified by A.A Lab Systems' A303 high voltage amplifier and modulator (up to 100Vpp). An LDV (Polytec OFV-5000 with OFV-500 laser head) is used to record the transverse velocity at the sensing points. The sampling frequency is 2560 kHz and a low-pass frequency filter (200 kHz) is employed in order to reduce the noise level. For each measurement, the signals are recorded twenty times and then averaged in order to minimize the effects of random noise.

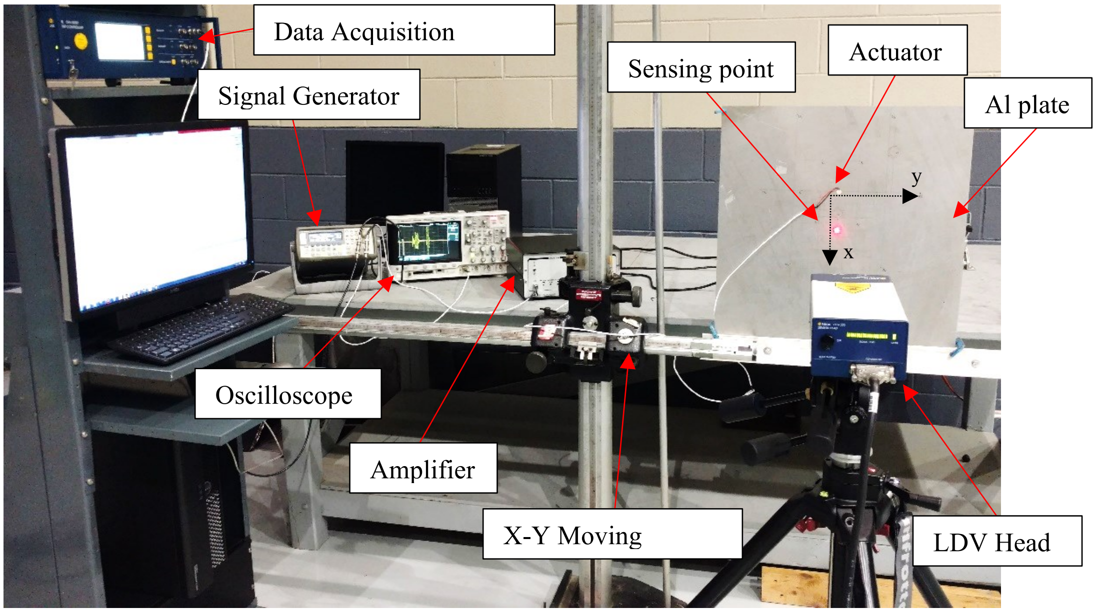

Figure 2.16 Experimental set up

A 70 kHz, 5.5 tone burst signal is used for excitation. At 70 kHz, only the fundamental wave modes exist and wave speeds are C_{A0}=1672 ms-1, C_{S0}=5436ms-1. An attachable metal piece is used to simulate a non-symmetric structural boundary. The location of the metal piece is varied in order to simulate the structural boundaries at different locations as shown in Figure 2.15 (b). The sensing point is kept fixed at (0.2 m, 0) location. Six locations are selected in order to validate Eq. 2.40, and excitation signal is reconstructed at each location. Three points (A, D, and F) are located on shaded area and three points (B, E, and C) are located inside white (unshaded) area. The experimentally reconstructed signals at each boundary location are shown in Figure 2.17 (a)-(d) and Figure 2.18 (a)-(b). It is observed that the side wave packets do not interfere with the main wave packet if the structural boundary is in the shaded (blue) area, as given by Eq. (2.40). However, if the boundaries are located inside the unshaded (white) area, the main wave packet experiences interference by the side wave packets resulting in inaccurate DI values.

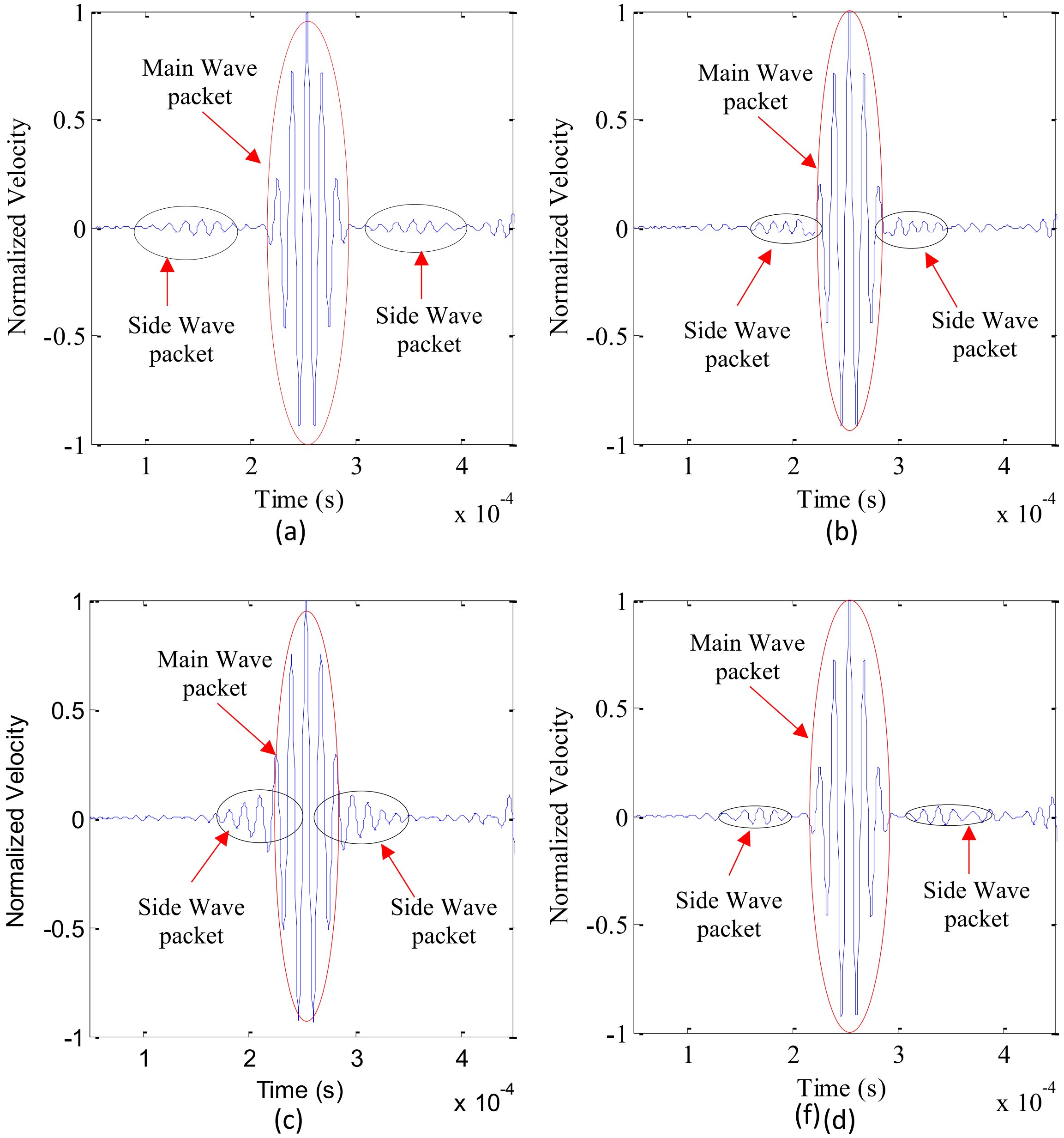

Figure 2.17 Reconstructed waveforms at location (a) A (b) B (c) C (d) and D (e)

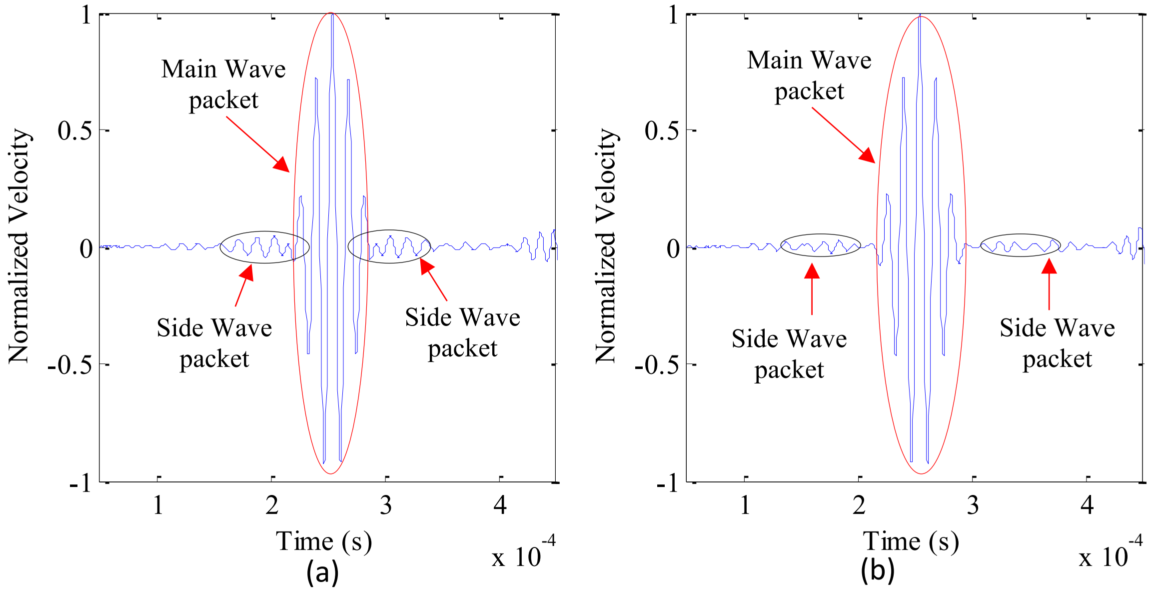

Figure 2.18 Reconstructed waveforms at location (a) E, and (b) F

It is worthwhile to mention that, in complex structures, wave packet overlapping due to the structural boundaries cannot be avoided. In such cases, Eq. 2.39 can be used to identify the side wave packets created by each boundary. The most straight forward approach to avoid the complexities arising from structural boundaries, is to capture only the first wave packet during the first sensing cycle. In this way, the reflections and mode conversions are not captured during first sensing cycle. Additionally, the structural damages located outside of the signal path are analogous to the structural boundaries. Therefore, it can be stated that if a damage is located inside the unshaded (white) area, that particular structural damage changes the DI value (by side wave packet overlapping) even though it is not located on the signal path. We use this characteristic to detect damages in a following section.

2.5.5 Repeatability of MTR method

Repeatability indicates the ability of a technique to consistently produce the same results under the same measurement conditions. The repeatability of MTR method is evaluated using the experimental set up shown in Figure 2.16. A metal disc is attached to the plate to simulate a damage and the MTR process is repeated 25 times. The DIs are calculated each time and normalized with maximum DI value. The standard deviation (σ) of normalized DISP is 0.03 and normalized DIL2 is 0.015. The calculated distributions (Figure 2.19 (a), (b)) reveal that the MTR method produces very consistent DIs under laboratory conditions.

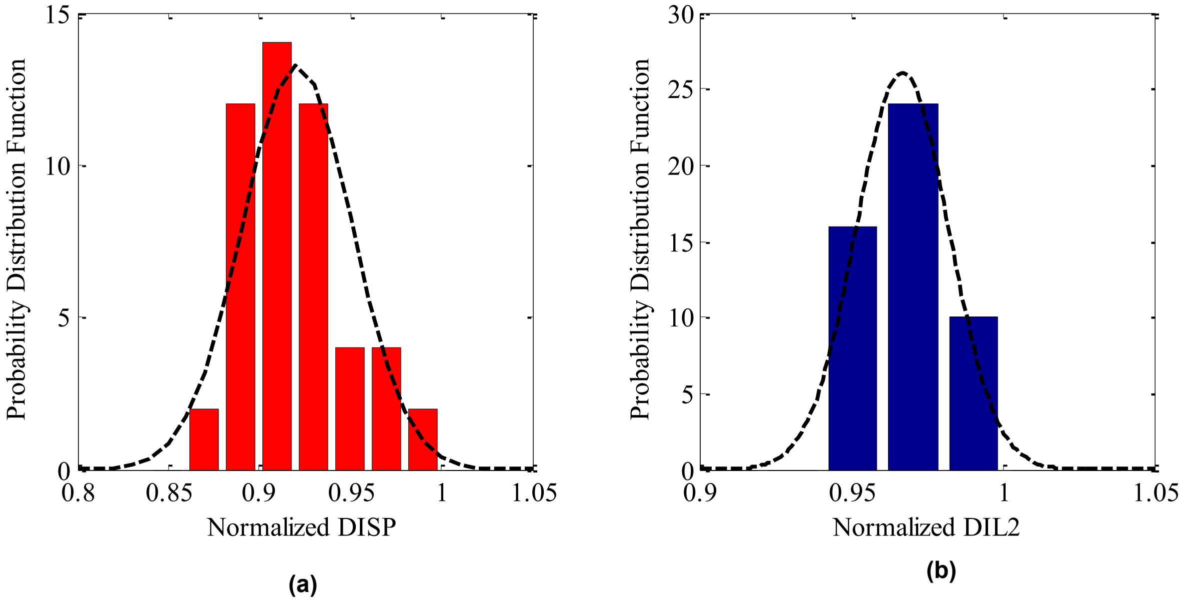

(a)

(b)

Figure 2.19 Probability distribution of (a) DISP, and (b) DIL2

Therefore, it is clear that MTR method along with non-contact sensing is capable of generating significantly repeatable damage information.

2.5.6 Similarity and number of cycles

The similarity between the excitation signal and the reconstructed signal is investigated experimentally. Considering similarity between excitation and reconstructed signal for undamaged structures is important to determine how the parameters of excitation signal (i.e. number of cycles, frequency) affect the MTR process. Once these effects are determined, an optimum excitation signal can be used to for high resolution damage detection. The experimental set up given in Figure 2.16 is employed and the pristine structure (no damage) is considered. Eq. (2.41) is used to calculate the similarity and the results are given in Figure 2.20. The similarity between excitation (voltage) signal and reconstructed signal is observed to increase as the number of cycles of the tone burst signal increases, similar to the results for conventional TR method [16]. In Eq. 2.41, A_i and A_j are the signals to be compared for similarity.

$$\mathbf{Similarity(i,j) = 1 - \sqrt{\sum_N (A_i - A_j)^2 \Big/ \sum_N A_j^2}} \tag{2.41}$$

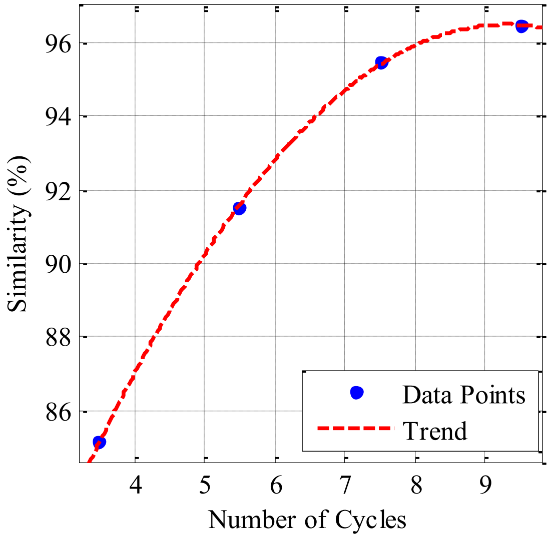

Figure 2.20 Similarity between the excitation voltage and the reconstructed signal

2.5.7 Damage index variation with number of cycles

The relationship between number of cycles (***N***) and sensitivity of MTR method is investigated experimentally (Figure 2.21). MTR is performed with 70 kHz tone burst signals with the number of cycles ranging from 3.5 to 9.5. As shown previously, the similarity between excitation voltage and reconstructed waveform increases as the number of cycles increase, and therefore DI values decrease. This is clearly demonstrated in Figure 2.21 (a) and (b). The DI values follow power law (that is, $y = ax^{-b}$) relationship with ***N*** (number of cycles). The increase of DIL2 values due to the damage is nearly constant for ***N*** = 3.5 to 9.5. However, DISP shows much larger increase due to damage for low cycle tone burst excitation. It is noted that the frequency bandwidth of the excitation increases as the number of cycles decreases which reduces the ability to reconstruct the original signal. The wider bandwidth waves show higher sensitivity to damages compared to that of narrow band excitations.

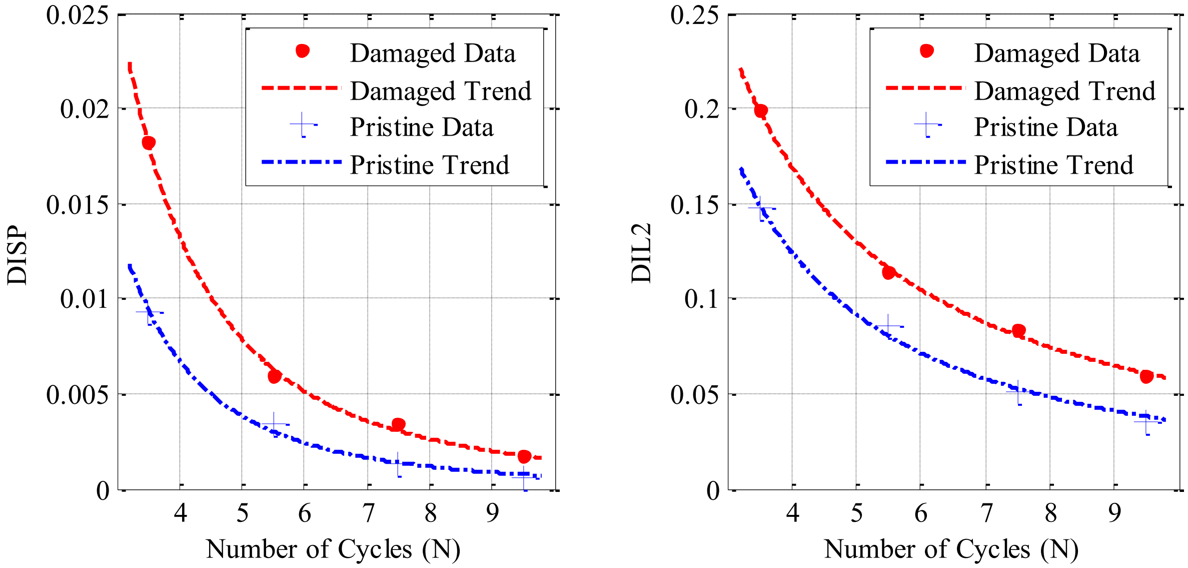

Figure 2.21 Damage sensitivity variation with number of cycles (a) DISP (b) DIL2

2.5.8 DI sensitivity to damages on the signal path

The experimental setup (Figure 2.21) is employed to investigate the sensitivity of DI for damage (represented by an attachable disc) location along actuator-sensor path. With fixed actuation and sensing points, the attachable disc is placed at six locations along the signal path (shortest path). The DI values calculated for each damage location are given in Figure 2.22 (a) and (b) where the distance (x-value) is measured from the outer edge of the actuator. The DIs have their minima close to the mid-point between actuator and sensing point and show higher values close actuator or sensing point. For each damage location, the MTR method is repeated three times by attaching and detaching the disc. The difference between the DIs calculated for a particular location is due to damage reproducibility errors of the attachable disc. On the other hand, if MTR process is repeated without detaching and re-attaching the disc, nearly identical DI values should have been obtained. As mentioned earlier in this paper, DI calculations are formulated to capture phase and shift of frequencies. Since the sensing point is fixed, slight phase and frequency shifts may have constructive or destructive effects on each other, depending on the damage location. Therefore, resulting location dependent DI values. As a summary of the section, depending on the location of the damage, the calculated DIs should be adjusted depending on the location of the damage in order to obtain accurate damage severities. In Figure 2.22, the trend lines are generated using second order least squares fit.

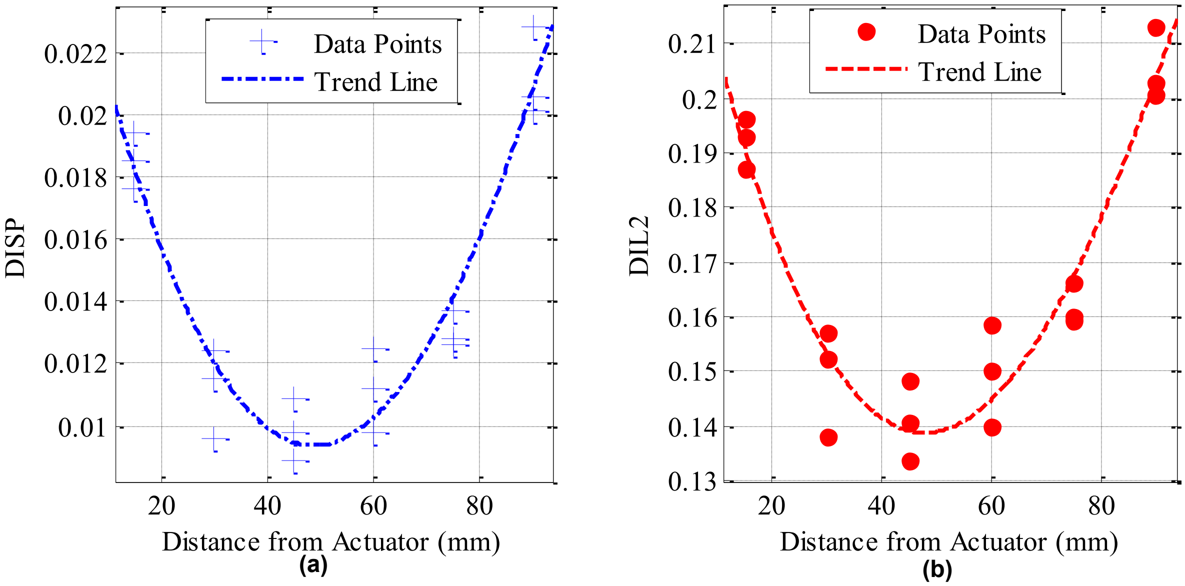

Figure 2.22 Damage index sensitivity with damage location along signal path (a) DISP (b) DIL2

2.6 Improve MTR process

2.6.1 Damage index tuning

We introduce a novel technique, “Damage Index Tuning” to minimize the multi-modal and boundary effects. This technique is very similar to, but much practicable and simpler than the mode tuning process. Damage index tuning is conducted on the pristine structure in order to determine the optimum excitation frequency that produces least distorted time–reconstructed signal (for pristine structure). The time reversal process is conducted within a prescribed frequency range on selected frequency intervals (generally, the selection of this frequency range is governed by the bandwidth of actuators, signal generators, amplifiers and LDV). DI values are calculated for each frequency and plotted against the excitation frequency. The optimum excitation frequency produces the least distorted time-reversed signal and therefore results the lowest DI. In contrast to the mode tuning process, several wave modes that have non-zero amplitude may co-exist on the optimum excitation frequency, and the boundary effects may be considerable. Damage Index Tuning focuses to minimize the combined effects of side wave packets within the given excitation frequency bandwidth. Therefore, at the optimum frequency, the combined effect is minimum. Additionally, this procedure can be conducted within the original MTR structure-actuator configuration, without addition of any special type transduces and/or measuring technique.

The values of DISP and DIL2 are calculated for eight excitation frequencies between 40 kHz and 110 kHz for the cases of $\mathbf{N} = 5.5$ and $\boldsymbol{N} = 7.5$ using the pristine structure. The DIs decrease as the excitation frequency increases reaching a certain minimum and increase with the excitation frequency. Further, the bonding conditions between actuator and host structure and the initial structural imperfections (possibly damages) are accounted for during the DI tuning process. Thus, the DI tuning process produces the optimum excitation frequency minimizing the multi-modal effects and attenuating the initial structural defects to allow better damage resolution.

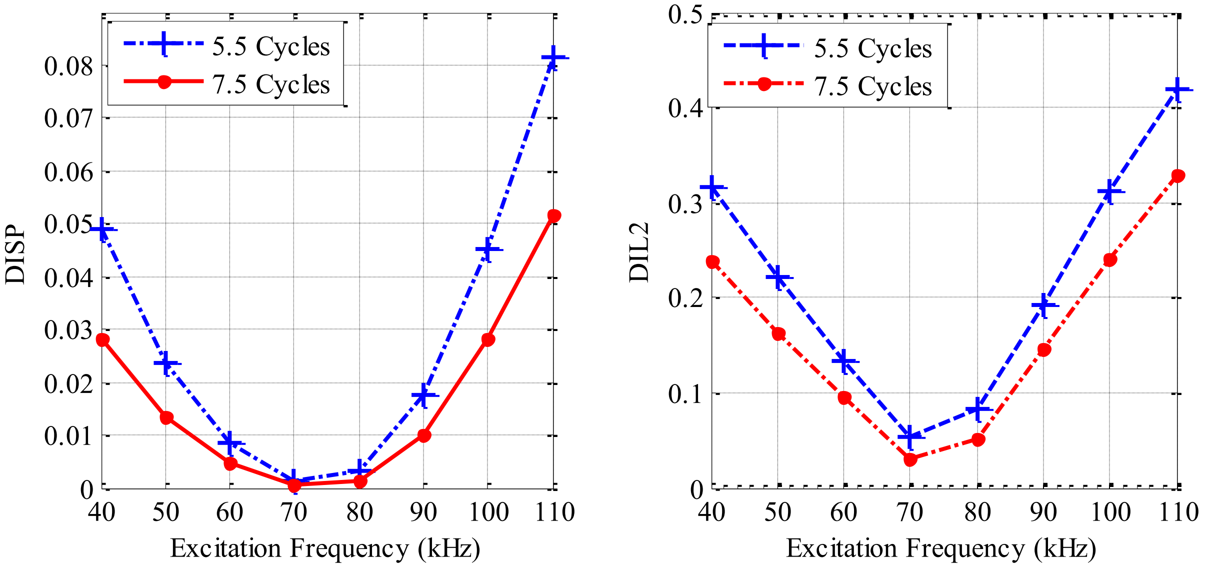

Figure 2.23 Variation of DI values (pristine structure) with excitation frequency (a) DISP (b) DIL2

2.7 MTR method for generic damage detection

The main limitation of the conventional TR method (along with related DI formulations) is that it is capable of detecting damages only if they lead to signal nonlinearity. Gangadharan et al. [14] showed experimentally that a notch type damage in a metallic structure does not break the time reversibility of Lamb waves, hence it is not detectable by conventional TR method. Additionally, the reconstructed signals obtained failed to exhibit notable changes as the size of the damage varied. This hinders the applicability of TR method for generic damage detection, especially for the damages in homogenous isotropic materials resemble structural features (for example, hole in a thin aluminum plate). First, we show that similar to the conventional TR method, MTR method along with the conventional DI calculation is not capable of detecting linear damages. Then we developed a time-frequency domain-based technique for the detection of linear damages.

The experimental setup described in Figure 2.24 is used, with a coin simulating a superficial non-symmetric damage. The location of the damage is treated as an unknown. The coin is attached to the structure using a soft adhesive film, as shown in Figure 2.24. Thirteen (13) sensing points are used, and the distance between each consecutive sensing point is set to 20mm. Since this experiment evaluates the MTR method for detecting generic damages, the other variables including multimodal effects and boundary effects are minimized by selecting low excitation frequency and capturing the first wave packet during the first-sensing cycle (as described in the preceding sections). The actuator is excited with a 5.5 cycle tone-burst 70 kHz signal. The MTR method is thirteen times for each sensing path, and average DI values are calculated.

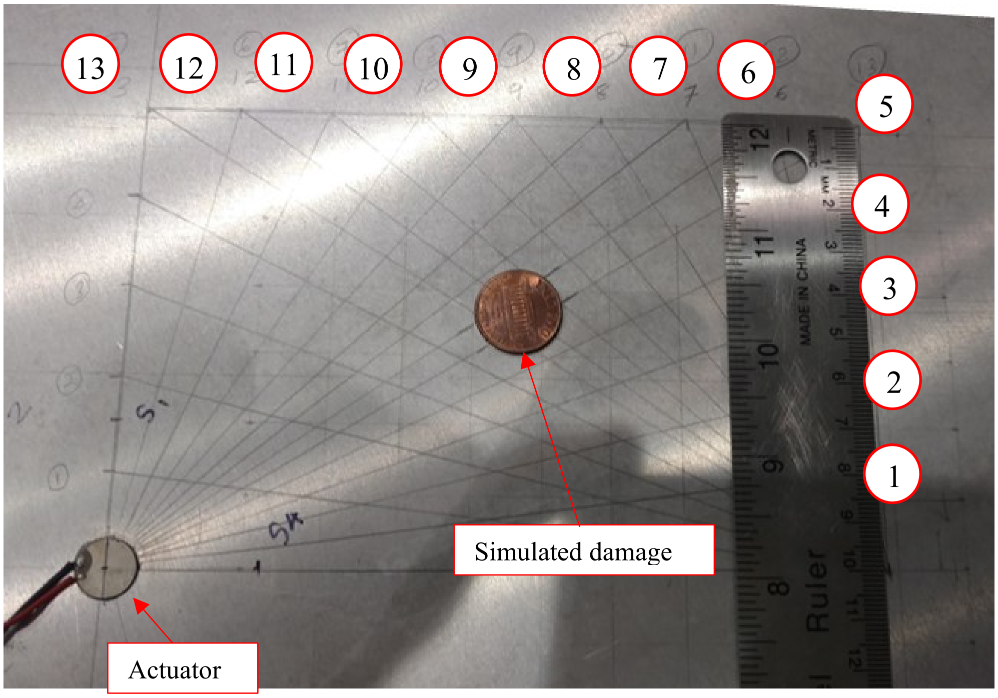

Figure 2.24 Damage and sensing locations (points 1-13) with respect to the actuator

Figure 2.25 shows the DI values calculated for each sensing path using Eq. (2.18). The results suggest that the signal path #11 contains a damage, since it has the highest DI value, but that is erroneous. In fact, the signal paths #5 and #6 pass through the damage. Therefore, the reconstructed signals for signal path *#5* and *#6* should have the highest distortion (highest DI values) compared to that of the other signal paths. However as shown in the figure, most of the DI values are higher than that of the signal paths #5 and #6. This inconsistency is caused by two factors:

1. Side wave packets created by the reflections at the damage overlap with the main wave packets and distort the overall signal.
2. The distortion created by the damage (signal non-linearity) is much smaller compared to the distortion created by overlapping.

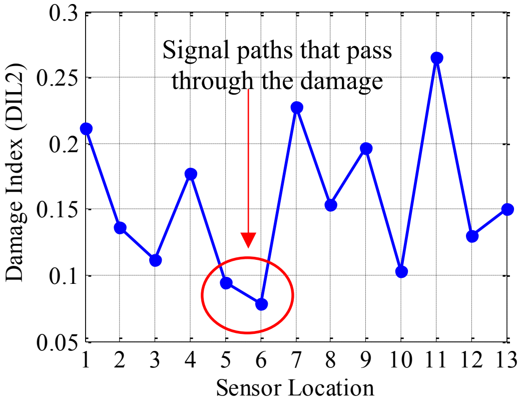

Figure 2.25 Damage index values

2.7.2 Detection of generic damages through frequency time analysis of reconstructed signal

As mentioned earlier, the reconstruction process compensates for the delays/advances of the arrival of the wave packets. For example, all the delayed wave packets (during the first sensing cycle) are excited in advance during the second sensing cycle. Subsequently, delays are compensated, and the time length of the main wave packet is preserved. Similarly, if the signal path consists of a damage, the overall time length of the main wave packet does not change while the shape (in time domain) and spectral energy distribution (in frequency domain) are affected by the damage. On the other hand, if a damage site is away from a signal path, the side wave packets created due to the reflections by the damage appear in the reconstructed signal. Overlapping of side wave packets change the time length of the main wave packet. In this analysis, we attempt to segregate the reconstructed signals which have preserved time lengths (main wave packet) from those which have distorted time lengths (main wave packet overlaps with side wave packets). Figure 2.26 shows two arbitrarily selected reconstructed signals (paths #4 and #8). As shown in the figure, given their relatively low magnitude, the presence of side wave packets is not clearly visible. Therefore, it is very difficult to make an accurate evaluation by considering the time-domain signal. For further analysis, the reconstructed signals are transformed into time-frequency domain using Short-Time Fourier (STF) transformation.

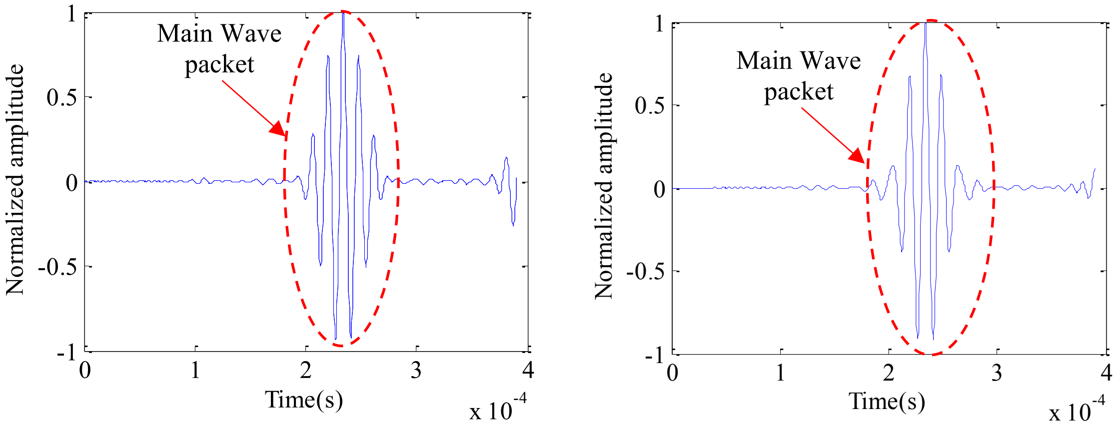

(a) (b)

Figure 2.26 Time reversed - normalized signal (a) signal path #4 (b) signal path #8

First, the excitation signal is transformed into time-frequency domain. Since the time length of the excitation signal is known, the parameters of STF transformation are adjusted so that the spectral energy at 70 kHz passes through -40dB levels at the limits of the time signal. Figure 2.27 (a), (b) and (c) show the time domain signal, spectral energy distribution and spectral energy distribution of the excitation signal, respectively.

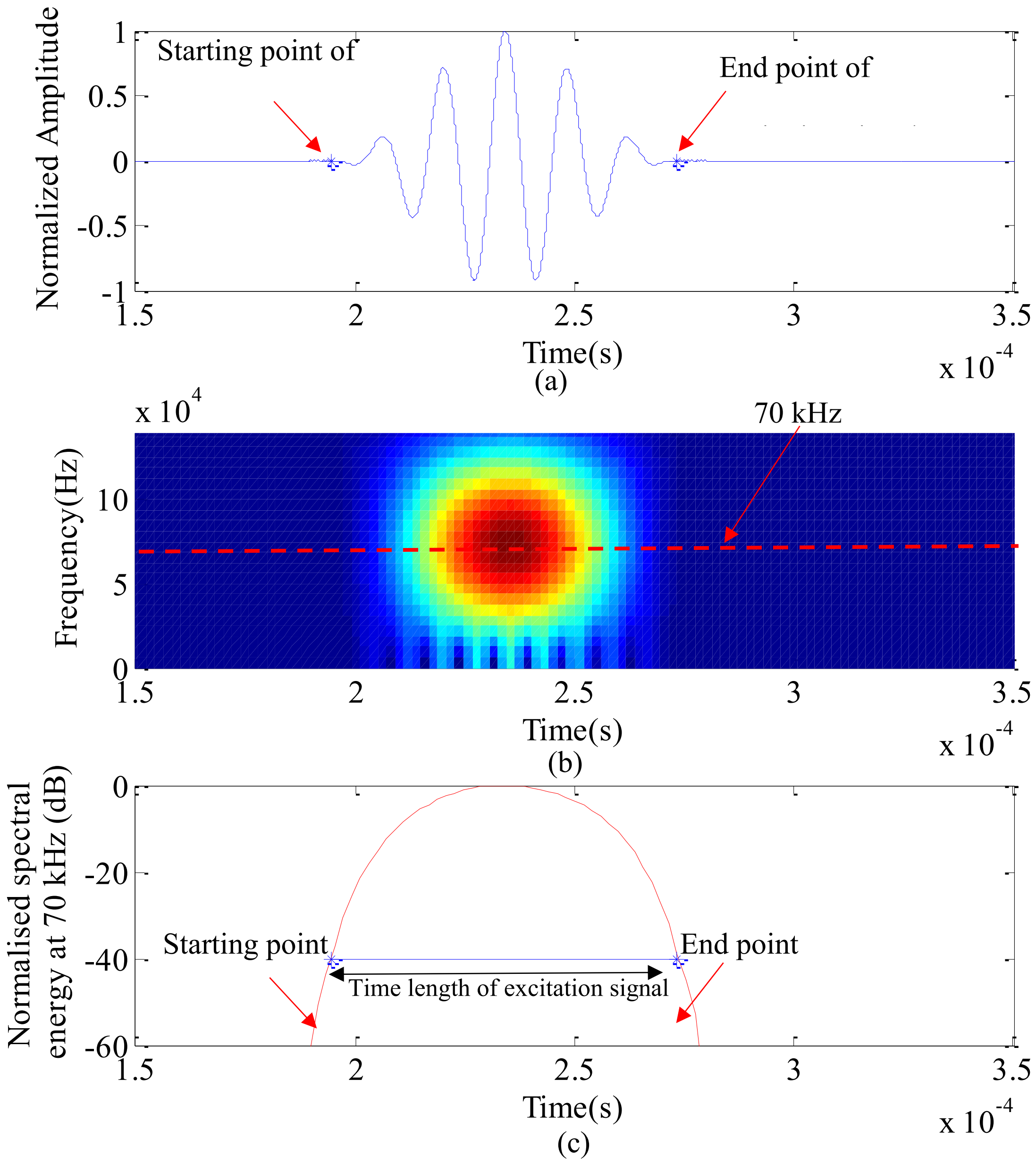

Figure 2.27 Excitation signal (5.5, 70kHz voltage signal) (a) time history (tone burst is shifted along time axis to match the location of main wave packet of time-reversed signal for direct comparison) (b) normalized instantaneous spectral energy distribution (c) normalized spectral energy time history at 70kHz in dB scale

Figure 2.28 and Figure 2.29 show normalized amplitudes of time-reconstructed signals in time domain and normalized spectral energy time history at 70 kHz in dB scale respectively for sensing path #6 and #7.

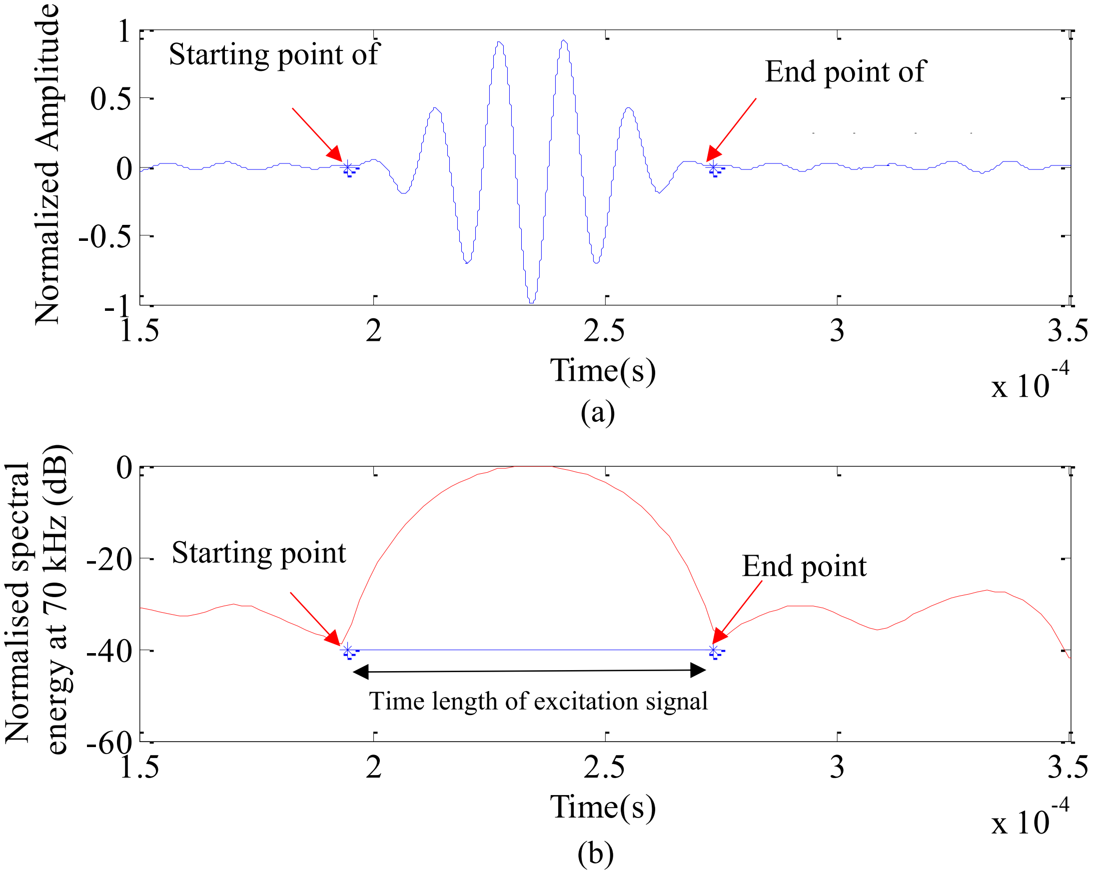

(a)

(b)

Figure 2.28 Time reversed signal obtained from sensing path #6 (a) time history (b) normalized spectral energy time history at 70 kHz in dB scale.

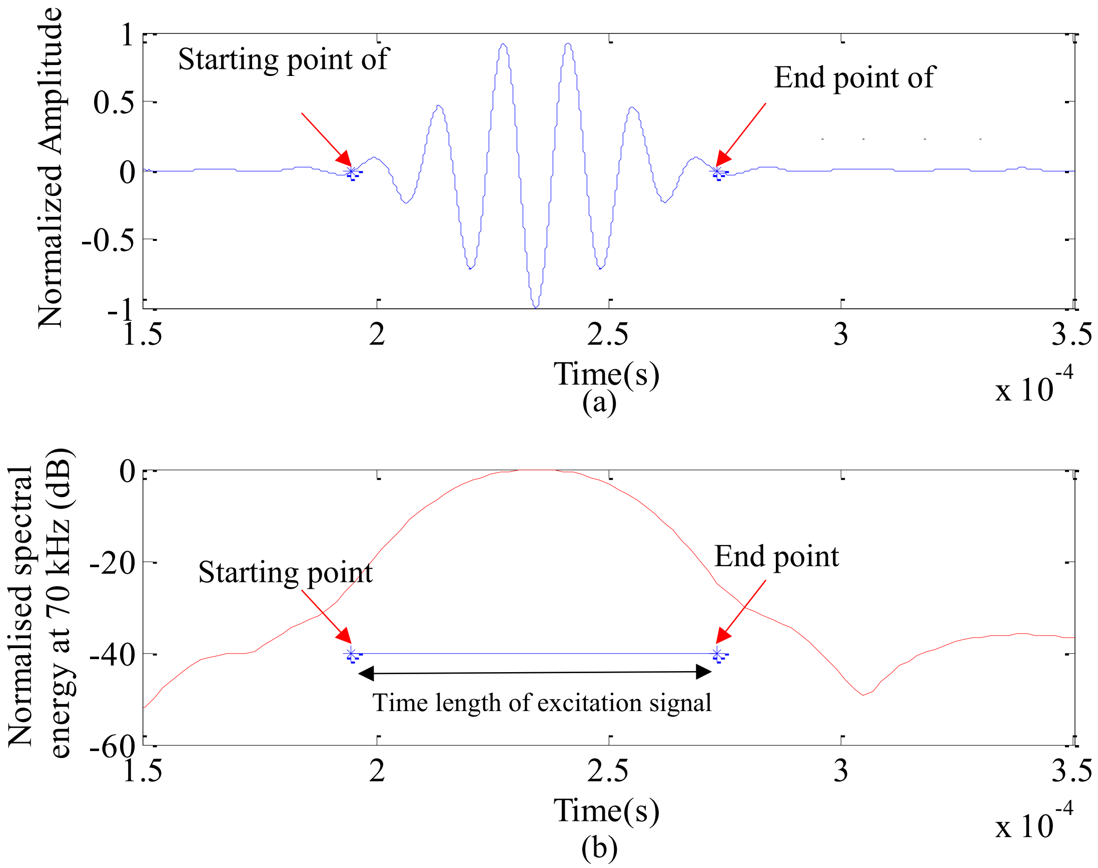

Figure 2.29 Time reversed signal obtained from sensing path #7 (a) time history (b) normalized spectral energy time history at 70 kHz in dB scale

If the time length of the main wave packet equals that of the excitation signal, the main wave packet is considered to be free of interference, and the signal path is potentially passing through the damage. Hence, those reconstructed signals are used for DI calculations. Similarly, if the time length of the main wave packet is notably different from the excitation signal, the main wave packet is considered to have an overlap with side wave packets, and those signals are excluded from DI calculations. In this particular example, the reconstructed signals from signal path #5 and # 6 have very close time lengths (main wave packet) to that of the excitation signal, and all of other reconstructed signals have considerably different time lengths. Therefore, reconstructed signals from signal path #5 and #6 are taken for damage index calculations. Table 2.2 presents the DI calculated for signal paths #5 and #6.

Table 2.2 Damage index values calculated for sensing path #5 and #6

Sensing location	DISP	DISP (no damage)
5	0.005	0.0014
6	0.002	0.0014

Above two DI value are higher than the DI calculated for the pristine structure which are 0.0014 and 0.054 for DISP and DIL2, respectively. Higher DI values indicate a presence of a damage along signal paths #5 and #6.

This technique is very suitable for the damages which resemble structural feature (linear damages). Note that the relative magnitude of the side wave packets produced by the damage corresponds to the severity of the damage. In this example, the relative magnitudes of the side wave packets are very small compared to the main wave packet. This indicates that the severity of the damage is very small (since it is bonded with a relatively soft adhesive film). However, despite the low severity of the damage, this technique is able to identify the damage path. Thus, this technique is also applicable when the damage is superficial, and the damage severity is relatively low. In other words, this technique increases the damage detection resolution of the MTR process and the procedure can be followed regardless of the nature of the damage.

In this particular example, no baseline wave propagation data for pristine structure is used. All the measurements are taken remotely from about 1-2-meter distance from the structure. The remote sensing capability is determined by the maximum stand-off distance for the LDV laser head. Additionally, the material properties and group velocities (influenced by temperature and loading conditions) are not needed to be taken into account for damage detection. The results are independent of the material properties of the structure, environmental conditions, and structural loading conditions. Further, the current actuator and sensing point configuration allows scanning of a wide area while using the minimum number of actuators and sensing points.

2.8 Conclusion of the chapter

In this chapter, the Modified Time Reversal (MTR) method along with non-contact sensing was used for structural damage detection. The MTR method does not require sensors to work as actuators and therefore non-contact measurement techniques may be used for MTR. Experimental and FE simulation results showed that a complete reconstruction of the excitation signal can be obtained from MTR by using the non-contact sensing of Lamb wave transverse velocity. The complexities arising from the multi-modal Lamb wave characteristics and the structural boundaries were discussed, and suitable equations were developed for the estimation of resulting errors. The equations were validated using experimental and FE simulation data. A major limitation of the conventional TR method (along with the conventional Damage Index formulations) is its incapability of detecting the linear damages. A novel frequency-time domain technique was introduced for the detection of the linear damages using the MTR method. Based on the current study, following conclusions are made:

1. A complete reconstruction of the excitation signal can be obtained from MTR method by using the non-contact sensing of Lamb wave transverse velocity.

2. The use of the transverse velocity eliminates the complexities arising from the multi-modal Lamb wave characteristics at lower frequencies. This is a major advantage of the MTR method over the conventional TR method.

3. The complexities arising from the structural boundaries cannot be eliminated completely. However, the use of the transverse velocity minimizes these complexities. Additionally, if the first packet of the forward moving wave is captured, the structural boundary effects are further reduced.

4. The proposed frequency-time domain technique is successful to identify the signal paths that contain linear structural damages. This technique would be suitable for the detection of damages that resemble the structural features in metallic structures (e.g., corrosion in large oil tanks). Additionally, this technique is particularly applicable when the potential damage is superficial, and the damage severity is comparatively low.

5. The proposed technique does not require baseline wave propagation data, and all the measurements are taken remotely. Additionally, the material properties and group velocities (influenced by temperature and loading conditions) are not needed for damage detection. Thus, this novel MTR method-based technique is independent from the material properties of the structure, environmental conditions, and structural loading conditions.

CHAPTER III

MODIFIED TIME REVERSAL METHOD FOR DAMAGE IMAGING

3.1 Introduction

The modified time reversal method operates in the pitch-catch configuration, and the structural damages located on the signal paths are detected through the DI values. Initially, the MTR method was developed for the detection of non-linear damages through the quantification of the main wave packet distortion [23] [2]. The main wave packet of the reconstructed signal which is compared with the excitation signal for the DI calculations, is distorted due the non-linearity of the damages located on the signal path, and due to the overlapping of the side wave packets. The structural damages which are located at a distance from the signal paths create side wave packets (similar to structural boundaries, as shown in Chapter *II*), and hence distort the main wave packet of the reconstructed signal. In Chapter *II*, we discussed how to avoid the overlapping of side wave packets. In contrast, in this chapter, the side wave packets are used to estimate the geometric location of the damages which are located at a distance from the signal paths. The equipment configuration for the estimation of the damage location using the MTR method is described below.

3.2 Equipment configuration

To implement the MTR method for the estimation of the damage location, the actuator and the sensor should be arranged in pitch-catch configuration. The reconstructed signal is obtained through six steps;

1. A narrow-banded wave is excited at an actuator at the location ***A***. This step initiates the "first-sensing cycle." The time length of the excitation signal should carefully be selected in order obtain a better spatial resolution.
2. The resulting wave motion (transverse velocity) is captured at ***B*** by an LDV. This step completes the "first-sensing cycle."
3. The recorded signal is then time reversed (i.e. $v_B(t) \rightarrow v_B(-t)$) and normalized with respect to the highest amplitude.
4. The time reversed signal is then given to the transducer ***A***, and a wave is excited at the location ***A*****.**
5. The resulting wave response (transverse velocity) is recorded at ***B*** using an LDV
6. The recorded signal at B is then time reversed. The resulting signal is called "reconstructed waveform." This step concludes the "second-sensing cycle."

The steps are shown in Figure 3.1.

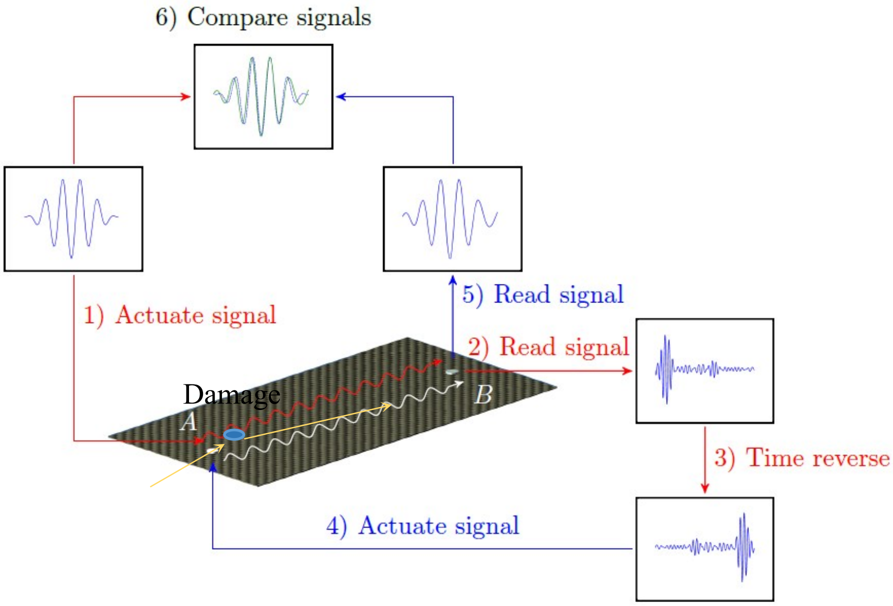

Figure 3.1 MTR for damage imaging

3.3 Side wave packets due to the structural damages

Let us consider the waves propagating in the structure shown in Figure 3.1. The Lamb waves are generated by transducer ***A*,** and the resulting wave motion is captured at ***B*** by an LDV. In contrast to the previous work, the damage is now located at a distant from the signal path. Suppose that the actuator produces only the A_0 wave mode. During the first sensing cycle, the LDV records the forward moving A_0 wave packet, and the reflected A_0 wave packet (shown in yellow arrows in Figure 3.1) due to the reflection at the damage. The direct and the reflected wave packets are recorded at ***B*** and time reversed. The time-revered signal is given to the actuator ***A*** as an excitation voltage. Such excitation produces corresponding A_0 and S_0 wave modes at the actuator resulting four wave packets. Each of these four wave packets result in two wave packets (direct, and reflection) at the sensing point ***B***. Consequently, a total of 8 (4-A_0, 4-S_0) wave packets appear in the reconstructed waveform. However, at least two Lamb wave modes exist at any given frequency. Therefore, for the fundamental Lamb wave, total of 16 wave packets constitute the reconstructed waveform. The time-location of each wave packet for a general Lamb wave can be formulated as follows.

For Eq. (3.1), Eq. (3.2), and Eq. (3.3), following notation is used. The superscripts ***D*** and ***R*** indicate the direct wave packet and the reflected wave packets, respectively. The subscripts A_P, and S_m represent the $\boldsymbol{p^{th}}$ *A* mode, and the $\boldsymbol{m^{th}}$ *S* mode, respectively. The subscript A*p*A*p* indicates the A_p wave packet of the reflected A_p wave packet. The terms ***L***, $\boldsymbol{d_1}$ and $\boldsymbol{d_2}$ are the distance between actuator and sensing point ***B***, the distance between the actuator and the damage, and the distance between the damage and sensing point ***B***, respectively. The time-location of *A* and *S* wave packets in the first sensing cycle are given by Eq. (3.1) and Eq. (3.2), respectively.

$$t^{D}_{A_pA_p} = \frac{L}{C_{Ap}}, \; t^{R}_{A_pA_p} = \frac{d_1}{C_{Ap}} + \frac{d_2}{C_{Ap}} \tag{3.1}$$

$$t^{D}_{S_mS_m} = \frac{L}{C_{Sm}}, \; t^{R}_{S_mS_m} = \frac{d_1}{C_{Sm}} + \frac{d_2}{C_{Sm}} \tag{3.2}$$

If the wave is recorded for T_1 seconds during the first sensing cycle and T_2 seconds during the second sensing cycle, the time locations of various wave packets in the reconstructed waveform are given by Eq. (3.3).

$$t = T_2 - T_1 + (t^{i}_{x_jx_j} - t^{u}_{y_ky_k}) \tag{3.3}$$

$x, y \in [A, S], i, u \in [D, R]$, $j, k \in [0,\ldots\ldots, n_S]$ for *S* modes, $j, k \in [0,\ldots\ldots, n_A]$ for *A* modes.

Note that the reconstructed signal of the directly sensed wave packets converge at $T_2 - T_1$ resulting in the main wave packet. The time-location of the main wave packet is independent of the group velocities and the distances (***L***, d_1 and d_2). The reflected wave packets produce side wave packets, depending on the group velocities and the distances. However, some of the reflected wave packets which satisfy, $t^{i}_{x_jx_j} = t^{u}_{y_ky_k}$ relationship also converge at $T_2 - T_1$. Thus, generally, the main wave packet of the reconstructed waveform is composed of waves which satisfy $t^{i}_{x_jy_k} = t^{u}_{x_vy_w}$ relationship, including some of the reflected wave packets.

In the lower frequencies, the A_0 wave mode particle motion resembles that of the flexural waves [3], and S_0 wave mode particle motion resembles that of the axial waves. Additionally, the A_0 wave amplitude is considerably larger than S_0 wave amplitude, at lower frequencies. Since we measure the transverse velocity (particle motion) of the Lamb waves using the LDV, the measured A_0 wave amplitude is significantly higher than that of S_0 wave. Hence, the presence of the S_0 wave mode can be ignored (in low frequencies), and the Eq. 3.3 is simplified as follows;

$$t = T_2 - T_1 \pm (t^{i}_{A_0A_0} - t^{u}_{A_0A_0}) \tag{3.4}$$

$$i, u \in [D, R]$$

Eq. 3.4 calculates the time location of all the wave packets on the reconstructed waveform. Given the value of L, d_1 and d_2, the time-location of each wave packet can be calculated. The distance between the actuator and the sensing point, L is fixed for each sensing point. However, the distances associated with the damage, d_1 and d_2, are unknowns. Conversely, if the time-location of each wave packets is known, d_1 and d_2 can be calculated. Eq. 3.4 produces four different relations as follows;

$$t = T_2 - T_1 + (t^{D}_{A_0A_0} - t^{D}_{A_0A_0}) = T_2 - T_1 \tag{3.5}$$

$$t = T_2 - T_1 + (t^{R}_{A_0A_0} - t^{R}_{A_0A_0}) = T_2 - T_1 \tag{3.6}$$

$$t = T_2 - T_1 + (t^{R}_{A_0A_0} - t^{D}_{A_0A_0}) \tag{3.7}$$

$$t = T_2 - T_1 - (t^{R}_{A_0A_0} - t^{D}_{A_0A_0}) \tag{3.8}$$

The solution of Eq. 3.5 and Eq. 3.6 calculate the time location of the time reversed direct wave packet sensed in first sensing cycle and the time reversed reflected wave packet sense in first sensing cycle, respectively. These wave packets coverage at T_2-T_1 and creates the main wave packet. Eq. 3.7 and Eq. 3.8 are corresponding to the side wave packets which are symmetrical around the main wave packet.

3.4 Deduce the damage location from side wave packets

The terms d_1 and d_2 specifies location of the damage, which can be calculated from the inverse of Eq. 3.7 or Eq. 3.8. However, a unique solution does not exist for d_1 and d_2. Therefore, a set of values of d_1 and d_2 which satisfy the Eq. 3.7 (or Eq. 3.8) is calculated. Consider the Figure 3.2.

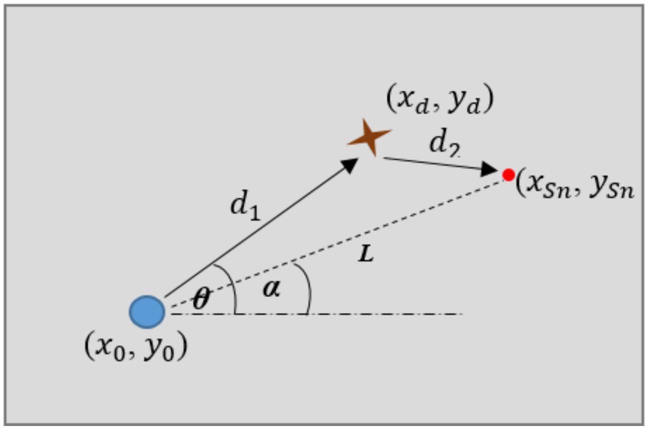

Figure 3.2 Damage location calculation

The damage location (x_d, y_d) is given by Eq. 3.9

$$x_d = d_1 \cos(\theta) , y_d = d_1 \sin(\theta) \text{ , where} \tag{3.9}$$

$$d_1 = \frac{S^2 - x_{sn}^2 - y_{sn}^2}{2S - 2x_{sn}\cos(\theta) - 2y_{sn}\sin(\theta)} , S = C_{A0}\left(T_1 + \frac{L}{C_{A0}} - t\right)$$

Eq. 3.9 is used to determine the location of a damage (through hole) in an aluminum plate. The experimental setup (which is identical to the experimental set up shown in Figure 2.16) comprises of a 1.2mm thick, rolled formed, 6000 series aluminum plate with a drilled hole (shown in Figure 3.3) and a disc type piezoelectric transducer (material: SM412) permanently bonded to the plate. The actuator has dimensions of 12mm diameter and 0.5mm thickness. The excitation voltage is generated by Agilent 33220A function/arbitrary waveform generator (5Vpp) and amplified by A.A Lab Systems' A303 high voltage amplifier and modulator (up to 100Vpp). A LDV (Polytec OFV-5000 with OFV-500 laser head) is used to record the transverse velocity at the sensing points. The plate size is selected sufficiently large, so that boundary reflection effects are minimized. Four sensing points are employed (namely, $\boldsymbol{S_1}$, $\boldsymbol{S_2}$, $\boldsymbol{S_3}$ and $\boldsymbol{S_4}$) for LDV wave measurements.

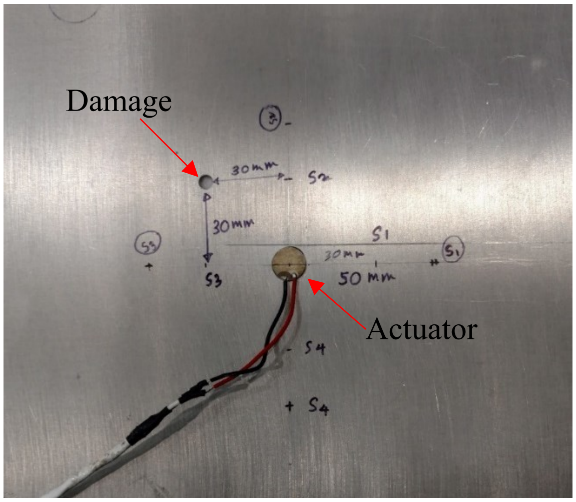

Figure 3.3 Damaged Al plate used for MTR based damage imaging

First, the MTR method is conducted at $\boldsymbol{S_1}$ sensing point. The wave motion captured during the first sensing cycle is shown in Figure 3.4. The wave motion captured during the first sensing cycle is used for the calculation of the instantaneous wave velocity (C_{A0}). Note that this is an isotropic specimen and therefore, the wave velocity does not change with the direction. However, if the test specimen is anisotropic, a slowness diagram (instantaneous) should be constructed. As mentioned previously, since the inspection is conducted in low frequencies (as well as LDV is employed for the wave measurements), the S_0 wave mode does not appear in the recorded wave motion. For this particular situation, the instantaneous wave velocity is calculated as 1720 ms^{-1}. The instantaneous velocity is not a fixed value, and changes with the environment and loading conditions. The wave signal captured during the first sensing cycle is time reversed, normalized, and given to the piezoelectric transducer. The resulting wave motion is captured. The reconstructed wave is shown in Figure 3.5. The time location (t) of the side wave packet on the reconstructed signal is measured. For this particular problem, T_1 = 126.6μs and t = 23 μs (Eq. 3.7).

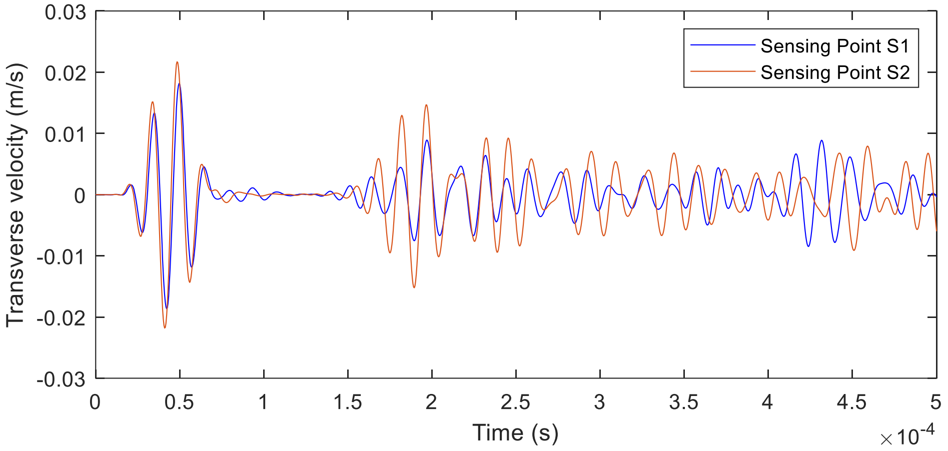

Figure 3.4 The wave motion captured during the first sensing cycle

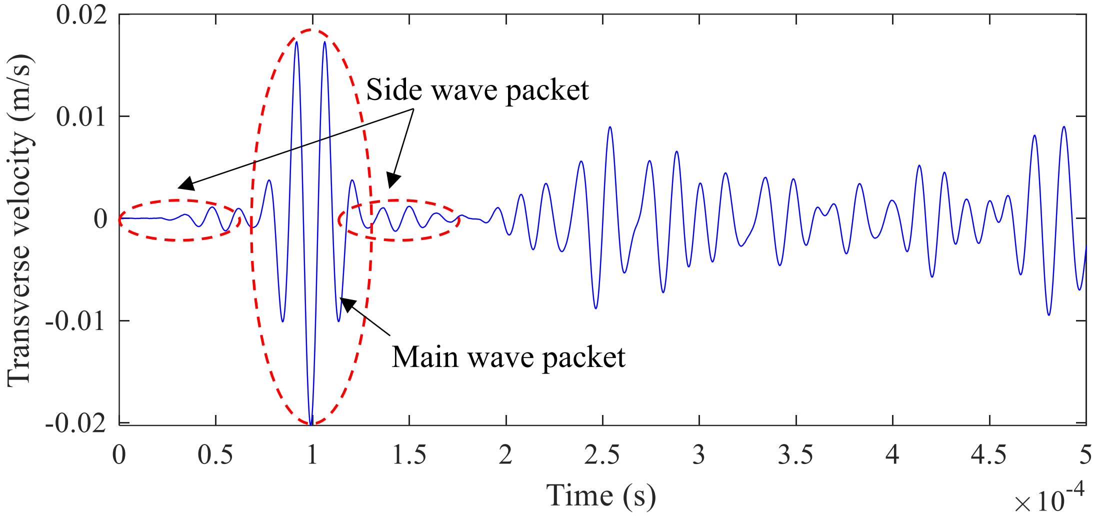

Figure 3.5 Reconstructed wave for sensing point 1

The time location of the main wave packet does not depend on the damage location or the sensing locations. The side wave packets are symmetrically distributed around the main wave packet. The possible damage location is then calculated using Eq. 3.9, where, the value of $\boldsymbol{\theta}$ is varied from 0 to 360 degrees. As mentioned above, the solution (damage location) is not unique.

This is due to the fact that the structural damages which are located in different locations may produce the side wave packets which have the identical time location on the reconstructed wave signal. The intensity of the damage is assumed be maximum at the points calculated from Eq.3.9, and the damage intensity is assumed to have a normal distribution around that point. The standard deviation of this normal distribution is selected arbitrary in order to develop damage images. The possible damage locations calculated for sensing point S_1, S_2, S_3 and S_4 are given in Figure 3.6.

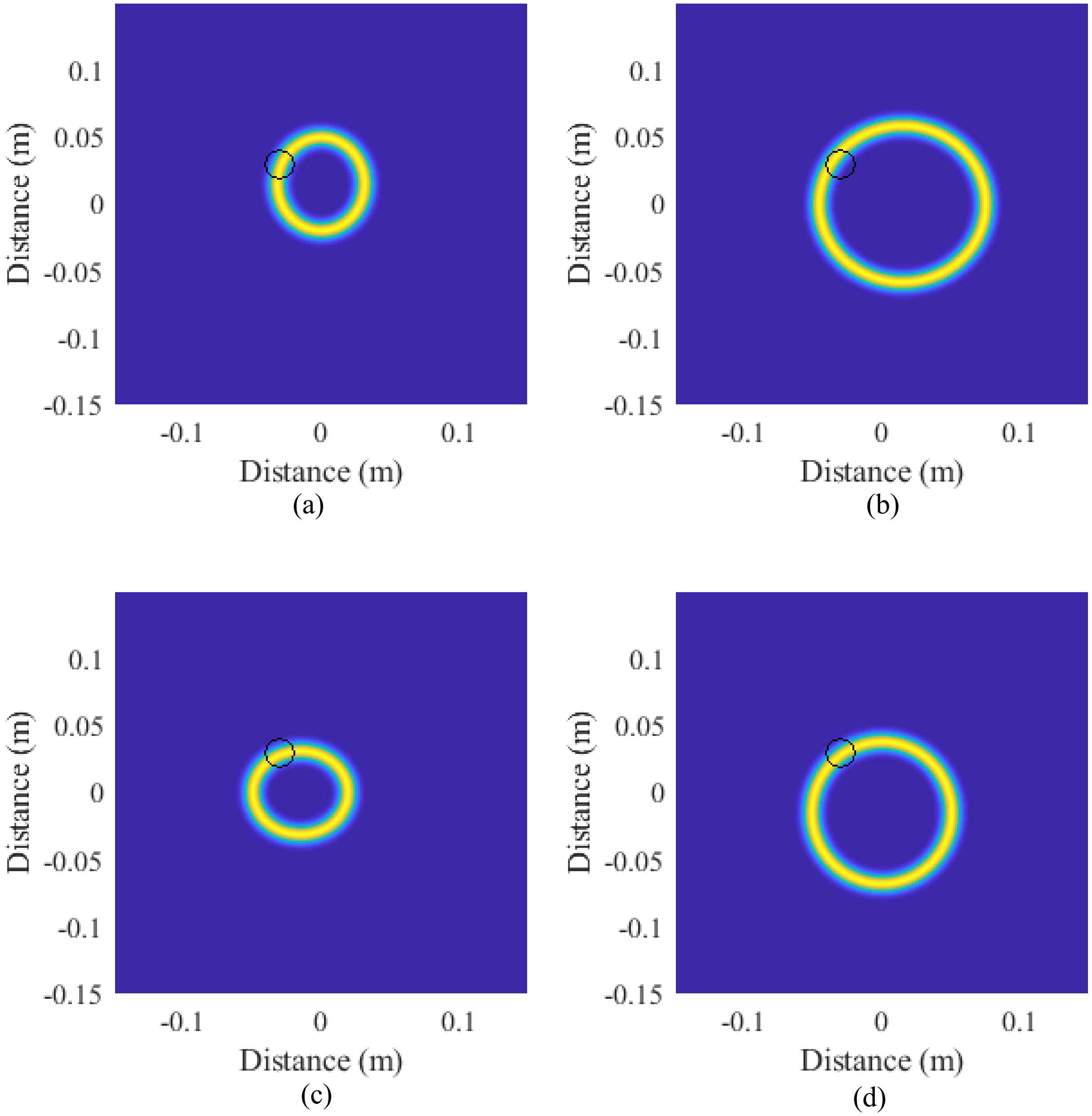

(a)

(b)

(c)

(d)

Figure 3.6 The possible damage locations calculated for sensing point (a) S_1, (b) S_2, (c) S_3, (c) S_4

According to the above figures, each sensing point produces a unique ellipse. The intersecting point of these ellipses yields the actual damage location. The damage intensity distributions calculated from each sensing locations are cumulated for the construction of the final damage image. The intensity/severity of complete damage image is given by Eq. 3.10.

$$D_{Total}(x,y) = \sum_{i}^{n} D_i(x,y) \qquad 3.10$$

The term D_{Total} is the damage intensity of the final damage image, and D_i is the damage intensity of each damage intensity distribution (ellipse) generated by each sensor. The term $\boldsymbol{n}$ is the number of sensors employed. The final damage image is given in Figure 3.7.

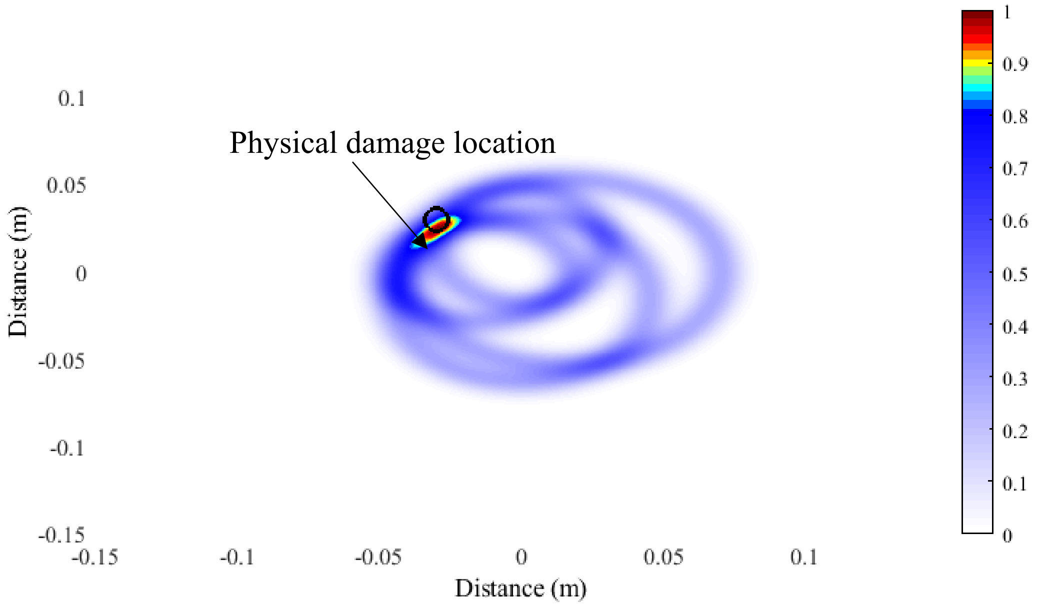

Figure 3.7 Resulting damage image

The applicability of this technique is tested using FEA models. Two examples are given below where the damage images of a drilled hole and a vertical crack are generated (Figure 3.8 and Figure 3.9).

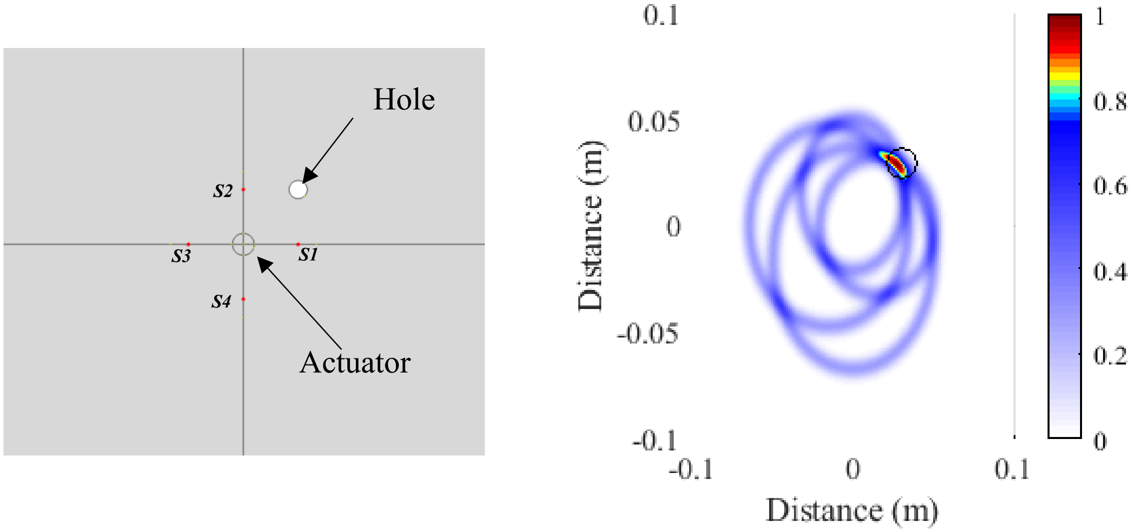

Figure 3.8 (a) FE modal of a drill-hole (b) Damage image. The sensing locations are shown using red dots

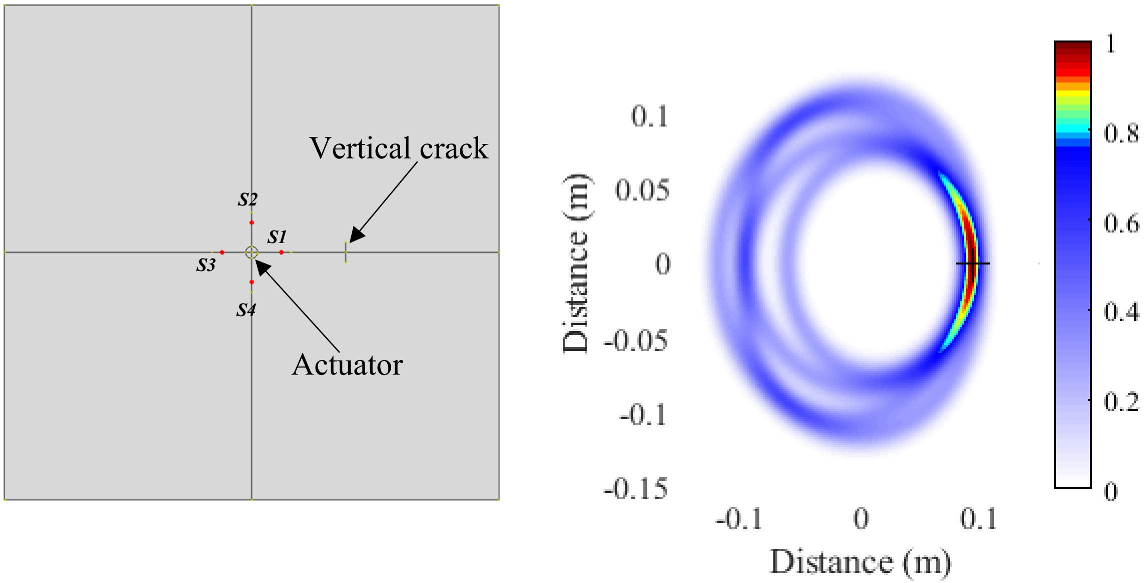

Figure 3.9 (a) FE model of a vertical crack (b) Damage image. The sensing locations are shown in red dots

3.5 Advantages of MTR for damage imaging

The MTR based technique does not require a baseline for the comparison with the current wave motion data for the characterization of possible damages. Unlike the conventional MTR method, this technique scans the damages located at a distance from the signal paths. Therefore, a large area is scanned with a minimum number of scanning points, resulting a significant reduction in the inspection time. As shown above, the velocity of the Lamb wave is required for triangulation of the damage location. However, the instantaneous wave velocity is measured during the first sensing cycle. Therefore, the environment and loading conditions do not influence the solution.

In this technique, an LDV is employed for the record of transverse velocity of the Lamb wave motions at sensing points. The coordinates of the sensing points are specified with respect to the actuator location. The LDV has a certain spatial accuracy (accuracy of aiming the laser point), and the true sensing point may deviate from the specified sensing point by few millimeters. The amount of the spatial deviation of the true sensing point from its intended location, depends on the accuracy of the laser beam pointing systems (in this particular situation, the laser beam is pointed to the designated sensing points manually). Generally, the spatial accuracy decreases as the distance between the structure and LDV increases. In the inspection techniques which utilize baselines, the baseline wave motion is measured and recorded on certain sensing points. During the inspection, the current wave motion is recorded again on these particular sensing points. Subsequently, the captured current wave motion is compared with the baseline wave motion. A spatial deviation between the sensing point of baseline wave motion and the sensing point of the current wave motion may produce significantly different waveforms (even when structural damages do not exist). This may trigger false alarms. Consider the example given below;

Figure 3.10 shows a FE model of an aluminum plate with no structural damages. A Lamb wave is generated with 3.5 cycle, 50 kHz excitation signal. Figure 3.11 presents the transverse velocity of the wave motions captured at $\boldsymbol{S_1}$, $\boldsymbol{S_2}$, and $\boldsymbol{S_3}$ sensing points. The coordinates of $\boldsymbol{S_1}$ is (0.1m, 0m) with respect to the actuator location (0 m, 0 m). The distance between $\boldsymbol{S_1}$ and $\boldsymbol{S_2}$ is 1mm, and the distance between the $\boldsymbol{S_2}$ and $\boldsymbol{S_3}$ is 1 mm.

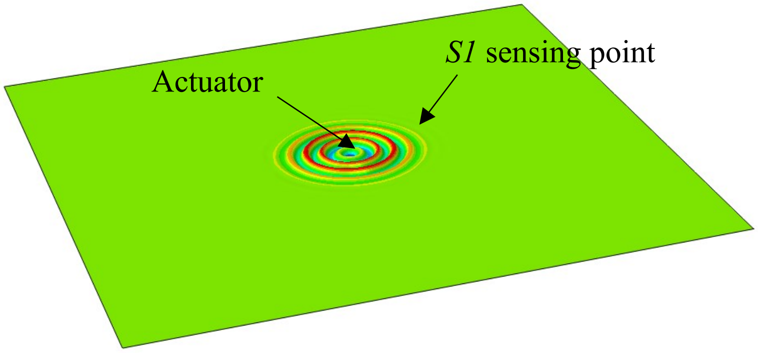

Figure 3.10 Wave propagation in the FE model

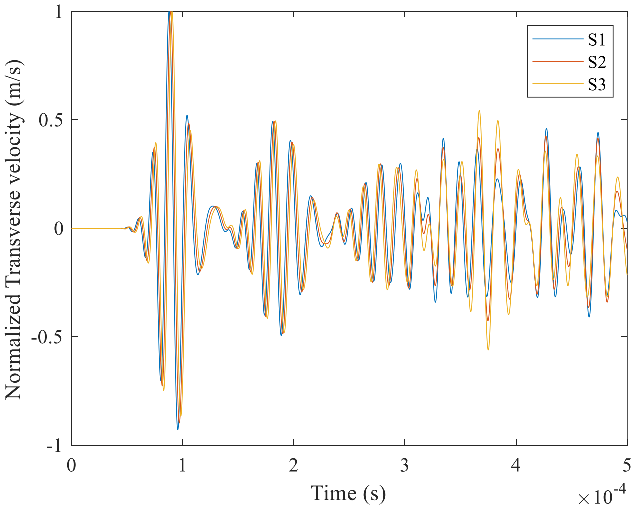

Figure 3.11 Recorded signals at S_1, S_2 and S_3

Figure 3.12 presents the numerical difference between the wave motion captured at S_1 and the wave motion captured at S_2. According to the figure, even though the two sensing points are very close to each other, the difference between the wave motions is considerable (about 55% of the wave motion maximum amplitude). On the other hand, MTR method do not use any baseline for the comparison. Therefore, false alarms due to the spatial deviation of the sensing points are not created.

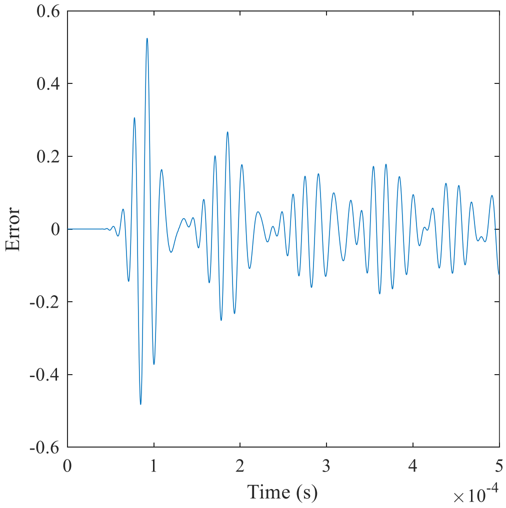

Figure 3.12 The numerical difference between the waveform measured at S1 and S2

3.6 Conclusion of the chapter

In this chapter, the modified time reversal method was used to estimation the geometric location of structural damages. The structural damages which are located at a distance from the signal paths create the side wave packets on the reconstructed waveform. The side wave packets were used to estimate the geometric location of the damages which are located at a distance from the signal paths. The time-location of the side wave packets in the reconstructed waveform were correlated with the damage location, and adequate equations were developed. The equations were then used to determine the location of a damage (through hole) in an aluminum plate, and a two-dimensional damage image was developed. The technique successfully predicted the true location of the damage. The applicability of the technique was further tested using a FEA model of plate with a drilled hole and a FEA model of a plate with a vertical crack. The damage locations of the FEA models were successfully predicted by the technique. Based on current study following conclusions are made.

1. The proposed MTR method-based technique is capable in predicting the damage location with a reasonable accuracy.
2. The technique is baseline free. Therefore, the solution does not depend on the environmental and loading conditions.
3. The technique is capable of scanning a large area with a minimum number of sensing points. Therefore, the inspection time is considerably reduced.
4. This technique is particularly suitable for non-contact inspection.
5. The technique is not capable of predicting the locations of multiple damages and may produce inaccurate results for the structures which have multiple damaged sites.

CHAPTER IV

MODEL BASED STRUCTURAL HEALTH MONITORING

4.1 Introduction

In the model based structural health monitoring, an analytical, semi-analytical, and numerical structural models are used for the generation of wave propagation data. Similar to the MTR method, the model based structural health monitoring techniques eliminate the need for the baseline data recorded for various environmental and loading conditions. The model based SHM are conducted in two different approaches: the forward (direct) problem approach and the inverse problem approach. In the forward problem approach, the structure is modeled numerically/analytically in its pristine conditions. The structural model is then utilized for the generation of baseline wave propagation data. The input variables of these structural model may include the mechanical properties, the physical parameters of the structure, and the excitation signal profile. The models generate the wave propagation corresponding to the given input variables. The mechanical properties (e.g. elastic modulus, density, etc.) of the constituent materials of the structure may be experimentally obtained as functions of the environment conditions (e.g. Elastic modulus as a function of temperature). The input variables of the model may be adjusted according to the current (instantaneous) environment condition. The numerical/analytical model along with the environment-dependent input variables are then used to generate the baseline wave propagation data. Hence, the baseline data (instantaneous) is a function of the instantaneous environmental condition. For the damage detection, the wave propagation of the physical structure (current wave propagation data) is recorded, and then compared with the model generated, environment-dependent, baseline data (instantaneous baseline data). Depending on the data processing technique, presence of damages, damage severity and the damage location may be determined through a comparison conducted between the modeled generated baseline data and the current wave propagation data.

In the inverse problem approach, the physical structure is numerically/analytically modeled in its damaged condition. The type of the damage, damage location and the severity (size) are treated as input variables. The simulated wave propagation data for the damage structure is then generated from this damaged model. The wave propagation data of the physical structure (possibly damaged) is recorded. The recorded wave propagation data is then compared with the model (damaged) generated wave data. The wave propagation simulation is repeated by varying the input variables (damage type, size, and location) until the model generated wave propagation data resembles the physical wave data. The optimization algorithms and the artificial neural networks are widely used to determine the inverse problem solution.

Generally, the inverse problem approach is complex and time-consuming compared to the forward problem approach. However, the inverse problem approach provides a complete description of the damaged structure. Hence, the subsequent signal processing and interpretation for the characterization of possible damages are not required. Therefore, the inverse problem approach is particularly popular for the damage detection of the structures. In this chapter, we use inverse problem approach for damage detection of adhesively bonded joints.

4.2 Adhesively Bonded Joints

Adhesively bonded joints provide a range of favorable properties compared to the conventional mechanical fastenings. The larger stress bearing area, higher fatigue resistance, light weight, ability to join thin components, ability to join dissimilar materials, better sealing, and better damping are some of the favorable properties offered from the adhesive bonded joints [35] [36]. The adhesive joints are also less labor and cost intensive. Due to its higher strength to weight ratio, the adhesive joints provide lightweight attachment methods for metals, carbon polymer composites, and honeycomb structures [37]. On the other hand, the adhesively bonded joints inherit a number of limitations including the longer cure time, difficulties in the inspection of the finished joint, and the environmental effects on the bond stiffness and the strength [37]. However, the advantages of the adhesively bonded joints outweigh their limitations, and hence, the adhesively bonded joints are increasingly used in modern aircrafts. Current aircraft certification necessitates the conformation that the adhesively bonded joints do not fail and cause structural failure at the critical design loads, and requires the use of mechanical fasteners along with adhesive [36]. The use of comparatively heavy metal fasteners along with the adhesive layer significantly undermines the full realization of the bonded joints advantages. An inspection technique, which is capable of detecting the damages during the manufacturing stage and the service life, is critically important for the continued safe operation of adhesively bonded structures.

Non-Destructive Evolution (NDE) and Structural Health Monitoring (SHM) techniques are widely used for the inspection of structural damages. Adhesively bonded joints inherit several distinct damage/defect types. Therefore, the NDE/SHM of adhesively bonded joints is relatively complicated. The adhesive layer damages are categorized as weak bonds, cohesive defects and gross defects [38]. Poor surface preparation, surface contamination, and erroneous bonding and curing processes produce weak bonds [39]. The cohesive defects relate to the mechanical properties of the adhesive, and mostly attribute to erroneous mixing and curing processes [9]. The gross defects account the micro to macro scale defects on the adhesive layer (e.g. micro cracks and voids) [5]. A fairly complete review of state-of-the-art nondestructive evaluation of adhesive bond quality can be found in [7]. Various NDE techniques that can be used in bonded joints inspection can be found in [8]. A number of NDE/SHM techniques have been proposed for the inspection of adhesively bonded joints, and particularly, the Lamb wave propagation based NDE/SHM inspection techniques have been identified to be promising. The Lamb waves permit long-range through thickness detection of damages, and hence ideal for the adhesively bonded joint inspection.

Several researches have been conducted for the detection of the cohesive damages (variation of adhesive properties). Ong et al. [40] measured the elastic modulus and the Poisson's ratio using Lamb wave dispersion curve fitting. Experimental Lamb wave propagation data (spectral domain) were compared with the wave data generated from a two-dimensional Finite Element (FE) model. A good agreement between experimental dispersion curve and FE dispersion curve is obtained by varying the properties of the FE model. The adhesive properties which yielded the best agreement between the experimental and analytical dispersion curves, were identified as the current properties of the adhesive joint (possibly defective or aged). Koreck et al. [41]also used a FE model and showed that the Local cross points and minima of the dispersion and slowness curves vary with the adhesive properties and thickness. Analytical models have also been reported [42] to be used for the dispersion curve generation. Additionally, use of semi-analytical model has been reported in [43] and [44]. Gauthier et al. [45] developed an adhesive joint model of which the interface between the adhered and the adhesive defined as a series of tension and shear springs. The level of the adhesion between the adhesive and adherend is specified by the spring stiffness. The higher order wave modes were observed to be more sensitive to interfacial stiffness. Hong-Xiang et al. [46] identified that the fundamental anti-symmetric (***A_0***) Lamb wave mode is more sensitive to the adhesive layer properties compared to the fundamental symmetric (***S_0***) Lamb wave mode. Heller et al. [9] utilized dispersion curves for the characterization of aged adhesive joints. As a result of the aging, the higher order wave modes disappeared in the dispersion curve.

A number of researches have been conducted for the detection of adhesive debonds. Ong et al. [47] showed that the dispersion characteristics have a negligible effect from the debond. However, the amplitude (which relates to the intensity of the dispersion curve) decreased due to the scattering at the debond. Okabe et al. [48] recorded the Lamb wave propagation using fiber bragg grating (FBG) and correlated the debond size to a damage index (using baseline). In order to avoid the use of baseline for the detection of debonds, Lin et al. [49] proposed to compare the travel time of Lamb waves between two adherends. The debond created a delay in the wave transmission between two adrends, and the delay is observed to be increasing with the debond size. A completely disbonded area between the adhesive and adrerend creates a kissing bond and generates the harmonics of the excitation frequency. This non-linear wave propagation is utilized for the detection of debonds. However, detection of kissing bonds depends on the transverse contact pressure applied between the interface surfaces [18]. The detection of bulk defects (e.g. micro-voids) are considerably difficult since the dimensions of bulk defects are considerably smaller than the wavelength of Lamb waves. Researches have not been reported for the detection of bulk defects using the Lamb wave propagation.

In this chapter, we use an inverse problem approach for the detection and estimation of major the damage types possible in an adhesive joint (cohesive damages, micro voids, debonds, and weak bonds). The solution of the inverse problem is obtained from an optimization algorithm. A number of researches which utilize the optimization algorithm-based techniques have been reported in literature. However, in this work, the optimization algorithm is utilized along with the Wavelet Spectral Finite Element (WSFE) models [35], for the first time. The WSFE models are significantly faster than the conventional FE models, and therefore, a significant reduction of the computational time is achieved. The solution of an inverse problem is obtained through an iterative process, and in each iteration, the wave propagation along the adhesive joint is calculated. Consequently, the computational time reduction gained from WSFE model in each iteration, accrues. Therefore, a significant reduction of the solution time is achieved. In the proposed inverse problem technique, we reduce the global optimization problem into a local optimization problem, and hence a computationally inexpensive local optimization algorithm is used. Additionally, most of the reported researches performed the optimization in spectral domain. These procedures require the record of the wave motion at multiple data points (128 points or more). On the other hand, the proposed inverse problem technique requires a single data point for the inspection of entire width of the adhesive layer. As a result, a significant reduction of data acquire/measuring time is saved. This results a significant reduction of the inspection time (aggregation of measurement time and computation time). The use of this technique in industry as a quality assurance (during the manufacturing stage) and inspection tool (during the operational life) is also presented.

4.3 Examination of the stress components in a single lap joint

The stress components along a Single Lap Joint (SLJ) is examined using a generic FE model. The adherends and the adhesive layer are modeled with the fully integrated 8-node hexahedral elements, and five (5) through-thickness elements are used. The interface between the adherend and adhesive is established by sharing the contacting nodes, and a perfect-bond condition is assumed. An axial tension load is applied to SLJ. The loading configuration and the boundary conditions are shown in Figure 4.1 (a). Due to the load path eccentricity, the applied axial forces create a bending moment, a large transverse deflection is produced. The resulting deformed SLJ is shown in Figure 4.1(b). Goland and Reissner's analysis first reported this geometric non-linearly [50]. Cooper et. al. [50] compared Goland and Reissner's theory with the FE and experiment results, and a very good correlation is demonstrated.

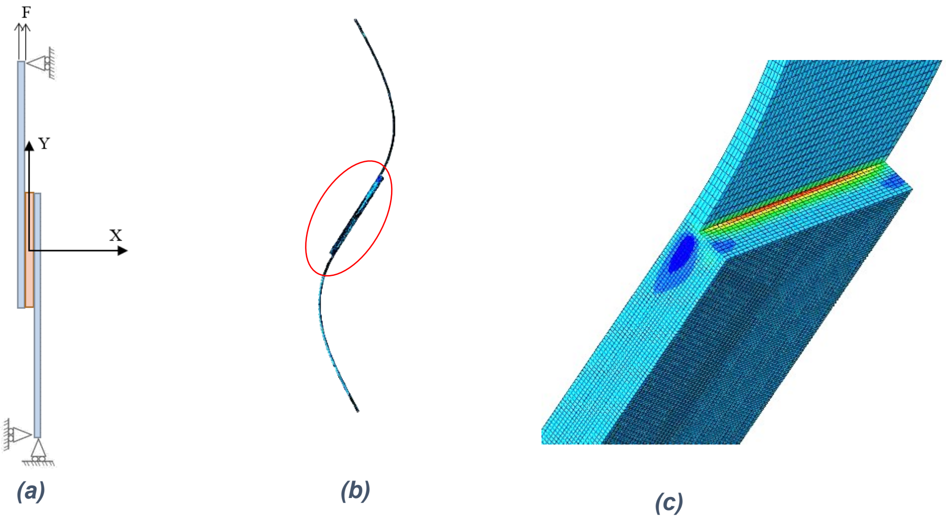

Figure 4.1 (a) the boundary conditions are loading configuration, (b) the deformed SLJ model, (c) the stress (σ_{xx}) distribution near the free edge

Figure 4.2(a) shows the transverse normal stress (σ_{xx}) variation along the adhesive joint obtained from the FE model. σ_{xx} is responsible for the transverse peeling of the adhesive from adherend, and the free ends of the adhesive joint have the highest peel stresses. The interfacial shear stress (τ_{xy}) is shown in Figure 4.2 (b). τ_{xy} is responsible for the interfacial shear failure. The free ends of the adhesive layer satisfy the traction free boundary conditions. Therefore, the shear stress at the end of the adhesive layer vanishes. However, shear stress reaches the highest value at the vicinity of free ends.

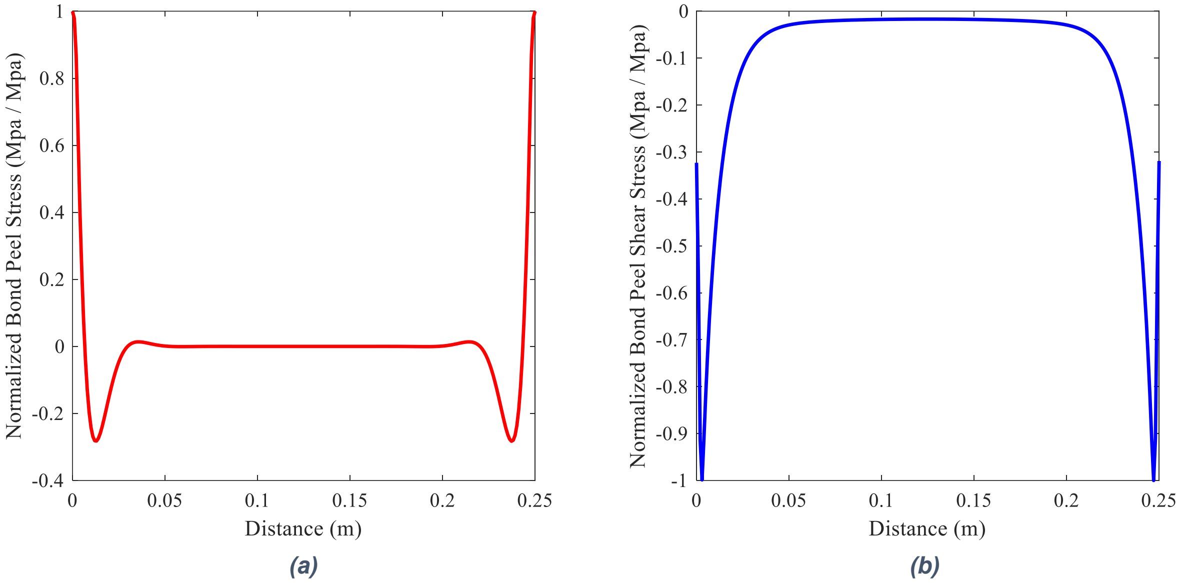

Figure 4.2 (a) Normalized bond peel stress variation, (b) Normalized shear stress variation

4.4 Correlation between the cohesive defects and the stress levels

The cohesive defects relate to the mechanical properties of the adhesive layer and resulted from an erroneous manufacturing process [9] or environmental degradation [51]. The stress levels of an adhesive layer are generally governed by the forces applied on the SLJ. However, due the load path eccentricity, the elastic modulus and the thickness of the adhesive layer also influence the stress levels. The axially loaded FE analysis is performed again by varying the adhesive layer elastic modulus. The peel, shear stress, and axial stress variations corresponding to the adhesive elastic modulus changes, are shown in Figure 4.3 (a) , Figure 4.3 (b), and Figure 4.4 (a) respectively. Note that all the stress component are normalized using the corresponding maximum absolute stress values. E_d is the design adhesive elastic modulus.

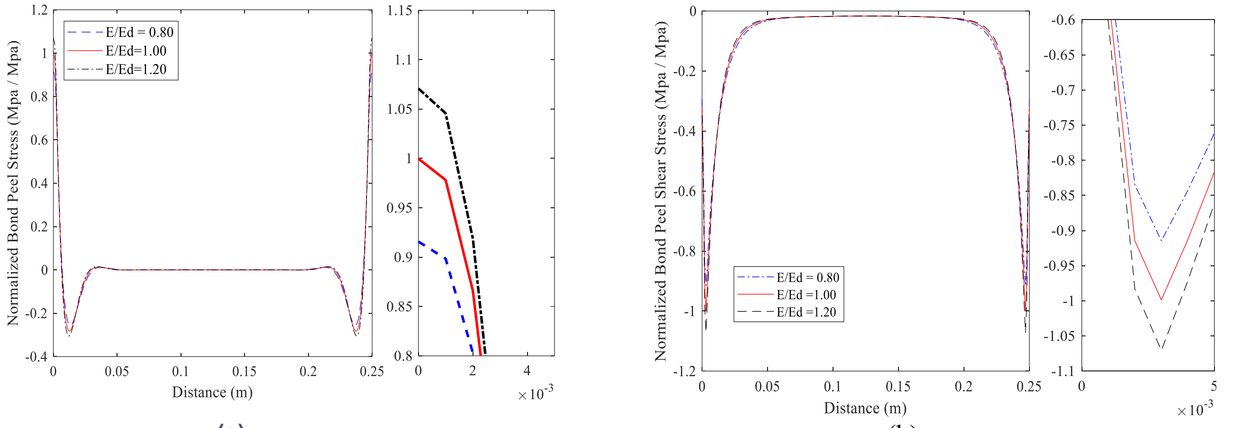

(a)

(b)

Figure 4.3 (a) normalized peel stress variation with the elastic modulus, (b) normalized shear stress variation with the elastic modulus

As shown in figures all the stress components rise as the adhesive elastic modulus increases. As shown in Figure 4.4(b), the reduction of bond line thickness also increases the stress components. However, the stress increases due to the thickness changes are not significant compared to that corresponds to the elastic modulus variation.

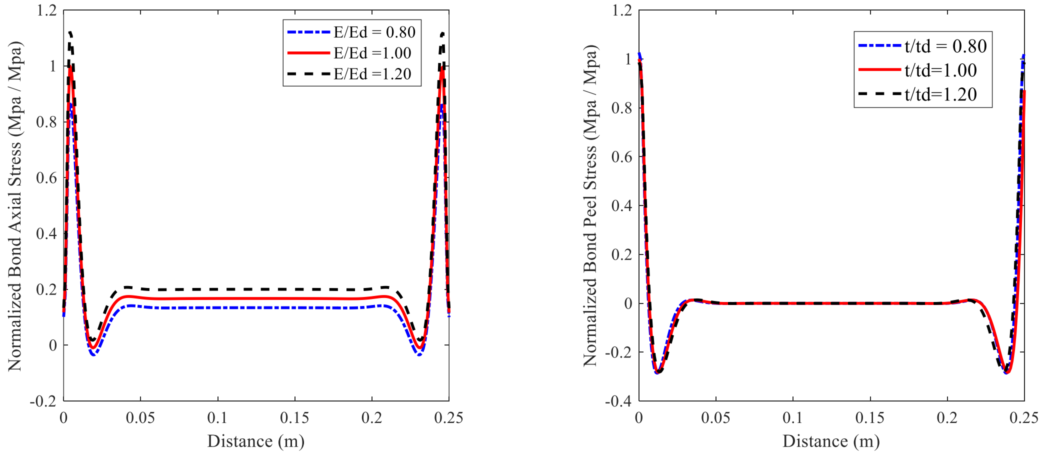

(a)

(b)

Figure 4.4 (a) Normalized axial variation with the elastic modulus, (b) Normalized bond peel stress variation with the bond line thickness

A number of failure criteria have been proposed for SLJs. These criteria are divided in to two categories: critical stress based failures [52], and Linear Elastic Fracture Mechanics (LEFM) based failures [53] [54]. In critical stress-based failure criteria, a bond between adhesive and the adherand fails once the stress components reach their critical values. In LEFM based criteria, an initial debond between the adhesive layer and adherend is assumed. Once the parameters in the vicinity of initial debond satisfy the LEFM based criteria, the initial debond is expected to grow and break the joint. Energy based debond criteria include peel strain energy density, shear strain energy density, and strain energy density [53]. Further, normal force at the tip of the debond (mode I fracture), and shear force at the tip of the debond (mode II fracture) are also used. Depending on the particular adhesive and adherend, the structural failure predominantly governed by one or a combination of failure criteria. The reader is encouraged to select the appropriate failure criteria depend on the constituent materials.

As shown above, 20% increase of adhesive elastic modulus raises the maximum stresses by about 9%. Therefore, for SLJs of which the failure is governed by the critical stress failure criteria, the load bearing capacity is reduced by about 9%. Hence, factor of safety is reduced by 9%. On the other hand, reduction of adhesive elastic modulus decreases the maximum stresses. However, the lower elastic modulus (compared to the design value) indicates adhesive degradation or a process issue such as under curing [55] [56]. Several researches have shown that reduction of adhesive elastic modulus indicates the reduction of bond strength, hence premature structural failures [55] [57].

In order to study the influence of the cohesive damages (variation of elastic modulus) on the LEFM based facture criteria parameters, an FE analysis is conducted. The FE model parameters are identical to the FE model described above. However, an initial debond is created at the adhesive-adherend interface. The initial debond is located at the free surface of the adhesive layer, where the stress values are at the highest. The initial debond length is 5mm. Further, a fine mesh is used for an accurate variation of the parameters in the vicinity of the debond tip. The resulting deformed configuration is shown in Figure 4.5 (a) and (b). The FE analysis is repeated by varying the adhesive elastic modulus.

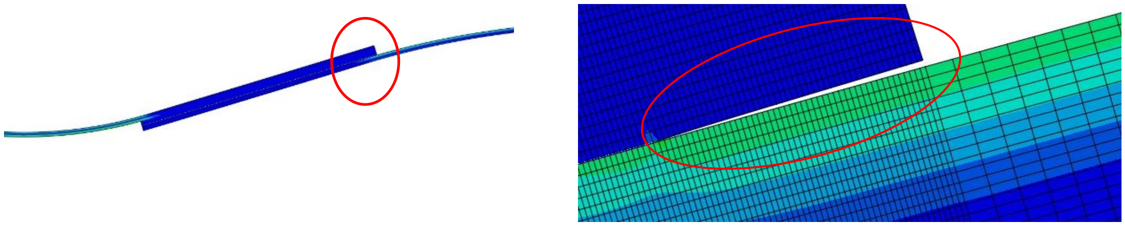
(a) (b)

Figure 4.5 (a) Deformed SLJ configuration, (b) debond opening

The resulting peel strain energy density, shear strain energy density, and the total strain energy density variation are shown in Figure 4.6 (a) and (b). Similarly, the variations of debond tip forces are given in Figure 4.7. Note that the debond tip opening forces are given in the value corresponding to 0.245mm. All the energy densities do not show a notable variation with respect to the adhesive elastic modulus variation. For the adhesive materials of which the failures are profoundly governed by the energy-based criteria, the failure is not influenced by cohesive damages. On the other hand, 20% of elastic modulus variation changed the debond tip driving forces by over 10%. Therefore, the failure loads of the SLJs that determined with the debond driving forces (which are analogue to peel and shear stresses), decreased by cohesive damage.

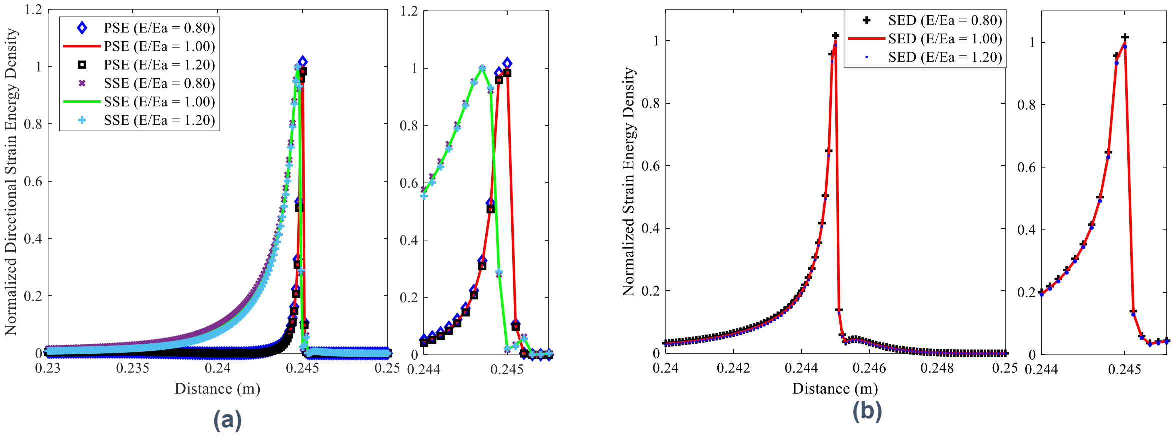

Figure 4.6 (a) peel strain energy density, (b) shear strain energy density

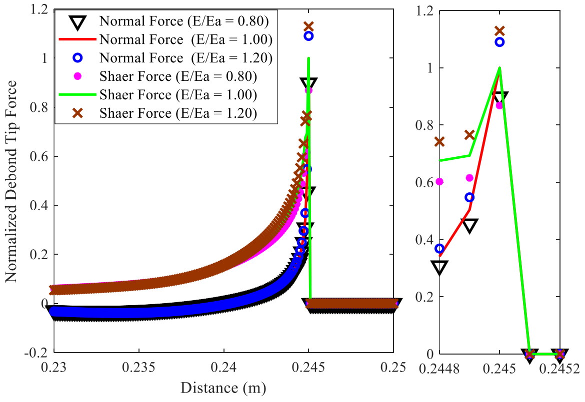

Figure 4.7 Debond tip forces

4.5 Lamb wave propagation along an SLJ

The Lamb wave propagation along an SLJ consists of aluminum adherands, is experimentally investigated. The SLJ configuration and the experimental set up are shown in Figure 4.8 and Figure 4.9, respectively. A piezoelectric actuator is utilized for the wave excitation. The excitation signal is generated by Agilent 33220A function/arbitrary waveform generator (5Vpp). A 3.5 cycle tone burst is selected due to its short cycle time. A laser Doppler vibrometer records the resulting wave motion. The high frequency environmental interferences are filtered with a low-pass signal filter. The aluminum adherends are 1.27mm (0.05 in) thick. Hysol EA 9309.3NA epoxy paste adhesive is used and the cured thickness is 0.1 mm.

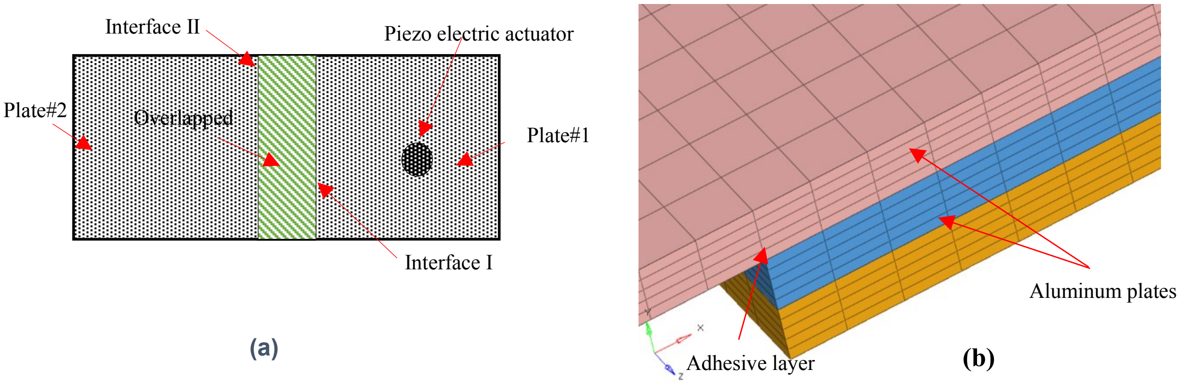

Figure 4.8 (a) SLJ configuration, (b) adhesive later and adrerands

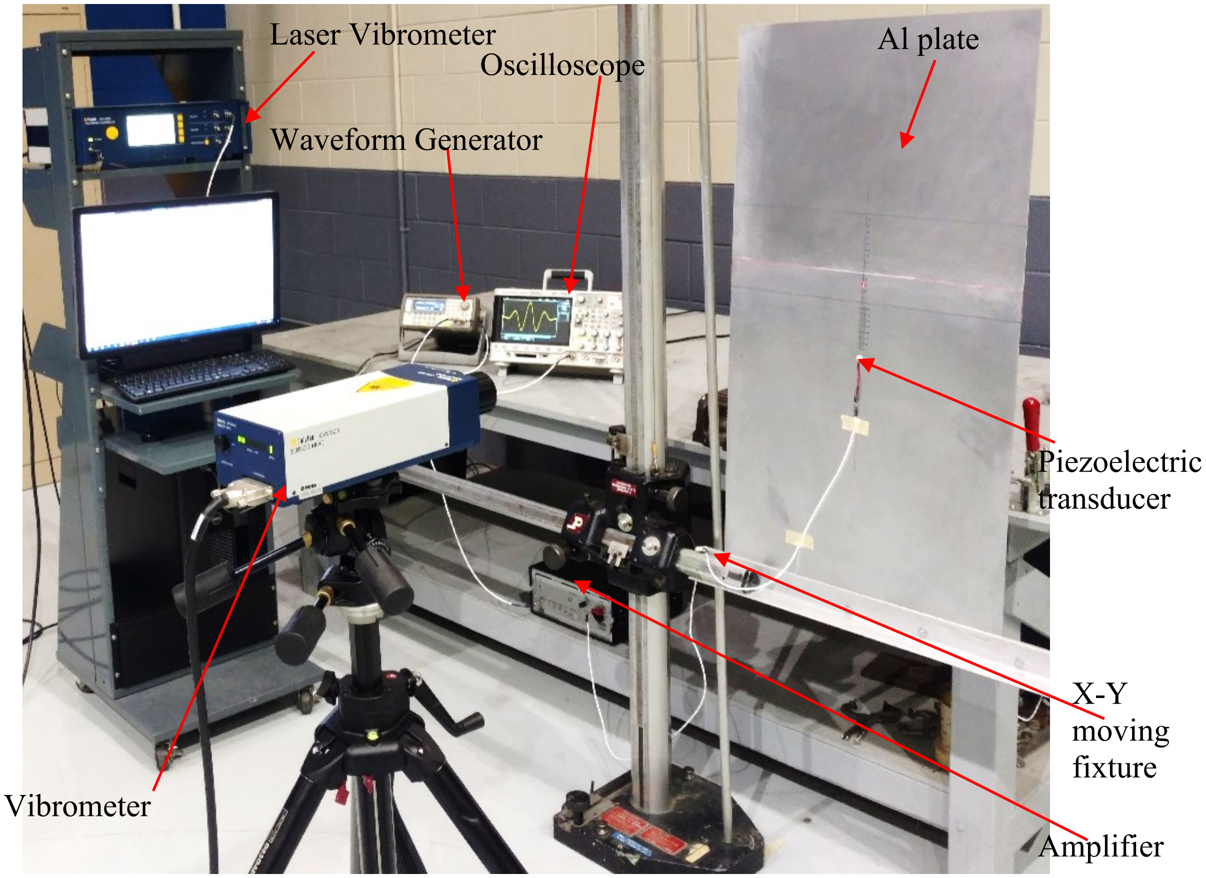

Figure 4.9 Experimental set up

Figure 4.10 shows a generic waveform captured in between the actuator and interface ***I*** (Figure 4.8). The wave signal consists of three main wave packets. The first wave packet corresponds to the forward moving wave. The second wave packet corresponds to the reflection from the interface ***I***. The third wave packet is the reflection from the interface ***II***. In addition to the reflections at the interfaces, the forward moving wave packets are mode-converted due to the asymmetry of the interfaces. The mode converted wave packets are clearly visible on the signals recorded on the adhesive joint (or past the adhesive joint). Figure 4.11 shows the waveform captured once the forward moving wave passed the adhesive joint. Since this waveform is captured after the adhesive joint, the wave shape and the amplitude are determined by adhesive properties. Therefore, in this work we use the wave motion, which is captured at interface *II*, for the estimation of adhesive properties.

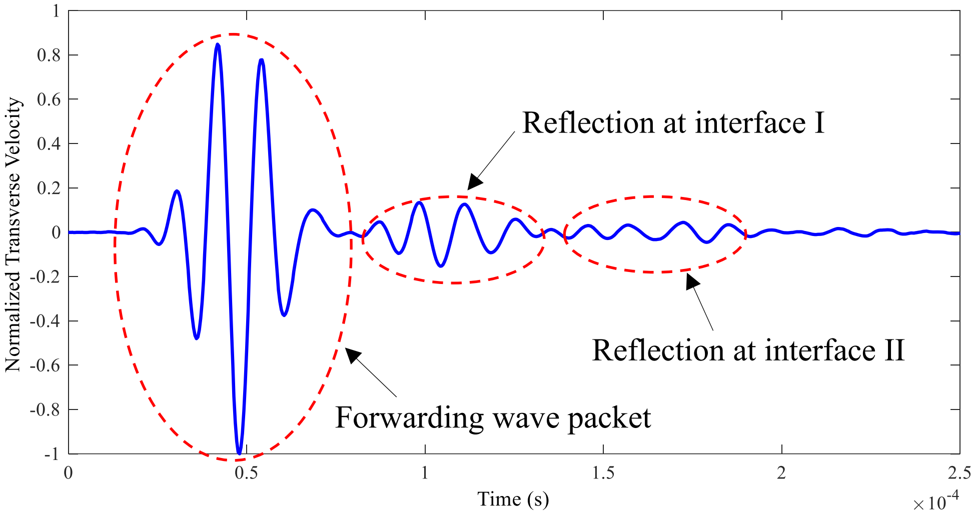

Figure 4.10 A general wave motion between the actuator and interface I

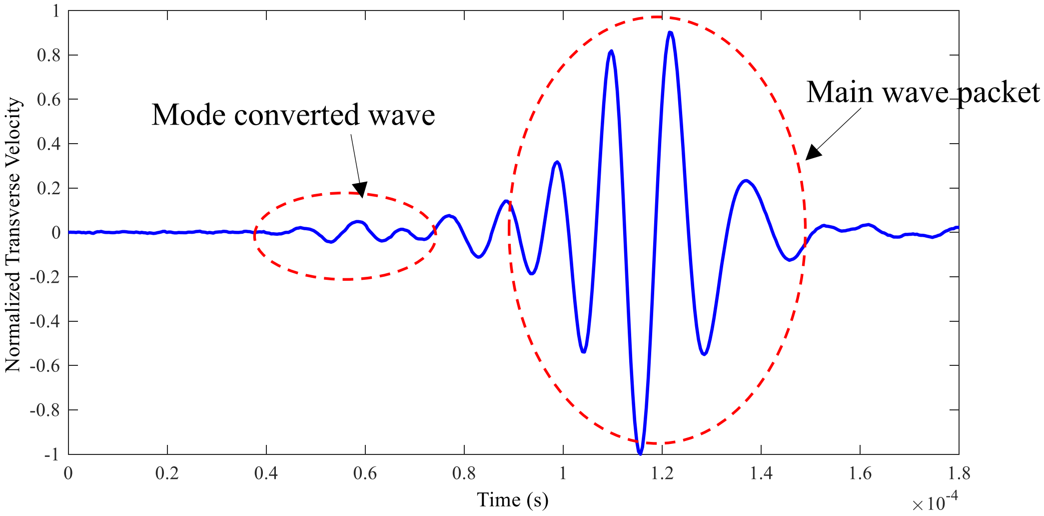

Figure 4.11 Wave motion captured at plate #2

The Lamb wave propagating along the SLJ is analyzed in spectral domain using an FE model. The FE model (Figure 4.8 b) is identical to the experimental setup. The FE analysis is performed by varying the elastic modulus and the adhesive thickness.

4.5.2 Effect of the adhesive elastic modulus

First, the dispersion curve of the Lamb wave on the SLJ is compared with that of the the Lamb waves on the bare adherend (aluminum plate). The time history of in-plane and out-of-plane velocities are recorded for at 128 equidistance points. Then the captured data are transformed into the spectral domain using 2D FFT. Figure 4.12 (a) shows the 2D FFT of the recorded time-space history data. The continuous red line shows the theoretical dispersion curve of A_0 and S_0 of the aluminum plate, and the dash red lines show the trend lines of the A_0 and S_0 wave modes on the SLJ. It is clear that within the given rage on the frequency and wavenumber, only A_0 wave mode is clearly visible on the plot and the other wave modes are barely visible. For the given frequency range (0-500kHz) the velocity of the S_0 wave mode is significantly higher than that of the A_0 mode and therefore at this range, S_0 mode has a larger wavelength and a smaller wavenumber. Additionally, the amplitude of the transverse velocity of the symmetric modes are considerably lower than that of the antisymmetric waves and as result, the symmetric modes are not clearly visible in generated dispersion curves.

In order to determine the effects of the elastic modulus of the adhesive layer on the dispersion characteristics of the Lamb waves, the elastic modulus of the adhesive layer isvaried by several percentages and the wave propagation is simulated. Figure 4.12(b) shows the dispersion curve obtained for several SLJs with different elastic moduli. It is clear that, for a given frequency, the velocity of the A_0 mode increases as elastic modulus of the adhesive layer increases, and these results align with ref [41]. Within this excitation frequency range, the A_0

amplitude is dominating and therefore, the amplitudes of other the wave modes are not clearly shown. Amplitudes of the A_0 and S_0 wave modes are known to increase because of the influence of the adhesive layer [46], and therefore, for the purpose of increasing the relative amplitude of the higher order wave modes with respect to the A_1 mode, the elastic modulus of the adhesive layer is brought down until the other wave modes become visible. The resulting lap joint configuration is set as the baseline. Reduction of adhesive elastic modulus decreased the cut off frequency of the higher order modes and raised the relative amplitude of the higher order modes.

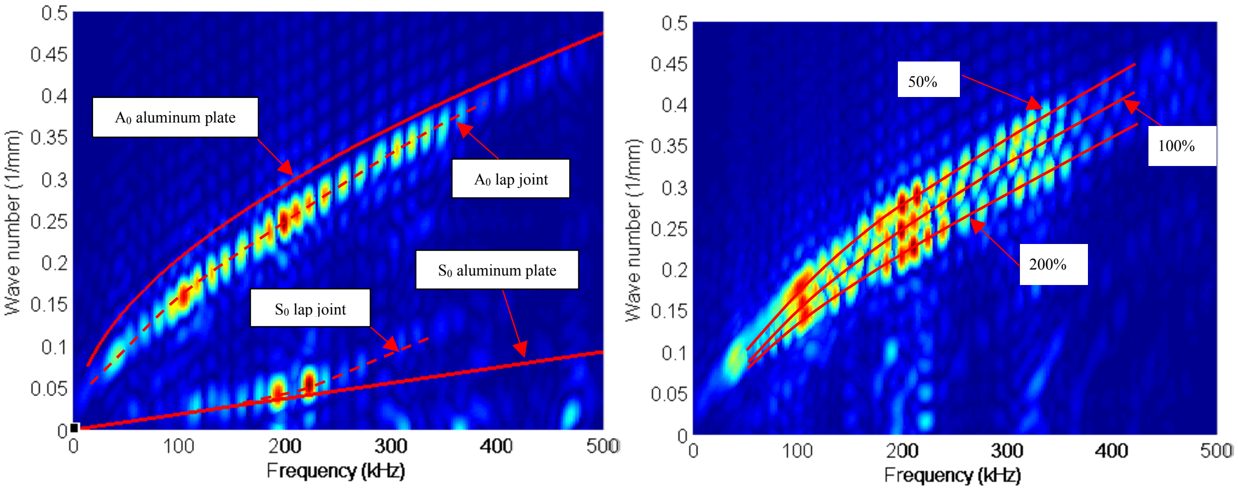

(a) **(b)**

Figure 4.12 (a) Comparison of dispersion curve of the lap joint to that of an adherend (b) variation of dispersion curve of A_0 wave mode as adhesive elastic modulus varies

Once the base line is established, the adhesive elastic modulus is varied and the wave propagation simulations on the corresponding SLJs are repeated. The resulting dispersion curves obtained for different adhesive elastic moduli are plotted on the same graph for the purpose of comparison. As shown in Figure 4.13, once the adhesive layer elastic modulus become lower compared to the adherend (aluminum plate) elastic modulus, the influence of the adhesive layer on A_0 become insignificant and the dispersion curve of the A_0 mode tends to be independent of the adhesive elastic modulus. On the other hand, the amplitude of A_1 wave mode becomes comparable with that of the A_0 and the dispersion curve of A_1 mode is observed to be significantly varying as the elastic modulus of the adhesive layer changes. Figure 4.13 presents the dispersion curves generated for SLJ with different adhesive elastic moduli. In Figure 4.13, the red dash line represents the trend line of the A_0 modes and the continuous red lines show the trend lines of A_1 wave modes generated under different adhesive elastic moduli.

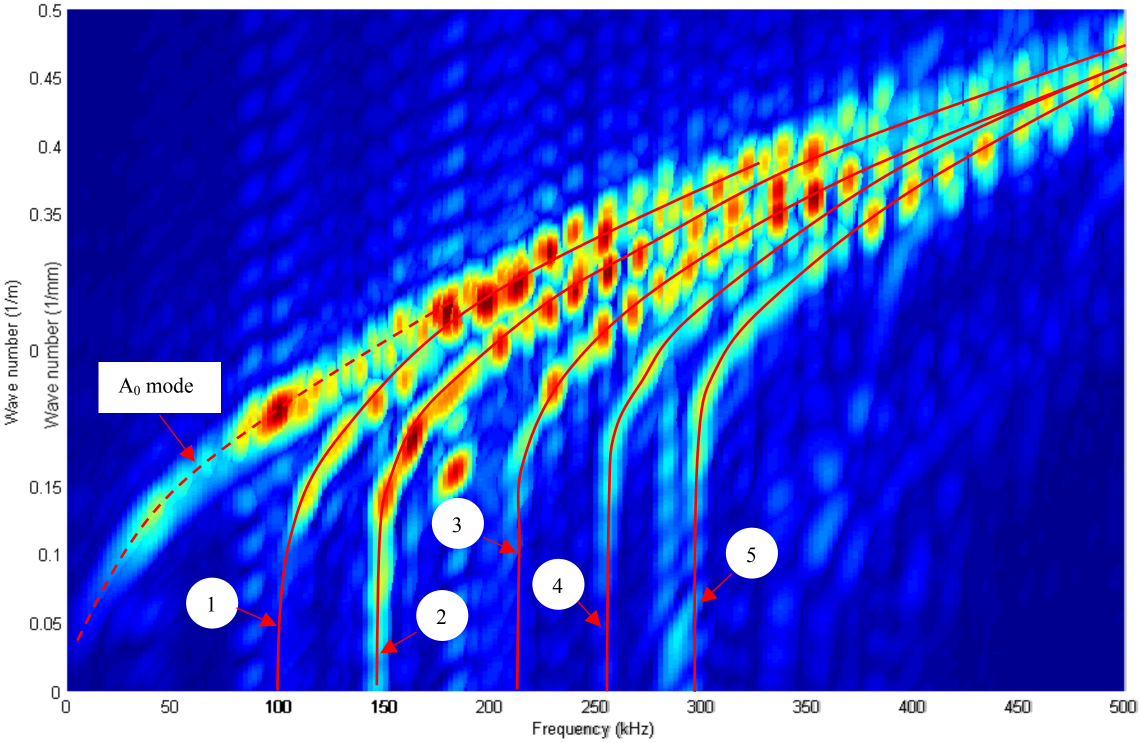

Figure 4.13 Dispersion curves generated under different adhesive elastic modulus. Legend: (1) elastic modulus is 20% of the baseline elastic modulus, (2) elastic modulus is 50% of the baseline elastic modulus, (3) elastic modulus is 100% of the baseline elastic modulus, (4) elastic modulus is 150% of the baseline elastic modulus, (5) elastic modulus is 200% of the baseline elastic modulus

The cut off frequency which is considered as the intersection point of the dispersion curve and frequency axis, is one of the obvious measurements that can readily be quantified from the dispersion curves. At frequencies below the cutoff frequency the mode is no longer propagating and thus presence or absence of the mode near cutoff frequency may indicate certain level of stiffness of the adhesive layer. As shown in Figure 4.13**,** the cut off frequency of the A_1 significantly varies as value of the adhesive elastic modulus change. The maximum error of the cut off frequency estimation is approximately about 10 kHz which is corresponding to 5% of maximum error for the inverse problem of estimating the adhesive elastic modulus from the cut off frequency. Figure 4.14 shows the cut of frequency variation of A_1 wave mode with respect to the adhesive elastic modulus.

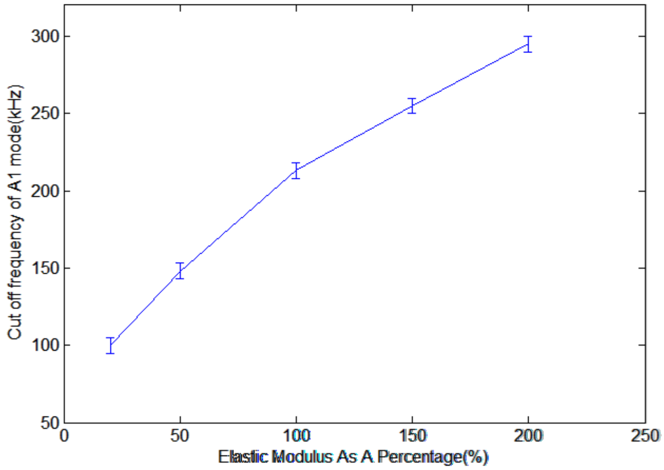

Figure 4.14 Cut of frequency variation of A_1 wave mode with respect to the value of the adhesive elastic modulus of the lap joint

As mentioned above, the change of the adhesive layer elastic modulus can be correlated to a number of adhesive layer defects. Most of the adhesive materials require to be undergone some type of a curing process and depending on the adhesive type, the adhesive layer may be cured in elevated temperature or in room temperature. The curing process hardens the adhesive layer and consequently raise the elastic modulus. If the curing process is not completed successfully, the adhesive layer may become soft and less stiff. Since the cut off frequency of the A_1 wave mode on the lap joint is directly related to the elastic modulus of the adhesive layer, the cut off frequency can be used as a measurement to determine the level of cure of the adhesive layer. Micro porosity is another factor which degrades the effective stiffness of the adhesive layer. Thus, the reduction of elastic modulus directly indicates the presence of the defects on the adhesive layer, which can also be determined from the cut off frequency of the A_1 wave mode.

4.5.3 Effects of adhesive layer thickness

The thickness of the adhesive layer is varied, and the cut off frequencies of A_0 and A_1 wave mode are examined. According to the results, the cut of frequency of A_0 wave mode is independent from the adhesive thickness and the cut off frequency of the A_1 wave mode is observed to be less sensitive to the thickness variation of the adhesive layer as shown in Figure 4.15.

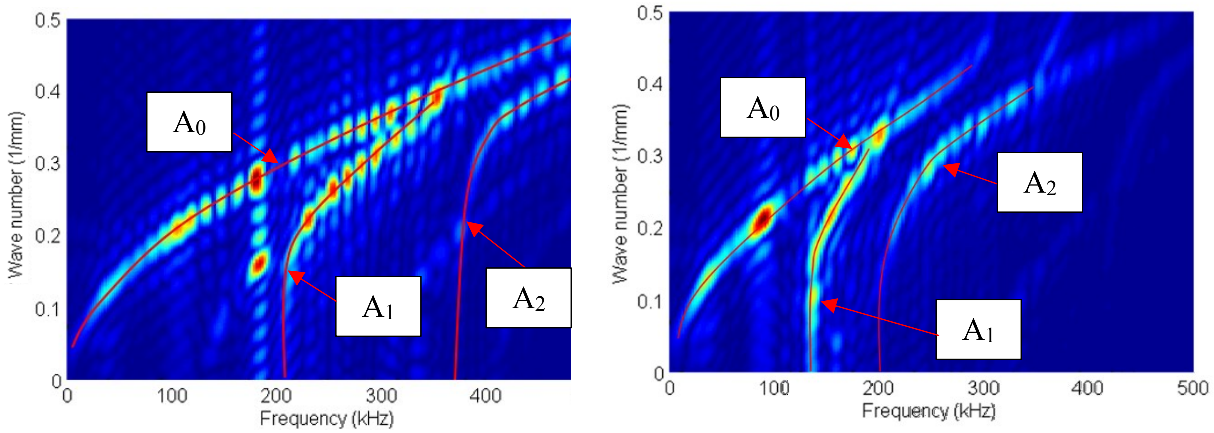

(a) **(b)**

Figure 4.15 (a) Dispersion curves of the baseline model (b) dispersion curve generated for the model of which the adhesive thickness is 200% of the baseline case

Figure 4.16 (a) shows the cut off frequency variation of A_1 mode with respect to the adhesive thickness. According to Figure 4.16 (a), the cut off frequency of the A_1 wave mode decreases as the thickness increases and the relative sensitivity is considerably low. The frequency estimation error is approximately 10 kHz which corresponding to 10% of adhesive thickness estimation error for the inverse problem in which the adhesive thickness is calculated from cut off frequency. Figure 4.16 (b) shows the cut off frequency variation of A_2 mode with respect to the adhesive thickness, and according to the figure, A_2 mode exhibits a significant sensitivity to the adhesive layer thickness. Since the amplitude of the A_2 mode is very weak near its cut off frequency level, the exact cut off frequencies are difficult to be determined and therefore the projected value obtained from the trend line is plotted.

The strength of a bonded joint strongly correlate with the adhesive layer thickness, and both failure stress and the elongation at the failure decrease as the bond thickness increases, for all type of loading configurations [58]. Therefore, maintaining the design bond thickness during the manufacturing process as well as during the operation of the structure is crucial. Once the cut off frequency of the baseline case (lap joint with designed adhesive thickness) is known, the bondline thickness can readily be estimated using the cut off frequency change.

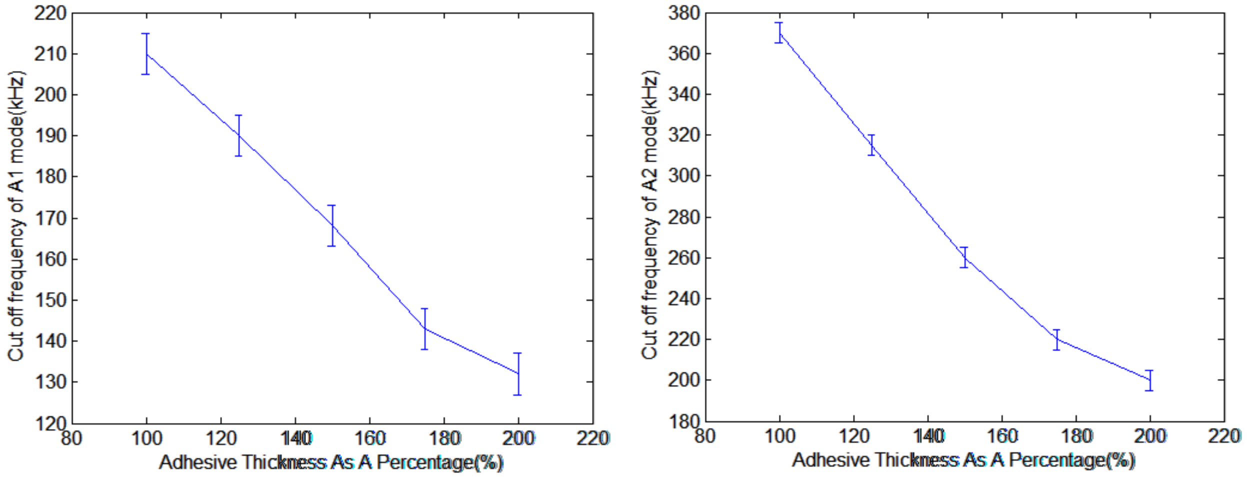

(a) **(b)**

Figure 4.16 (a) cut of frequency variation of A_1 wave mode with respect adhesive thickness (b) cut of frequency variation of A2 wave mode with respect adhesive thickness

4.5.4 Effects of the adhesive density

The cohesive density of the adhesive layer directly correlates to the micro porosity presence in the bond area and is able to significantly reduce the load carrying capacity of the joint. Density of the adhesive layer is varied by several percentages and the dispersion curves for each density value is generated using 2D FFT. Both A_0 and A_1 waves are not (or negligible amount) sensitive to the adhesive density.

4.6 The normal and the shear stiffness of the adhesive layer

The normal (***kt***) and shear (***ks***) stiffness of the entire adhesive layer is a function of adhesive modulus, Poisson's ratio, adhesive layer thickness and width (***E***, ***υ***, ***t***, and ***b*****)** as seen in Eq. 4.1 and Eq.4.2. Hence it is clear from these two relationships that both the stiffness are functions of ***E/t*** ratio. Therefore, as long as ***E/t*** ratio is constant, the wave characteristics remain identical. However, if the mass of the adhesive layer is significant compared to that the adherends, the inertial effects of the adhesive layer influence the wave motion.

$$k_t = b\left(\frac{E}{t}\right) \tag{4.1}$$

$$k_s = \frac{Gb}{t} = 2b(1+\upsilon)\left(\frac{E}{t}\right) \tag{4.2}$$

4.7 Inverse problem approach

The adhesive layer elastic modulus variation (cohesive defects), initial debonds, and micro voids considerably change the factor of safety of the SLJ. The adhesive elastic modulus may deviate from its design value due to erroneous processes and process parameters. Further, the elastic modulus may change due to the moisture absorption or other environmental effects. Later, we show that micro voids, debonds, and weak bonds contribute to the reduction of the effective stiffness of the SLJ. Conversely, aforementioned damages can also be quantified from the current elastic modulus of the adhesive layer. The properties of the adhesive layer, which is not measurable prior to the fabrication, is profoundly governed by the manufacturing process/parameters. Therefore, a quantitative estimation of adhesive layer properties of the finished product is critically important for assurance of the product conformity against the design parameters. Additionally, the prolonged exposure to the high humidity and temperature, further changes the adhesive properties [27]. Thus, a continuous/periodic monitoring of the adhesive layer properties is also crucial for continued safe operation of adhesively bonded structures. In current work, we use an inverse problem approach based numerical technique for the estimation of the current elastic modulus. The damage severity is then calculated from the current elastic modulus. 0 presents the flow diagram of the proposed inverse problem.

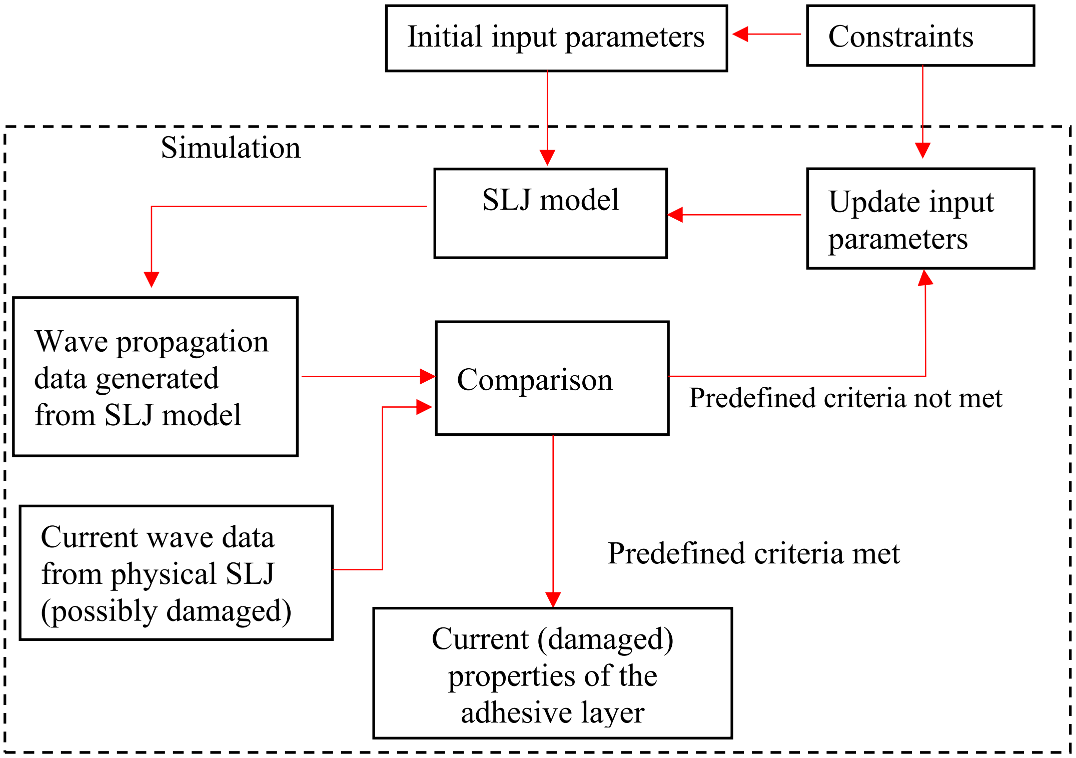

Figure 4.17 Flow diagram of the proposed inverse problem

A Lamb wave is excited on the physical SLJ (possibly damaged), and the resulting wave response (current wave data) is captured. The Lamb waves that propagate past the overlapped region, is influenced by the adhesive properties and the thickness. Hence, the wave is recorded once it completely travels through the overlapped region. An analytical/ numerical model which is identical to the physical SLJ, is utilized to generate the wave data for the comparison with current wave data. The generated wave data is then compared with the current wave data obtained from the physical SLJ. This process is repeated by varying the adhesive layer properties until a good agreement between the physically recorded wave data and model generated wave data, is obtained. However, an analytical solution for this complex wave propagation is very difficult to obtain [36]. On the other hand, conventional FE models accurately simulate the wave propagation along SLJs. However, the conventional FE models are computationally very expensive. Since the proposed technique require repeated simulation in each iteration, overall, the technique become significantly time consuming. As solution, the authors developed a Wavelet Spectral Finite Element (WSFE) SLJ model which is computationally very efficient compared to the conventional FE models. A brief description of the WSFE model is given in following section.

4.8 Description and the validation of WSFE LSJ model

The adherends are modeled as homogenous isotropic/anisotropic material and the adhesive layer is modeled with homogenous isotropic material. The continuously distributed tension/compression and shear springs are used to model the adhesive layer. The Hamilton's principle is used to derive the governing wave equation in Partial Differential Equation (PDE) form, and PDEs are then reduced to Ordinary Deferential Equation (ODE) using Daubechies scaling function. The resulting ODEs are solved exactly by applying a harmonic solution. The wave motion generated from a conventional FE model is employed to validate the WSFE model [36]. A load (impulse) is applied in transverse direction, and the resulting transverse and longitudinal (axial) responses are shown in Figure 4.18. It is clear that, WSFE SLJ generated wave motion very closely resemble the FE generated wave motion. The complete validation of the WSFE LSJ model is given in ref [36].

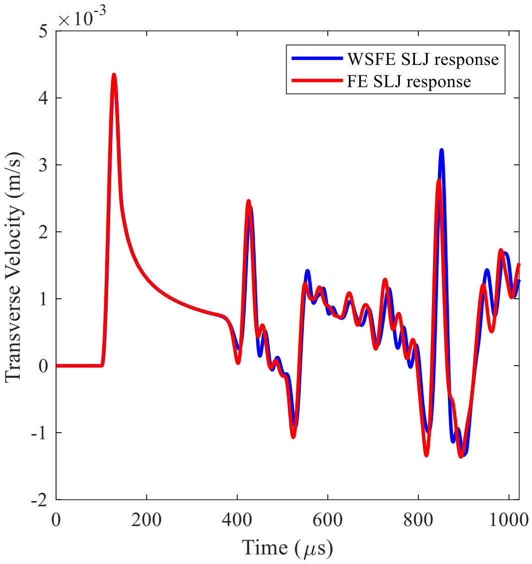

Figure 4.18 Comparison of WSFE generated wave motion with FE generated wave data

4.9 Experimental validation

4.10 Experimental setup

The experimental setup, shown in Figure 4.9, comprises two adhesively bonded aluminum plates (520x480 mm) with a surface bonded disc type PTZ transduce. The plates are made from 6000 series aluminum and the thickness of each plate is 1.27mm (0.05 inch). The plate size is selected (using dispersion curves shown in Figure 4.19) to prevent the side reflections during the data acquisition period to avoid the complexities generated from side reflections. Hysol EA 9309.3NA epoxy paste adhesive is used to bond the plates together and standard pre-preparation, bonding, and curing procedures specified by manufacturer, are followed in the bonding process. The cured thickness of the adhesive layer is measured to be 0.1 mm. A disc type PTZ made from SM412 is permanently bonded on one plate Figure 4.9. The transducer has the dimensions of 12mm diameter and 0.5mm thickness. The excitation signal is generated by Agilent 33220A function/arbitrary waveform generator (5Vpp) and consequently amplified by A.A Lab Systems' A303 high voltage amplifier and modulator (up to 100Vpp). A LDV (Polytec OFV – 5000 with OFV – 500 laser head) is used to acquire the wave motion. The sampling frequency for the LDV data acquisition is set to 2560 kHz, and a low-pass frequency filter (200 kHz) is employed to reduce the noise level. For each sensing location, the signals are recorded fifty times and then averaged.

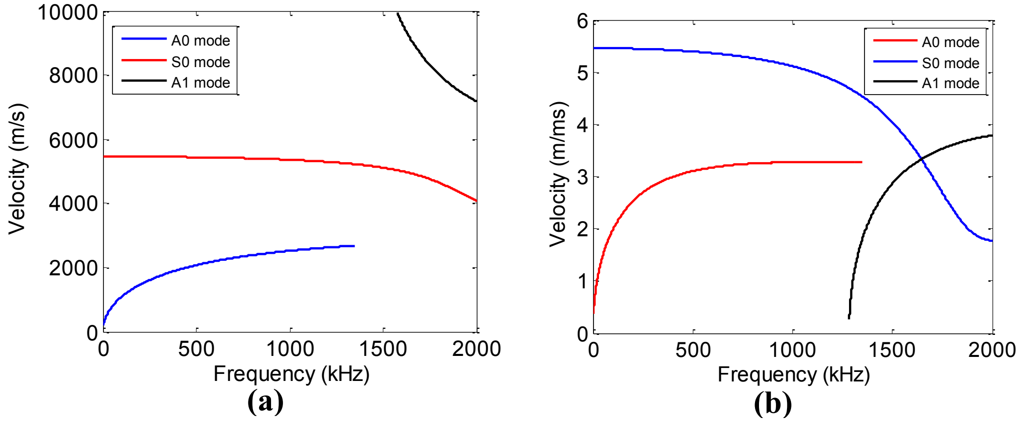

Figure 4.19 Dispersion curve for aluminum plate (a) group velocity (b) phase velocity

4.11 Bonded lap joint configuration and excitation

A 3.5 cycle 80 kHz tone burst is selected as the excitation waveform due to its short time-length with respect to the wave speed over the excitation frequency range. This facilitates to locate separate wave packets (away from each other on time axis). Highest practical excitation frequency range of piezoelectric transducer is also selected by structural mode-tuning, [59, 32] in order to further shorten the cycle time. The experimental and the WSEF wave propagation data are normalized before the comparison, and the experimental wave propagation data is slightly (~1μs) moved along the time axis on order to obtain a batter agreement

4.12 Correlation of experimental data with WSFE result

Generally, the signal profile (voltage) which is used in the experimental wave excitation is also used as the input profile (excitation force) in numerical simulations. The surface bonded piezoelectric transducers generate in-plane and out-of-plane excitation forces. These forces may have phase difference. A finite element (Abaqus) simulation is therefore performed to determine the excitation force profiles. A cantilevered aluminum plate with a bonded piezoelectric transducer is modeled (SM412 [34]). The plate size is kept sufficiently larger in order to delay the arrival of boundary reflections. The tone burst signal which is used in experiments (3.5 cycle, 80 kHz) is given as the input for simulations (Abaqus standard dynamic solver). The reaction forces generated between the piezoelectric transducer and the plate are recorded. Figure 4.20 shows that the in-plane forces are in-phase with excitation voltage signal. Further, the out-of-plane force is anti-phase with the excitation voltage signal. These force profiles are used as the input force for WSFE analysis.

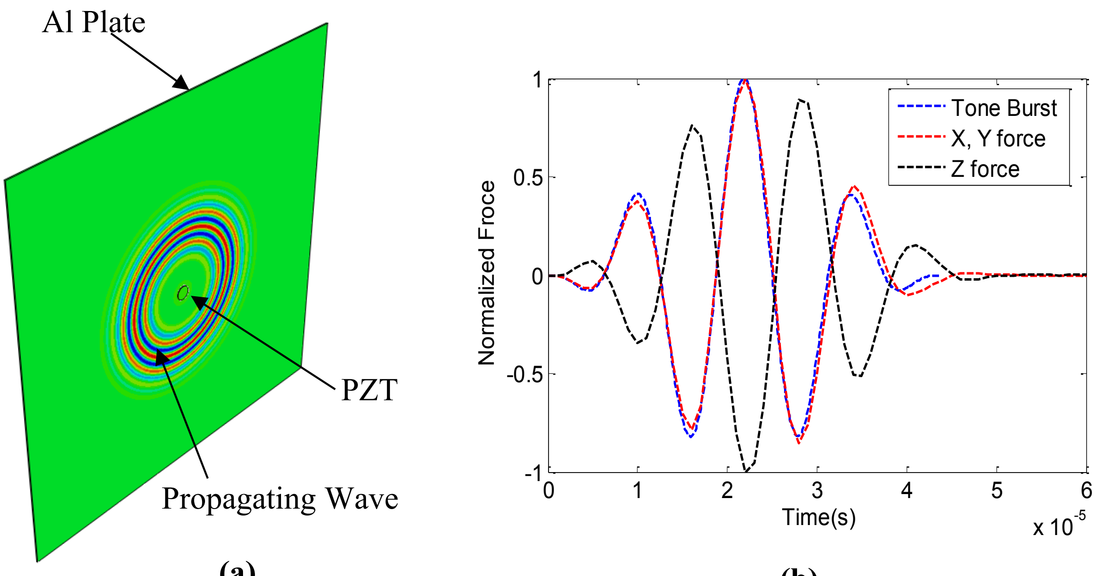

(a) (b)

Figure 4.20 (a) FEA simulation results (b) force profile

4.13 Input excitation for WSFE simulations

The use of appropriate input excitation in numerical (WSFE) simulations is crucial in experimental validation. Figure 4.21 shows experimental and WSFE results for two inputs, namely (a) the tone burst input force (b) the input force profiles determined from FEA. It is observed that there are significant differences in wave amplitude for input (a), whereas WSFE and experimental results are in very good agreement for input (b).

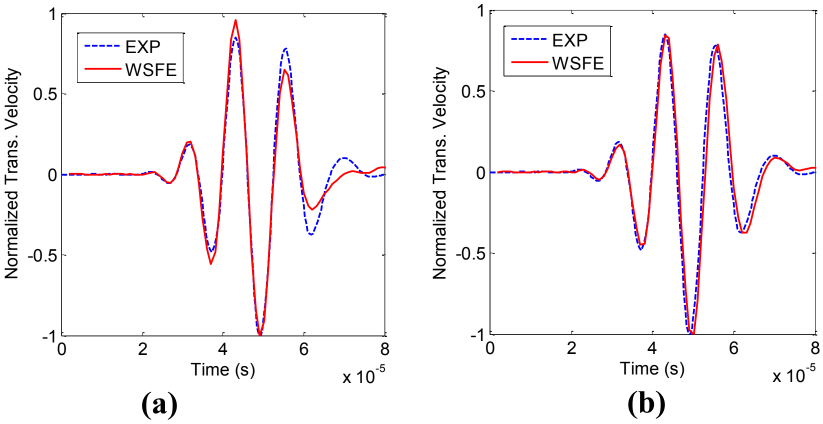

Figure 4.21 Experimental and WSFE result (a) tone burst input force (b) FEA calculated force used as input for WSFE simulations measured 40 mm from piezoelectric transducer

4.14 Comparison of experiment and WSFE results

Figure 4.22 presents the comparison of experimental and WSFE wave propagation data on Plate #2, 50 mm from the actuator location. It is observed that the experimentally measured forward propagating wave packet shows a very good agreement with the WSFE model generated wave propagation data. The first reflected packets have the same frequency, but the experimental wave has a smaller amplitude compared to WSFE model generated wave data. This is caused by the wave attenuation due to the material damping of the aluminum plate, whereas the WSFE model does not account for the material damping. Larger variations between WSFE wave data and the experimental wave data can be observed for the subsequent wave packets due to differences in the boundary conditions (in addition to the lack of damping in WSFE model).

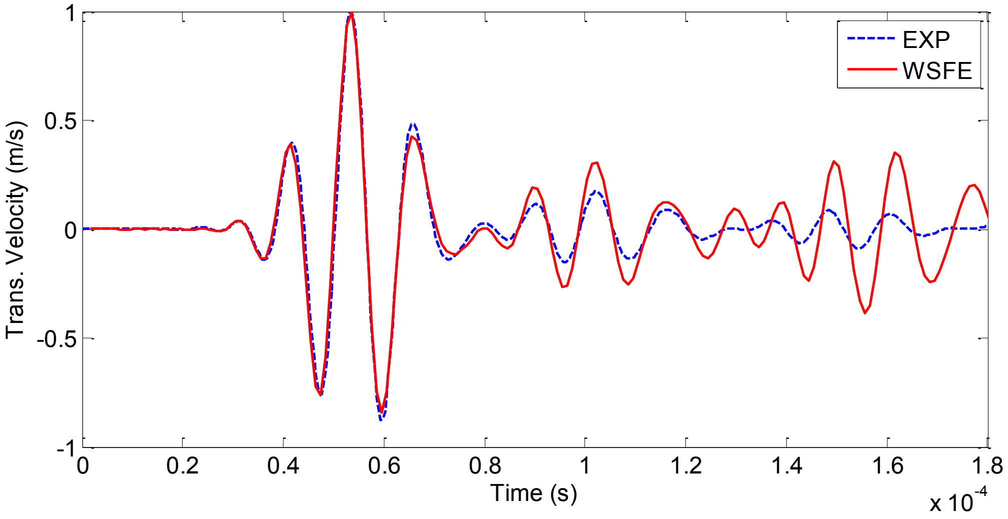

Figure 4.22 Figure 1: Response on Plate # 2, 50 mm from piezoelectric transducer at 80 kHz

Figure 4.22 shows the experimental wave data and WSFE model generated wave data for the sensing point located on the bonded region (20 mm from Interface II). The forward propagating wave (the largest) packet of the WSFE wave data shows a very good with experimental wave data. The mode converted wave packet shows a slight difference in phase and amplitude. The noticeable difference between the WSFE and the experimental wave data in later wave packets is due to the lack of damping in the WSFE modeling, as the experimental waves attenuate significantly after passing through the lap joint.

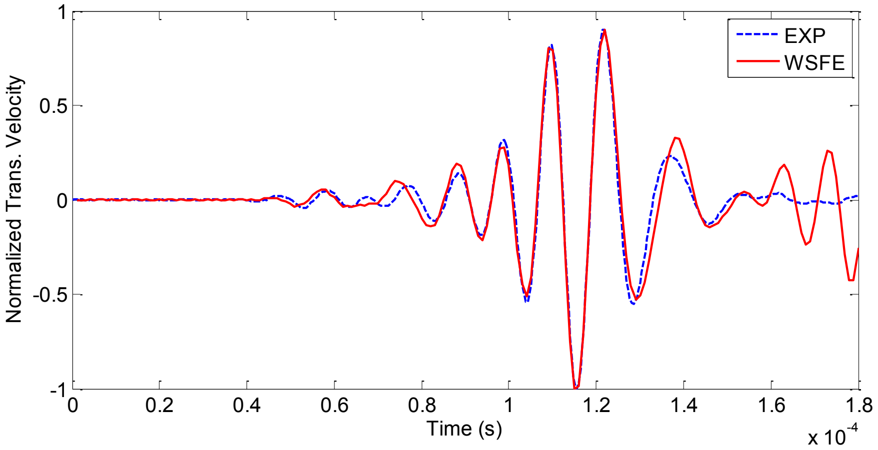

Figure 4.23 Response on the bonded area, 20 mm from interface II at 80 kHz

4.15 Objective function

The object of the inverse problem approach is to modify the WSFE SLJ model so that it produces a wave response which is identical to that of the physical SLJ. Since this is an optimization/minimization problem, an optimization algorithm is used for the iterative process. Many researches have been reported in literature, which uses optimization algorithm along with conventional FE models to reach the inverse problem approach, and all of these methods compare wave data in spectral domain. Further, due to the global nature of the objective functions, a generic optimization algorithm (or similar global optimization algorithms) is used for this purpose. In present work, we use WSFE models along with local optimization algorithms to determine the inverse problem solution, for the first time. As mentioned above, the WSFE model possess a significant computation efficiency compared to the conventional FE models. Since, the SLJ model is simulated in each iterative step, the computational advantage produced by WSFE models in each iteration, accrues. Therefore, a significant increase of the computational efficiency can be achieved (a quantitative analysis is given in a later section). Since we compare the wave data in time domain along with design constraints, the optimization problem is treated as a local optimization problem. Therefore, we will use gradient based local optimization algorithms which is computationally very efficient compared to that of the global optimization algorithms.

Initially, the objective function for the minimization problem is calculated as the absolute difference between two waveforms (*Eq. 4.3*). Both signals are recorded with the same sampling frequency. The objective function with respect to the adhesive layer elastic modulus variation is shown in Figure 4.24 (a).The term $\boldsymbol{V_{PHY}}$ is the transverse velocity recorded from the physical structure, and $\mathbf{V_{WSFE}}$ is the numerically generated transverse velocity of the wave motion.

$$\boldsymbol{f}(\mathrm{V}_{PHY}, \mathrm{V}_{WSFE}) = \sum_{\boldsymbol{i}}^{\boldsymbol{n}} \left| \mathrm{V}_{PHY_i} - \mathrm{V}_{WSFE_i} \right| \tag{4.3}$$

Regardless of its simplicity, the objective function has a unique global minimum (at ***E/Ed*** =1). It is observed that the objective function has a number of local minima. Therefore, the gradient based local optimization algorithms may not be able to determine the global minimum value. Utilizing the number of random starting point may facilitate to reach the global minimum. However, having multiple optimization processes reduce the computational efficiency of this technique. On the other hand, the problem can be converted into a local minimization problem by introducing constraints. Hence, the range of the variation of ***E*** is limited by constraints. These constraints represent the estimation limitations of adhesive elastic modulus.

According to Goland and Reissne's model, the stress levels of adhesive layer are influenced by both adhesive elastic modulus and its thickness. Therefore, both the elastic modulus and the thickness are now considered, and the objective function surface, ***f (E,t)*** is generated by varying both variables. As seen in Figure 4.24 (b), a unique global minimum is not present in the objective surface. As mentioned above, SLJ produces identical wave responses for different elastic moduli and thicknesses, as long as ***E/t*** ratio remains a constant. Due to the absence of a global minimum, it is not possible to determine both elastic modulus and the thickness of the adhesive layer. Therefore, this method can only be used to determine the elastic modulus. The thickness of adhesive joint can readily be measured using standard measuring equipment.

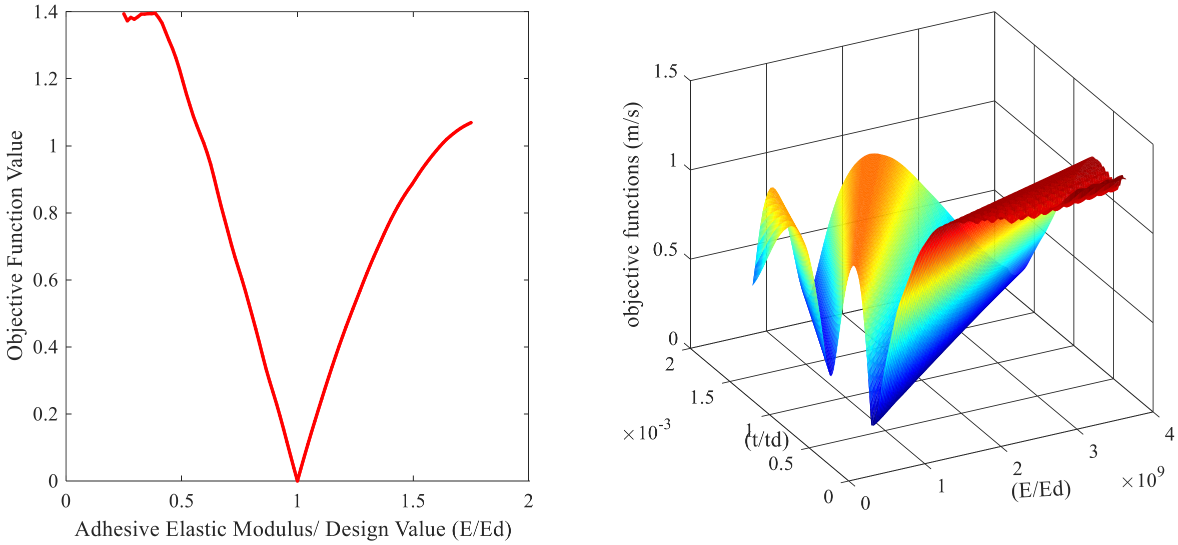

(a) *(b)*

Figure 4.24 (a) Initial objective function, (b) objective surface for multi variable problem

4.16 Modified objective function

As shown above (Figure 4.22 and Figure 4.23), slight discrepancies between the physical wave data and the WSFE model generated wave data can be observed. These discrepancies are mainly due to the group velocity differences and activation time delays of the test equipment. The environmental noises and stress relief features (e.g. fillet at the end of the bonded area) further distort the wave motion data. Therefore, a perfect agreement between the experimental data and WSFE data is practically not achievable. For this study, a conventional FE SLJ model is used to represent the physical SLJ. The adherends consist of AS4/3501–6 graphite-epoxy composites. The design adherend thickness is 0.001 m, and the width is 0.02m. The layup sequence of the laminate is taken as $[0]_{10}$. The adhesive layer consists of Hysol EA 9394 epoxy based structural adhesive with the design elastic modulus ($\boldsymbol{E_d}$) and the Poison's ratio equal to 4.24 GPA and 0.45, respectively. A WSFE SLJ model is utilized to generate the numerical wave data for comparison with the physical SLJ wave data. The two signals are compared using the objective function given in Eq. 4.3. The objective function variation against the adhesive elastic modulus is shown in Figure 4.25 (a). The objective function curve does not have a minimum at $\boldsymbol{E/E_d}$=1. This error is mainly due to the slight discrepancies between the WSFE model and the physical structure (Figure 4.25(b)).

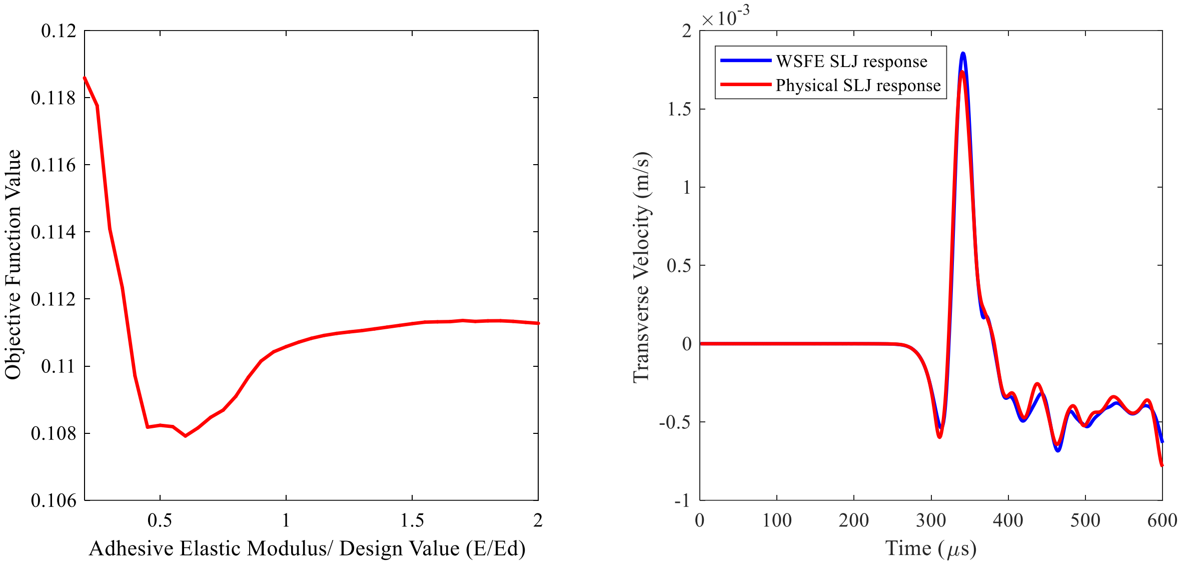

(a)

(b)

Figure 4.25 (a) Objective function with physical data, (b) slight discrepancies between the WSFE generated data and physical SLJ data

In order to circumvent this issue, a new objective function is formulated. The modified objective function, given in Eq. 4.5, is calculated using the correlation coefficient between two waveforms. The correlation coefficient is widely utilized for the signal comparison. When the two signals are identical, the correlation coefficient equals to one. Otherwise, it has a value smaller than one. Unlike simple absolute difference between the relevant data points of the two wave motions, the correlation coefficient consider the entire waveform into the consideration. The objective function variation (when ***E/E**_d*=1) is given in Figure 4.26. As shown in the figure, it has a minimum at $\boldsymbol{E/E_d}$ =1.05. Further, the optimization algorithm is performed (without generating the entire objective curve), and the optimized value was given as $\boldsymbol{E/E_d}$ = 1.05. Therefore, error of estimation equals to about 5%. The term $\boldsymbol{\sigma}$ represents the standard deviation of the data points recorded for the transverse velocity signals, and $\boldsymbol{\mu}$ represents the mean of the data points. The term $\boldsymbol{\rho}$ stands for the correlation coefficient.

$$\rho(V_{PHY}, V_{WSFE}) = \frac{1}{N-1}\sum_{i=1}^{N}\left(\frac{\overline{V_{WSFE_i} - \mu_{WSFE}}}{\sigma_{WSFE}}\right)\left(\frac{V_{PHY_i} - \mu_{PHY}}{\sigma_{PHY}}\right) \tag{4.4}$$

$$f(V_{PHY}, V_{WSFE}) = \frac{1}{\rho(V_{PHY}, V_{WSFE})} - 1 \tag{4.5}$$

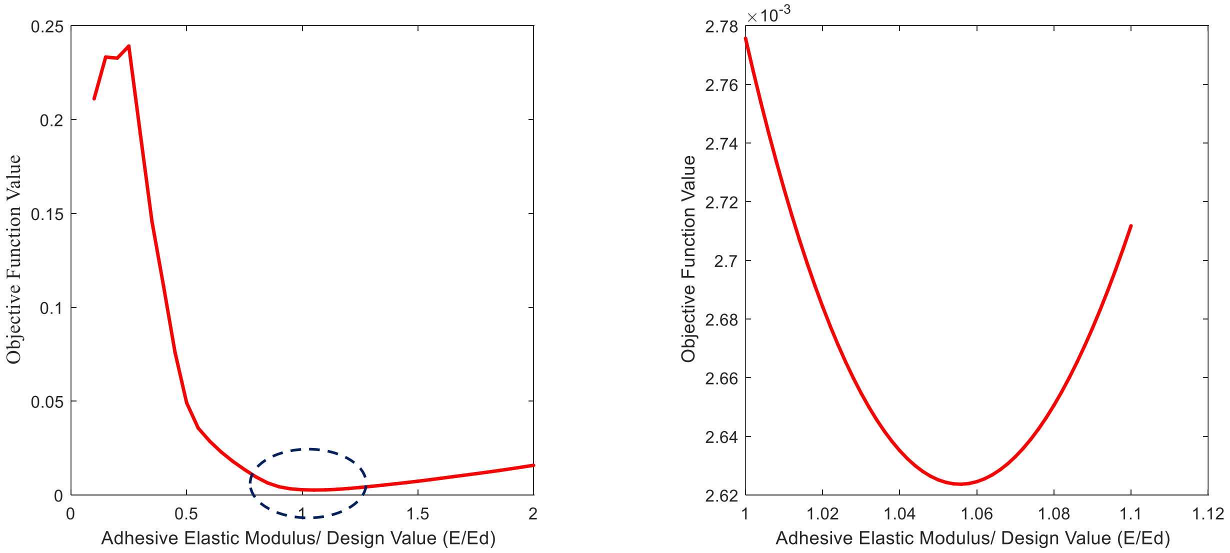

(a) **(b)**

Figure 4.26 (a) Modified objective function, (b) modified objective function near the minimum point

Further, we evaluated the robustness of this objective function. All the stress components (peel, shear, and longitudinal) have their highest values at, or near the free ends of the bonded area. Therefore, fillets and chamfers are commonly used at the free edges for stress concentration reduction. The possible influences of the edge fillets/chamfers for the inverse problem solution is investigated. The physical SLJ is modified by adding chamfers to the free ends (Figure 4.27 (a)). The objective function is then constructed ($\boldsymbol{E/E_d}$ =1). The resulting objective function, which is shown in Figure 4.27 (b), has a global minimum at $\boldsymbol{E/E_d}$ =0.99. Similarly, the inverse problem solution is calculated using the optimization algorithm. The resulting value is $\boldsymbol{E/E_d}$ = 0.98, which is very close to the design value. Therefore, regardless of the presence of the stress relief features, the inverse problem is able to estimate the elastic modulus with a considerable accuracy.

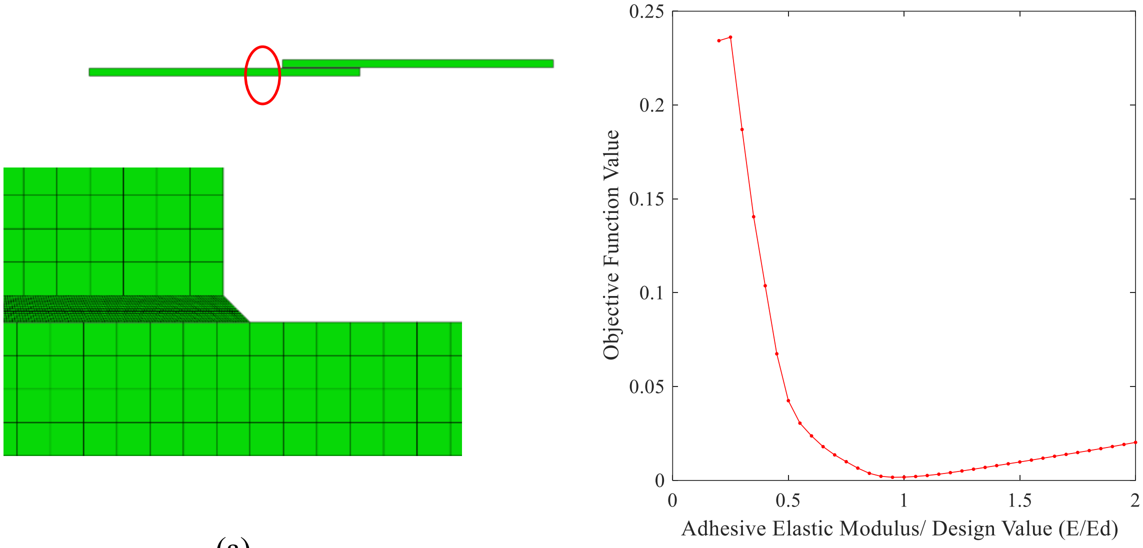

(a)

(b)

Figure 4.27 (a) The fillet at the free edge, (b) the objective function

The experimental test data consists of noises from the environment, test equipment, and data recording. In order to test the robustness of this inverse problem approach (the objective function), an artificially generated random noise is added to the physical wave motion, and the inverse solution is obtained. The original physical wave data and the noise added wave data is shown in Figure 4.28 (a). The signal to noise ratio is kept in about 5%. Since the bandwidth of the random noise is virtually infinite, a band-pass filter cannot be used in this situation. However, the random noises can be attenuated by taking the average of number measurements. However, taking number of wave measurements increase the inspection time. The objective function (when E/E_d =1) is shown in Figure 4.28 (b). The inverse problem solution is calculated without generating the entire objective function, and the resulting solution is E/E_d=0.53. This is an inaccurate solution. Additionally, since the starting point of the optimization process is selected randomly, the solution changes every time when the optimization process is conducted.

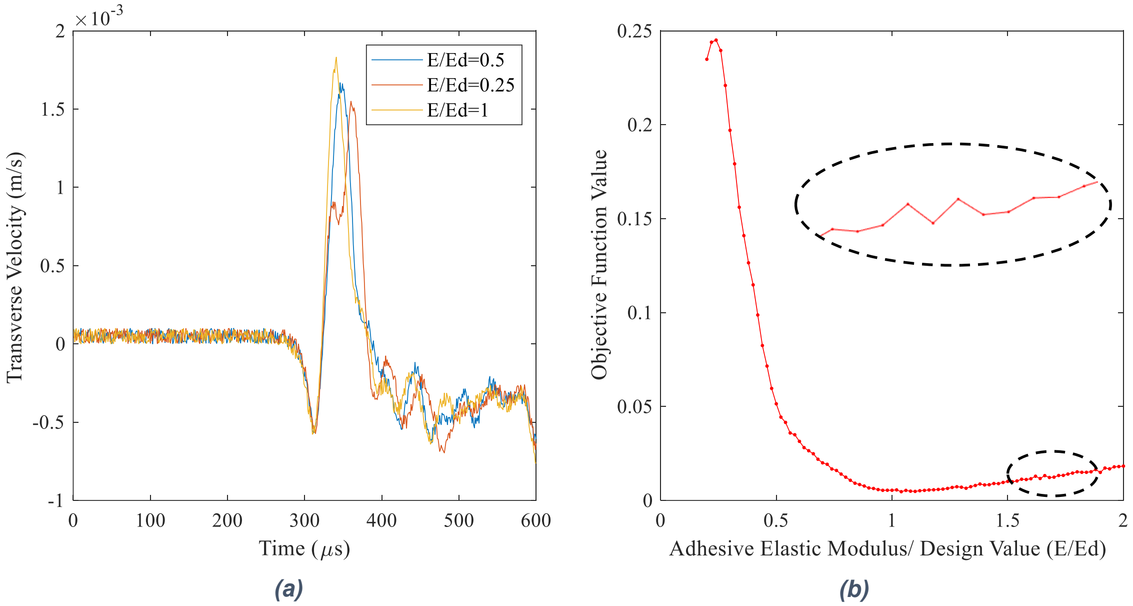

Figure 4.28 (a) Signals with added noise (b) the objective function with local fine fluctuations

This inaccurate value is obtained due to fine local minima in the objective function. In order to avoid fine local minima, the objective function calculation tolerance within the optimization algorithm is increased to $1\text{x}10^{-4}$ (from $1\text{x}10^{-6}$). The minimization process is repeated few times, and resulting optimized value is equal to $\boldsymbol{E/E_d} = 1.05$. This is very close to the design value despite of the 5% of random noise in the signal.

4.17 Case study: SLJ inspection using inverse problem approach

In this section, we present the use of inverse problem approach for the detection and estimation of the major damage types possible in an adhesive joint. The damage types include the variation of the adhesive elastic modus (cohesive damages), micro voids, debonding, and weak bonding. Later we present the use of this method as a quality assurance tool during the manufacturing state, and as an inspection tool during the operational life. The inverse problem approach is tested for a physical SLJs consist of different type of damages. The SLJ under investigation has the dimension identical to the FE model described above section.

4.17.1 Cohesive damages

The cohesive damage accounts for the variation of the mechanical properties of the adhesive layer from its design values. The reduction of the adhesive elastic modulus indicates process issues which results a reduction of the bond strength [56] [51]. On the other hand, increase of the adhesive elastic modulus increases the stress levels and reduces the safety factor of the structure. The elastic modulus of the adhesive layer is varied in the physical model, and the corresponding inverse problem solution is calculated. The solutions, solution time, and errors are given in Table 4.1. Additionally, the computational time and the estimated computational time for FE based inverse problem approach, are also given in Table 4.1. An equivalent FE SLJ model (explicit) takes about 30 seconds to complete a one iteration. The estimated total time is calculated by multiply the conventional FE solution time with the number of iterations. Note that this estimated time for FE solution does not include the computation time taken for the calculation of the objective function values. As shown in the table, the elastic modus of the adhesive layer is calculated with a considerable accuracy for each damage scenario. Most importantly, all the inspection (solution) times are less than 20 seconds.

Table 4.1 Inverse problem solution for different cohesive damages

Physical adhesive Elastic Modulus (Gpa)	Estimated Adhesive Elastic Modulus (Gpa)	Error as a (% Ed)	Number of iterations	Inspection time using WSFE (s)	Estimated inspection time using FE (s)
1.06 (E/Ed =25%)	1.14	-2%	29	17.4	870
1.69	1.82	-3%	27	16.2	810
2.12	2.16	-1%	19	11.4	570
4.24 (E/Ed=100%)	4.49	-6%	16	9.6	480
6.36	6.23	3%	22	13.2	660
8.47 (E/Ed =200%)	8.47	0%	26	15.6	780

4.17.2 Micro voids

Micro voids are formed due to the process issues and reduce the load bearing capacity of SLJ. Due to its scale and the distributed nature, the detection of micro voids is very difficult. Conventional ultrasonic inspection methods use the transmission or reflection characteristics due to the interaction with damage for detection. However, the wavelength should be comparable to the damage size for accurate damage detection. Therefore, it is not possible to identify accurate reflections or meaningful attenuation during transmission from these micro damages. Interestingly, the effective elastic modulus of the adhesive decreases with the micro voids. The reduction of the effective elastic modulus ($\boldsymbol{E_{Efct}}$) is profoundly governed by the void volume percentage ($\boldsymbol{vl}$). The size of the voids and inter-void interactions also influence the effective elastic modulus. However, the relationship between the ($\boldsymbol{E_{Efct}}$) and $\boldsymbol{vl}$ is not linear. Therefore, a second order trend line (using data point for $\boldsymbol{vl}$ =0%, $\boldsymbol{vl}$ = 15% and $\boldsymbol{vl}$ =25%) is constructed to estimate the void volume ratio with a reasonable accuracy (Figure 4.30).

Conversely, the void volume percentage can be back calculated from the value of the effective elastic modulus. The inverse problem approach is used to determine the effective elastic modulus of the adhesive layer, and the void volume percentage is calculated from the effective elastic modulus. An FE model is used to represent the physical structure (with micro voids). The adhesive layer of the SLJ is modeled with randomly place voids. A computer algorithm generated the random location of each void for a given void volume ratio. The adhesive layer is exclusively discretized with a fine mesh size, and the void size is controlled with the mesh size. The inverse problem solution is calculated for the SLJs which have 2.5%, 5%, 10%, 15%, 20%, and 55% of void volume percentages. The calculated void volume percentages and the actual percentages are given in Table 4.2.

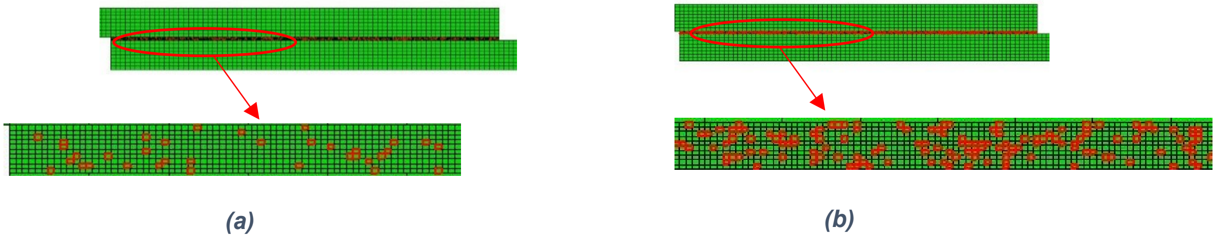

Figure 4.29 (a) 5% void volume percentage, (b) 15% void volume percentage

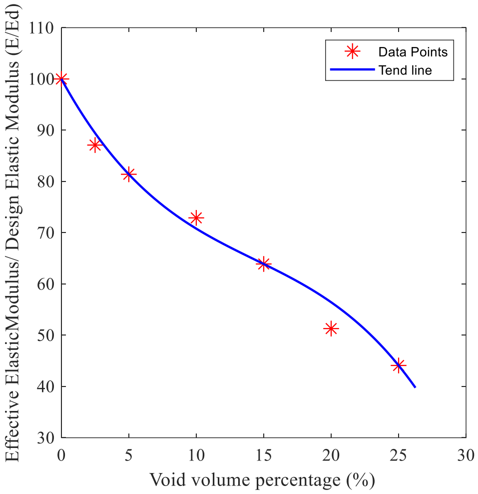

Figure 4.30 Effective elastic modulus variation with void volume percentage

Table 4.2 Calculated void volume percentages from Inverse Problem Solutions

Physical Void Volume percentage	Estimated Effective Adhesive Modulus	Estimated Void Volume percentage (Trend line)	Error (Trend line)
0	100	0.0	0%
2.5	87.1	2.5	2%
5	81.4	5.0	1%
10	72.9	9.6	-3%
15	63.9	15.0	0%
20	51.3	22.0	11%
25	44.1	25.0	0%

In addition to the micro voids, the cohesive defects also reduce the elastic modulus. Therefore, it is not possible to distinguish micro void damages from cohesive damages using this inspection technique. However, the technique is capable of detecting non-conforming SLJs which have micro voids.

4.17.3 Debonds

Debond are the most severe damage type in the adhesive layer. The Initial debonds should be detected during the manufacturing stage, and the debonds that exceed the critical debond length should be detected during the periodic inspection. The debonds may grow in length as the SLJ undergoes loadings. Once they reach its critical length, it may completely serve the adhesion between the adhesive and the adhered. Since the debond occur at the interface, it is difficult to identify the presence of debond using the traditional ultrasonic bulk waves (pulse echo or through transmission based) especially the ones such as kissing bonds. As mentioned above, the adhesive layer stiffness is calculated using Eq. 4.1 and Eq. 4.2. The presence of a debond reduces the net contact area between the adhesive and adherend, and therein reduces the adhesive layer stiffness. Further, the unbond area creates a kissing bond that produces the harmonics of the excitation frequency. The presence of a debond can be identified from the reduced adhesive stiffness and is distinguishable from other damage types due to the harmonic frequencies. The SLJ adhesive layer is modeled with debond (shown in Figure 4.31). The inverse problem approach is used to detect the presence of the damage and estimate the size of the debond. As shown in the Table 4.3, the presence of debonds as small as 5mm (5% of the total bonded length) results a considerable reduction of the effective stiffness. However, a clear relationship between the debond size and the effective stiffness cannot be determined. Especially, at larger debond sizes the load carrying capability or joint strength is likely to be deteriorating faster than stiffness reduction estimated by this technique. Yet the stiffness reduction offered by the present technique can serve as an indicator of otherwise difficult to detect defects such as kissing bonds.

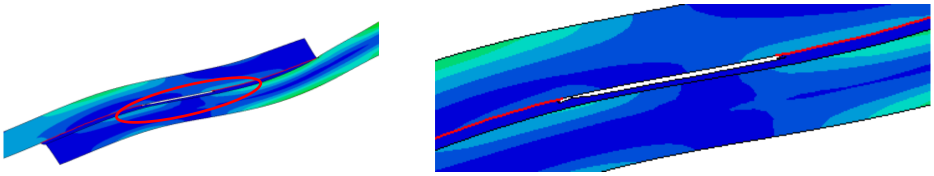

Figure 4.31 Debond region

Table 4.3 Estimated effective stiffness for debonds

Debond size (mm)	Estimated effective stiffness (%)
5	92
12.5	91
25	89
37.5	85

Presence of complete debonds are distinguishable due to the generation of harmonic frequencies. In order to examine for the harmonic frequencies, the SLJ is excited with a narrow band signal and the wave response is captured. The captured signal was then transformed into frequency and time-frequency domain using Fourier and wavelet transformations, respectively. The resulted transformations are shown in Figure 4.32. 50 kHz excitation is used for the wave generation, and the first harmonic of the excitation frequency is clearly visible in the graphs. As a summary, the reduction of the stiffness indicates a presence of a damage (possibly a debond), and the harmonics facilitate to distinguish debonds from other type of damages.

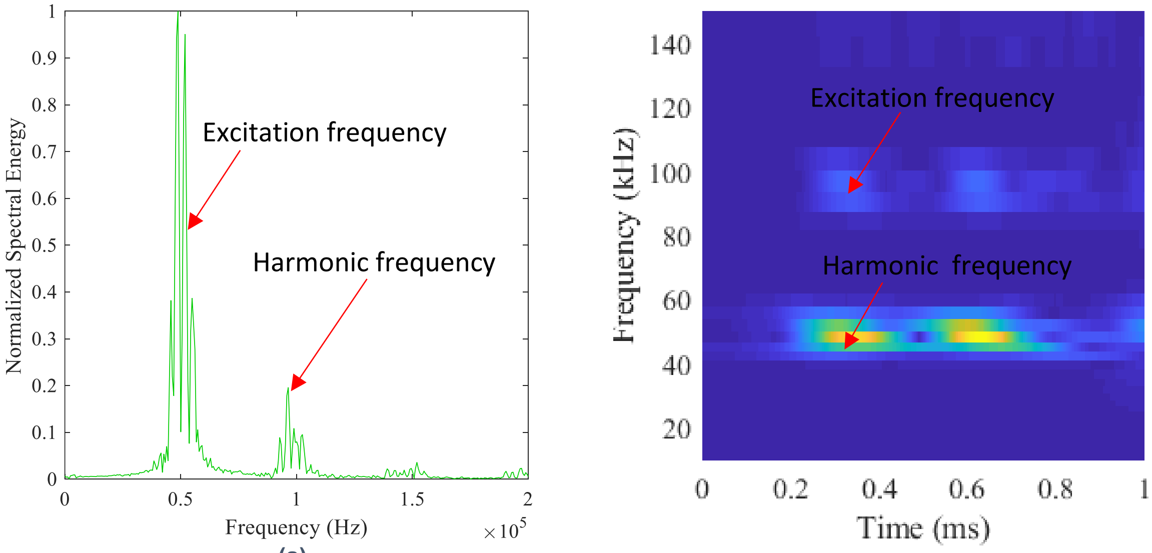

(a)

(b)

Figure 4.32 (a) Harmonic generation in frequency domain, (b) harmonic generation in frequency-time domain

4.17.4 Weak bonds

The erroneous bonding surface preparations, contaminations, and process issues result weak or partially bonded regions. The weak/partially bonded regions are similar to the debond areas. However, the adherends and adhesive are not completely disconnected. Similar to debonds, weak bonds reduce the effective adhesive stiffness. However, a reduction of the effective adhesive stiffness occurs due to the reduced bonding stiffness between the adherend and adhesive (similar to Gauthier's model [45]). The weak bonds are detected form the inverse problem approach, and the resulting stiffness values are given in Table 4.4. These values are very similar to the values obtained for debonds, and accurate relationship between the debond size and effective stiffness cannot be established. In the FE model which represent the physical SLJ, the connecting stiffness between the adherend and adhesive is assigned a low stiffness, for the simulation of the weak bonding. Unlike complete debonds, the weak bonds do not generate harmonics of the excitation frequency (Figure 4.33).

Table 4.4 Estimated effective stiffness for weak bond

Weak bond area size (mm)	Estimated effective stiffness
5	92
12.5	90
25	91
37.5	90

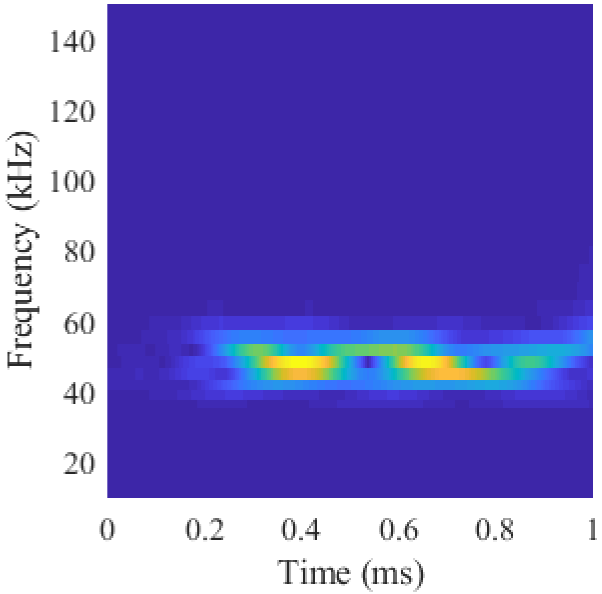

Figure 4.33 Time frequency diagram of the wave response

4.17.5 Applications in quality assurance

Quality assurance is part of the quality management of a product which provides the confidence that quality requirements are fulfilled. The quality requirements of a SLJ may include, the bond strength, bond stiffness (elastic modulus), bond layer thickness, and the finish. The bond layer thickness may be measured by the standard measuring equipment and gauges, and the adhesive joint finish is evaluated through the visual inspection. Importantly, the properties of the adhesive layer are not measurable prior to the fabrication and is governed by the manufacturing process/parameters. Additionally, the estimation of the bond stiffness and strength of the finished SLJ may require expensive mechanical testing. Specially, the destructive testing of coupons required for the bond strength measurements which is a key driver of manufacturing costs by requiring additional samples for testing. Since the adhesive properties are profoundly determined by manufacturing process, the bond strength can significantly vary from unit to unit. Katnam et al. [60] showed that the nature of the adhesive preparation techniques (mixing) significantly changes the bond strength for the same SLJ design. The dispenser mixing results about 50% of the improvement of the bond strength compared to that of the hand-mixed adhesive. Additionally, curing temperature, and the environment conditions during the adhesive curing also reduces the bond strength and bond stiffness. Moussa et al. [56] showed that the variations of the curing temperate considerably changes bond strength and the bond stiffness. Additionally, it has been shown that an approximately linear relationship exists between the bond strength and bond stiffness [56].

The inverse problem approach can be used to determine the stiffness of the adhesive layer during the quality assurance testing. Since the stiffness and strength has a linear relationship, the bond strength can be indirectly calculated from the adhesive stiffness. For instance, if the adhesive stiffness is reduced by 10%, then the bond strength is expected to be reduced by 10%. Therefore, this inverse problem approach can be used to detect and estimate the defects caused by erroneous process. The estimated damage severities (reduction of elastic modulus, void percentage, debond) can be used for the decision making.

This technique is readily be used in automated inspection systems in production lines. Figure 4.34 illustrates the equipment configuration for an automated inspection system. The wave is generated using a non–contact means for higher scanning speed. These non-contact wave generation methods include; air-coupled ultrasonic transducer, laser ablation, and Electro Magnetic Acoustic Transducer (EMAT). For the wave measurements, laser Doppler vibrometer, air-coupled ultrasonic transducers, and EMATs can be used. The traditional ultrasonic transducers require physical contact with the test specimen, and the couplant liquid are used for better energy transfer. Therefore, the traditional ultrasonic transducers hinder the inspection speed. The advantage of this technique over conventional automated ultrasonic inspection systems are given below;

- Scan the entire width of the bonded region with single measuring point. Therefore, point-to-point scan on the bonded region is not required.
- This method provides an estimation of the stiffness and the strength of the adhesive joint. Hence, this method facilitates value (numbers) based decision making in material review board.
- The acceptance or the rejection of units (SLJ) can be automated based on the estimated stiffness and strength values.
- Sensitive to wide range of damages.

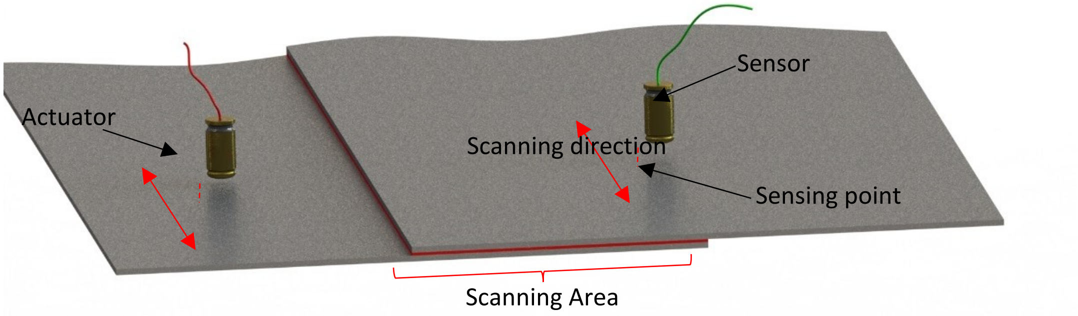

Figure 4.34 Automated adhesive bond inspection in quality assurance

4.17.6 Application in inspection for continued operation

SLJ exposure to humidity and temperature considerably reduce the bond stiffness and strength of SLJs. Nguyen at al. [51] showed that prolonged exposure to sea water and high level of humidity significantly reduce the elastic modulus and the bond strength. The elevated temperature further reduces the elastic modulus and bond strength caused by exposure to sea water. According to the Nguyen at al. [51], 1000 hours of exposure to 90% humidly reduces adhesive stiffness and strength by about 8%. The adhesive strengths is plotted against the corresponding stiffness values (Figure 4.35, data taken from [51]). The adhesive strength and the stiffness have an approximately linear relationship. Therefore, during the periodic inspection, this inverse problem approach can be used to determine the stiffness of the adhesive layer, and hence the corresponding adhesive strength can be calculated. Particularly, this technique requires a single point measurement recorded at the exposed side of the SLJ, and therefore very suitable for inspection of in-service structures.

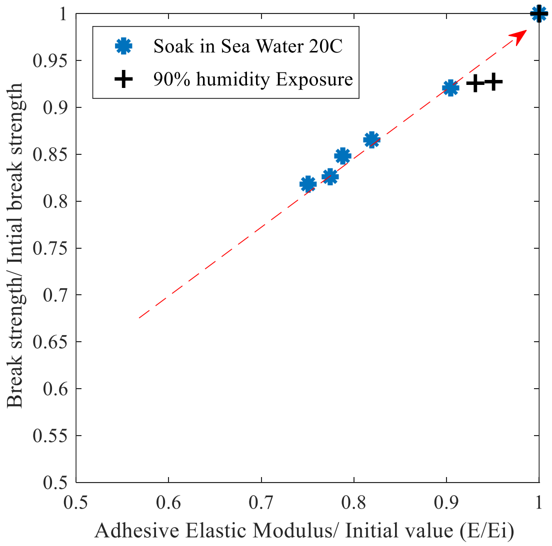

Figure 4.35 Adhesive layer environmental degradation, the relation between the degraded elastic modulus with degraded strength [51]

4.18 Conclusion of the chapter

In this study, we developed an inverse problem approach for the detection and estimation of major damage types possible in an adhesive joint. The damage types considered include cohesive damages, micro voids, debonds, and weak bonds. It was shown that the cohesive damages which relates to the mechanical properties of the adhesive layer, significantly reduce the factor of safety of the SLJ. Hence, the inverse problem was first developed to estimate the cohesive damages of the SLJ. The solution of the inverse problem is obtained through an optimization algorithm. In this work, the optimization algorithm is utilized along with the Wavelet Spectral Finite Element (WSFE) models, for the first time. The WSFE models are significantly faster than the conventional FE models, and therefore, a significant reduction of the computational time is achieved. Additionally, the proposed inverse problem technique requires a single data point for the inspection of the entire width of the bonded region. As a result, a significant reduction of data acquisition/ measurement time is achieved. Further, we reduced the (initially) global optimization problem into a local optimization problem and hence further enhancing the computational time. This results in a significantly reduced inspection time (aggregation of measuring and computation times). A considerably accurate estimation was obtained for the cohesive damages. Further, it was shown that the effective stiffness of the adhesive layer is influenced with the presence of micro voids, debonds and weak bonds. Therefore, the inverse problem approach is then used for the estimation of effective stiffness of the adhesive layer. The void volume percentage, presence of debond, and presence of weak bond are determined from the effective elastic modulus. Based on above observations following conclusions are made;

- The inverse problem approach is considerably accurate for the estimation of cohesive damages, and significantly faster than the similar methods which utilized conventional finite element methods
- The reduction of the elastic modulus of the adhesive layer (due to manufacturing process issues or environmental degradation) is linearly proportional to the bond strength. Therefore, the reduction of the bond strength is indirectly calculated from the elastic modulus estimated by this method.
- Presence of the micro voids decreases the effective stiffness of the adhesive layer. The inverse problem approach can be used to estimate the effective stiffness, and hence the void volume percentage is calculated.
- The effective stiffness of the adhesive layer significantly reduced with the presence of debonds and weak bonds. The reduction of the effective adhesive stiffness is captured using the inverse problem approach. However, the debond/weak bond size cannot be determined from this method
- The proposed method can be used as a quality assurance tool during the manufacturing process, and as an inspection tool during the operational life. The advantages of this method offer number of advantages over conventional ultrasonic inspection methods.
- This technique scans the entire width of the bonded region with single measuring point. Therefore, point-to-point scan on the bonded region is not required
- This method provides an estimation of the stiffness and the strength of the adhesive joint. Therefore, this method facilitates for value (numbers) based decision making in material review boards.

- The acceptance or the rejection of the unit (SLJ) can be automated based on the estimated stiffness and strength values calculated in this technique.
- Sensitive to wide range of damages.

CHAPTER V

INVERSE PROBLEM APPROACH USING ARTIFICIAL NEURAL NETWORKS

5.1 Introduction

The Artificial Neural Networks (ANN), which are inspired by the biological brain neural network, consist of a set of interconnected processing units called neurons. The ANN are being employed in number of fields including the natural speech recognition, computer vision, medical diagnosis, and classifications. The use of ANNs is increasingly popular in modeling the highly non-linear systems for which the conventional data fitting and the condition-based techniques are inadequate. The use of ANNs have also been reported in the field of Lamb wave-based structures health monitoring. Charles et al. [61] developed a shallow ANN for the estimation of the dimensions of a SLJ and a T-joint. A Lamb wave was excited in an adherend and the resulting wave motion was captured on the other adherend. The captured wave motion was then transformed into the frequency domain. The magnitudes of the frequency components were employed as ANN inputs for the classification of the bond line thickness. Here, the ANN classifies the joints into pre-defined categories based on the Lamb wave propagation across the joint. Most importantly, given the highly nonlinear nature of classification problem, a large number of training data is required. Chenhui et al. [62] utilized an ANN for the estimation of damage location and the severity. Similar to ref [61], the captured wave motion was de-noised and transformed into frequency domain. The wave motion was captured at four distinct sensing locations, and the features of the transformed waveform which correlate with the damage characteristic were extracted. The corresponding extracted features were then used to train the ANN. The damage location and the damage severity were estimated from the trained ANN. The transformation of the time-signal (wave motion) into the frequency domain is very common in Lamb wave-based ANN techniques. The transformed data reduces the influence of the environment noises and other type of waveform distortions. Additionally, the feature exactions (from the transformed data) reduces the number of inputs to ANN. For a given ANN, the accuracy of the ANN (how accurately the ANN can predict an output for a given inputs) reduces as the number of inputs increases. On the other hand, the increased number of training data (samples) improves the accuracy of a given ANN. Therefore, a large number of training data is required for an ANN which has a large number of inputs. Additionally, the number of required training data also depend upon the non-linearity of the problem. Feng et al. [63] used Time of Flight (ToF) of Lamb waves as inputs for the training of an ANN. The Lamb wave motion was measured at three different locations, and the ToF, the time taken by the Lamb wave to reach to the sensing point from the actuator, was calculated for each sensing point. In ref. [63], unlike ref [61] and ref [62], the wave motion was not transformed into the frequency domain. However, a reduced number of inputs were achieved through the use of ToF as inputs.

The solution of an inverse problem can be obtained through an optimization algorithm or through a trained ANN. In previous chapter, we employed optimization algorithms to reach the solutions of inverse problems. In this chapter, we utilize trained ANNs to obtain inverse problem solutions in order to estimate the cohesive damages of SLJs. The transverse velocity of the Lamb wave motion (time domain signal) along a SLJ is measured and given as the input for the ANN. The output of the ANN represents the current/ degraded elastic modulus of the adhesive layer. Generally, the accuracy of the ANN increases with its size. However, a large number of examples (training data) is required for an adequate training of a large ANN. Most of the reported works in literature have restricted their work into a limited number of inputs and smaller size of ANNs. In the damage detection of a SLJ, the training data may consist of the Lamb wave motion captured on the SLJs which have different adhesive layer elastic moduli. Given enough examples, the trained ANN is capable of predicting the elastic modulus of an unknown SLJ, when the Lamb wave motion along that particular SLJ is given as the input. However, it is not viable to fabricate a large number of SLJs (samples) with different adhesive elastic modulus. As a solution, the conventional FE models are used for the generation of Lamb wave motion through SLJs with different adhesive elastic moduli. This Lamb wave motion is then used as training data (in time domain or frequency domain). As mentioned in the previous chapter, the Lamb wave propagation simulation through SLJs is computationally expensive. Hence, generating a large set of training data (Lamb wave motion) consumes a considerable amount of time. As solution, in this work, we employ the WSFE SLJ model (described in previous chapter) for the generation the Lamb wave motion through SLJs with different adhesive elastic moduli, and a large number of training data is generated. Given the availability of a large set of training data, a relatively complex ANN is employed for accurate prediction of adhesive layer elastic modulus variations/cohesive damages.

5.2 Description of the ANN architecture

Figure 5.1 shows the general architecture of an ANN. However, depending on the function, the architecture of ANN can be significantly different to Figure 5.1. The neurons are grouped into several groups called layers. For example, this particular ANN has four layers (input, hidden layer 1, hidden layer 2, and output layer), and ***n*** inputs and one output.

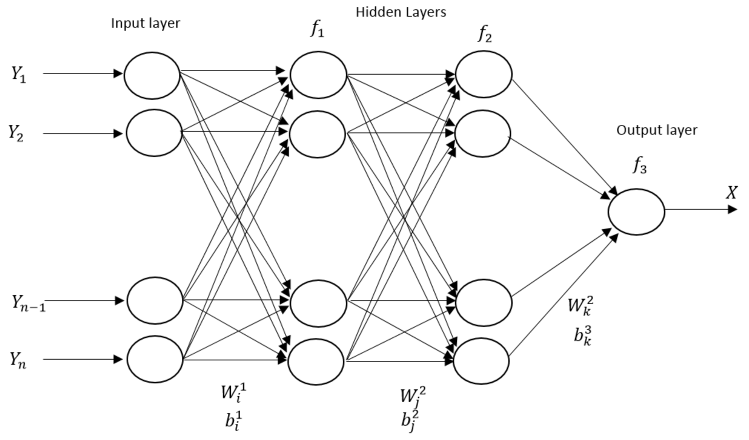

Figure 5.1 Schematic diagram of a basic ANN

The output of a single neuron is given by Eq. (5.1). The term, $Y_i(k)$ is ***i***th input for the neuron, $W_i(k)$ is the weight for the ***i***th input, ***b*** is the bias, ***f*** is the transfer function of neuron, and $X(k)$ is the output of the neuron.

$$X(k) = f\left(\sum_{i=1}^{m} W_i(k)\, Y_i(k) + b\right) \qquad 5.1$$

The output of the entire ANN shown in Figure 5.1 is given by Eq. (5.2). The terms ***m***, ***i***, ***j*** and ***k*** are the number of neurons in input layer, output layer, hidden layer 1, and hidden layer 2, respectively. The term, Y_p represent the ***p***th input. In this particular ANN, ***i*** =1 (one output).

$$X_i = f_1\left(\sum_{q=1}^{k} W_{q-i}^{1}(k)\, f_2\left(\sum_{r=1}^{j} W_{r-q}^{2}(k)\, f_1\left(\sum_{p=1}^{m} W_{p-r}^{1}(k)\, Y_p(k) + b_r^1\right) + b_q^2\right) + b_i^3\right) \qquad 5.2$$

Generally, the accuracy of a given ANN increases with its size (given by number of neurons and layers). However, a large number of training data set is need for a large size ANN. In this work we have employed a relatively large ANN. The size of the ANN is selected in trial and error by considering the minimum error between the true output and the target output. The ANN used in this work has 300 inputs, 30 neuron hidden layer, 30 neuron hidden layer, and one output layer. The Tan-Sigmoid transfer function (Eq. 5.3) is used for the hidden layers and a linear transfer function is used in output layer (5.4).

$$X(k) = \frac{2}{1+e^{-2n}} - 1 \; where, n = \sum_{i=1}^{m} W_i(k)\, Y_i(k) + b \qquad 5.3$$

$$X(k) = \sum_{i=1}^{m} W_i(k)\, Y_i(k) + b \qquad 5.4$$

5.3 Input/out of ANN

For this study, a WSFE SLJ model is used to generate the Lamb wave motion. In the SLJ model, the adherends consist of AS4/350-6 graphite-epoxy composites. The design adherend thickness is 0.001 m, and the width is 0.02m. The layup sequence of the laminate is taken as $[0]_{10}$. The adhesive layer consists of Hysol EA 9394 epoxy based structural adhesive with the design elastic modulus ($\boldsymbol{E_d}$) and the Poison's ratio equal to 4.24 GPA and 0.45, respectively. An example wave motion is shown in Figure 5.2. The wave amplitude in each sampling point in the time signal is used as the input. For example, this particular wave signal consists of 500 sampling points. However, first two hundred sample points have a near zero amplitude. Therefore, the portion of the wave signal of which the amplitude is near zero, is excluded from the analysis. The output of ANN is selected as the current elastic modulus.

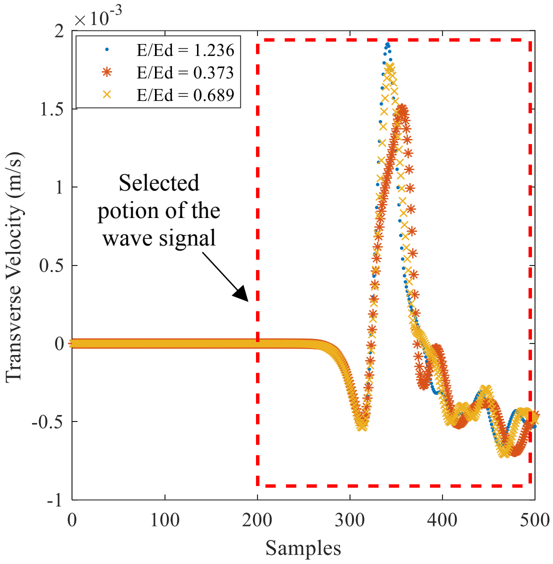

Figure 5.2 Lamb wave motion for different adhesive elastic moduli

5.4 Training of the ANN

A total of 1000 training data (transverse velocity of Lamb wave motions) is created using the WSFE SLJ model. The upper limit of targets of the training data is selected as $E/E_d = 2$ (E =8.47 Gpa), and the lower limit is selected as E/E_d=0.3 (E=1.27 Gpa). The advantage of using the WSFE SLJ model is its superior computation speed. For this particular situation, the WSFE SLJ model consumed only about 600 seconds to generate the aforementioned training data sets. However, if a conventional FE model was employed, an estimated time of 30,000 seconds is consumed. The training data (wave motion) is then used for the training of the ANN. The Bayesian regularization back propagation network training function is used in training. The Bayesian regularization back propagation updates the values of weights and bias according to the Levenberg-Marquardt optimization [64]. First, a limited number of training data is used to check the accuracy of the ANN. In following example, only 50 training examples are used for training, 7 training samples are used for validation of the results, and 7 samples are used for the testing of the ANN. The mean square error of the training is given in Figure 5.3.

According to the Figure 5.3, the network adjusted the corresponding weights and bias values to fit to the data used for the training. However, the error for the data which is not used for the training (validation and testing) is comparatively high. This implicates that the trained ANN produces erroneous output for unknown Lamb wave motion given as the input. This phenomenon is called “overtraining”; the network is over-trained to only predict the output data used for training. This condition can be improved by increasing the number of training data.

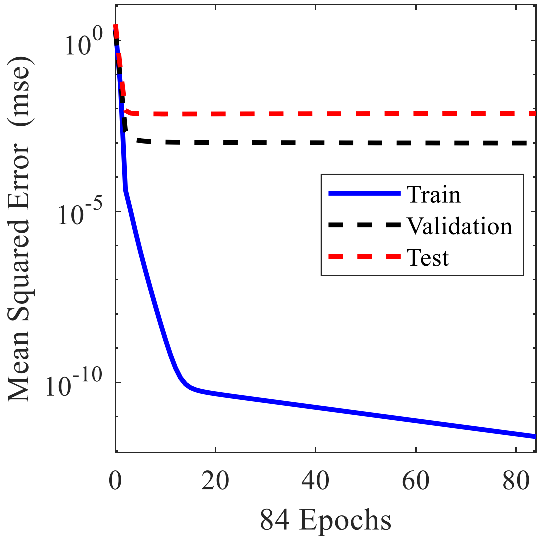

Figure 5.3 Performance of the ANN trained with fifty samples

The entire set of the training data (1000 wave motion data) is used for the training of the ANN. The mean square error of the training and the histogram of error is shown in Figure 5.4 (a) and Figure 5.4 (b) respectively. As shown in the Figure 5.4, the errors are considerably small. Therefore, the network is considered to be more generalized. When the network is given an unknown Lamb wave motion which is not used for the training purpose, the network should be able predict the elastic modulus with a reasonable accuracy.

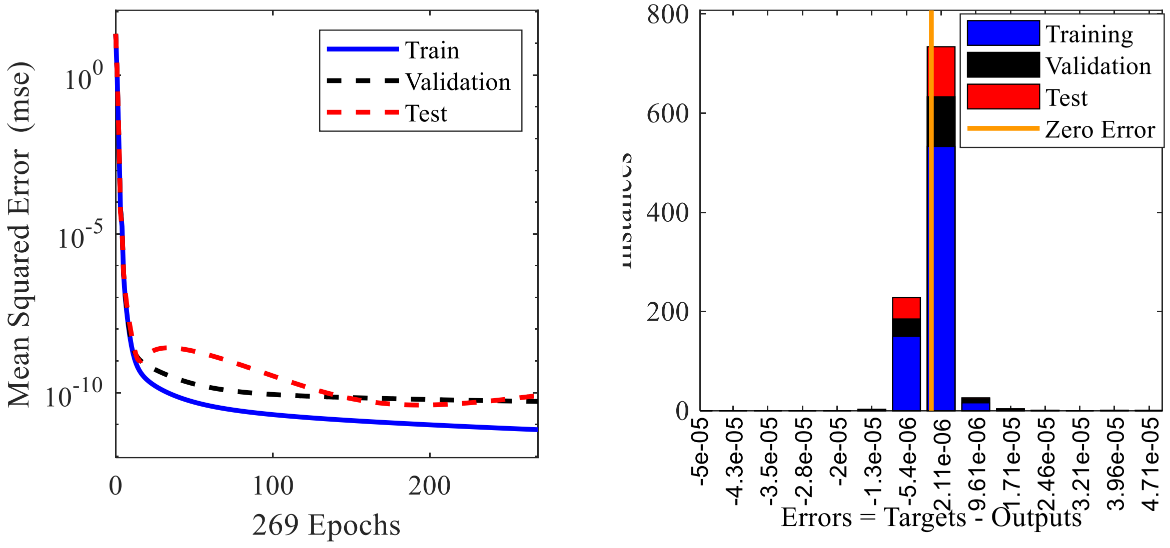

(a) (b)

Figure 5.4 The performance of trained ANN (a) mean square error (b) histogram of error

5.5 Use of the trained ANN

The trained ANN is used for the prediction of the elastic modulus of the defective SLJs. The WSFE SLJ model is used to generate the Lamb wave motion through SLJs with known adhesive elastic moduli. The resulting Lamb wave motion is then fed into the trained ANN, and the corresponding outputs/predictions are recorded. As mentioned above, the upper limit of targets of the training data is selected as $E/E_d = 2$ (E =8.47 Gpa), and the lower limit is selected as E/E_d=0.3 (E=1.27 Gpa). The Lamb waves are generated for the SLJs which have adhesive elastic moduli values that fall inside and outside of the range of the target values used in training. Table 5.1 presents the predictions, the true values and the error of estimation.

Table 5.1 The results of the trained ANN

WSFE model adhesive Elastic Modulus (Gpa)	Estimated Adhesive Elastic Modulus (Gpa)	Error (%)
10.59	13.30	26%
9.32	10.00	7%
8.47 (E/Ed =2)	8.47	0%
7.63	7.63	0%
6.36	6.36	0%
5.08	5.08	0%
4.24	4.24	0%
3.39	3.39	0%
2.12	2.12	0%
1.27 (E/Ed =0.3)	1.27	0%
1.06	3.47	228%
0.85	4.60	443%

According to Table 5.1, for the elastic moduli which lie within the range of the target values used in training, the error of the estimation is negligible. However, the prediction is significantly erroneous when the elastic moduli is outside of the range of the target values used in training. Therefore, this trained network cannot be used to predict the degradation of elastic modules of which the values lie outside of the range of target values used for training. The back calculation of the adhesive elastic modulus by only considering the Lamb wave propagation is relatively complex, and a highly non-linear problem. However, having a large number of training data facilitate to generate an ANN with a significant accuracy. The main advantage of use of the trained ANN over the optimization algorithms is that the ANN estimate the adhesive elastic modulus instantaneously while the optimization algorithms consume a notable amount of time for the estimation.

The trained ANN is then used for the estimation of the adhesive elastic modulus of a physical SLJ. Similar to the previous chapter, a conventional FE SLJ model is used to represent the physical SLJ. In the physical model, the adherends consist of AS4/3501–6 graphite-epoxy composites. The design adherend thickness is 0.001 m, and the width is 0.02m. The layup sequence of the laminate is taken as $[0]_{10}$. The adhesive layer consists of Hysol EA 9394 epoxy based structural adhesive with the design elastic modulus ($\boldsymbol{E_d}$) and the Poison's ratio equal to 4.24 GPA and 0.45, respectively. The Lamb wave motion recorded in the physical SLJ is used as the input for the trained ANN in order to estimate the corresponding elastic modules in the physical SLJ. The obtained estimations are given in Table 5.2.

Table 5.2 The results of the trained ANN for physical SLJ

Physical adhesive Elastic Modulus (Gpa)	Estimated Adhesive Elastic Modulus (Gpa)	Error (%)
6.35	8.38	32%
4.23	11.86	180%
2.11	3.59	70%
1.69	3.50	107%

As shown in Table 5.1, use of large number of training data increase the accuracy of ANN. However, the disadvantage of using the large number of training data is that the ANN losses the generality and become very sensitive slight distortion of the wave motions. As shown in chapter IV, the slight deviation exists between the WSFE model generated wave motion and the physical Lamb wave motion due to the differences in wave velocities, environment noises, measuring delays, and approximations made in WSFE formulation. When, an ANN which is trained with WSFE model generated wave motion, is employed for the prediction of the elastic modulus of a physical SLJ, the obtained ANN output (the inverse solution) is significantly different to the actual value of the elastic modulus of the physical SLJ. This is very clearly demonstrated form the data presented in Table 5.2. Therefore, due to slight deviation between the WSFE model generated wave motions and the wave motion recorded in the physical SLJ, the ANN is not able to predict the SLJ adhesive elastic modulus accurately. In order to circumvent this issue, the ANN configuration is modified as a classification problem.

5.6 Classification of the SLJ

The inverse problem approach is modified into a classification problem. Instead of estimating the current adhesive elastic modulus through the inverse problem solution, the ANN now classifies given SLJs into pre-defined categories depending upon the values of their adhesive layer elastic modulus. In quality assurance or in-service inspection, the inspector should ultimately make the decision to accept, reject, or rework the SLJ. Therefore, the classification of SLJs holds a great practical value over the direct estimation of the adhesive elastic modulus. The simplest SLJ classification categories are “acceptable” and “unacceptable”. For the purpose of demonstrating the capability of WSFE model trained ANN, in this work the SLJs are classified into six categories. Note that the category labels are not specific, the operator may change the labels according to the working experience with a particular SLJ configuration. The modified architecture of ANN is shown in Figure 5.5. The modified ANN consists of 300 inputs, four hidden layers (each with 30 nodes), and 6 outputs. The number of layers and number of nodes per-layer are increased until a no further improvement of the accuracy is obtained. The classification criteria are given in Table 5.3. Each target value ($\boldsymbol{X_i}$) holds one or zero. For example, if the actual elastic modulus of a given SLJ is within [0.9, 1.1] range, the output $\boldsymbol{X_3}$ is set to one and all other outputs sis zero. Note that, in training data, very different wave motions ($\boldsymbol{Y_i}$) may have the same output ($\boldsymbol{X_i}$).

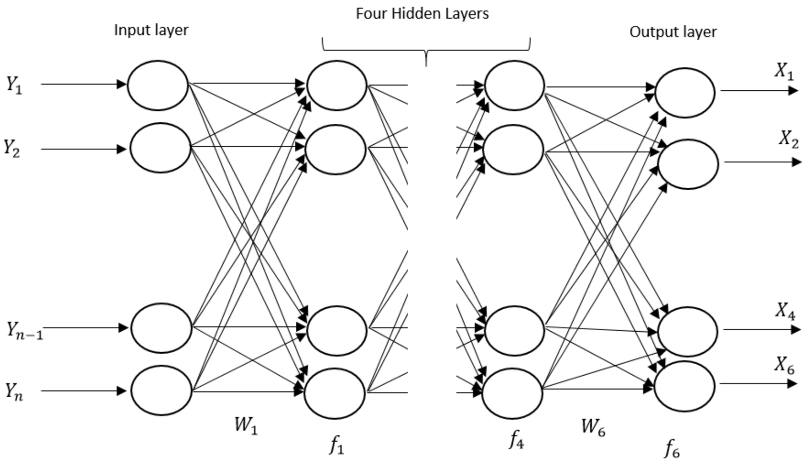

Figure 5.5 The ANN architecture for the classification problem

Table 5.3 Classification criteria

Output	E/Ed Range (Gpa)	Labels
X_1	E/Ed > 1.5	A
X_2	1.5 ≥ E/Ed > 1.1	B
X_3	1.1 ≥ E/Ed > 0.9	C (acceptable)
X_4	0.9 ≥ E/Ed >0.7	D
X_5	0.7 ≥ E/Ed > 0.5	E
X_6	0.5 ≥ E/Ed	F

Generally, the classification problems are considerably non-linear compared to the regression problems. In order to handle the high non-linearity, the size of the ANN is increased. Further, the size of the training data is increased to two thousand (2000) samples. The WSFE SLJ model is used to generate the training data (the transverse velocity of Lamb wave motion) for SLJs with randomly selected adhesive elastic moduli. The range of the target values is kept within ***E/E*$_d$** =0.3 to ***E/E*$_d$**=2. The ANN is trained with the training data, and the performance of the trained ANN is given in Figure 5.6.

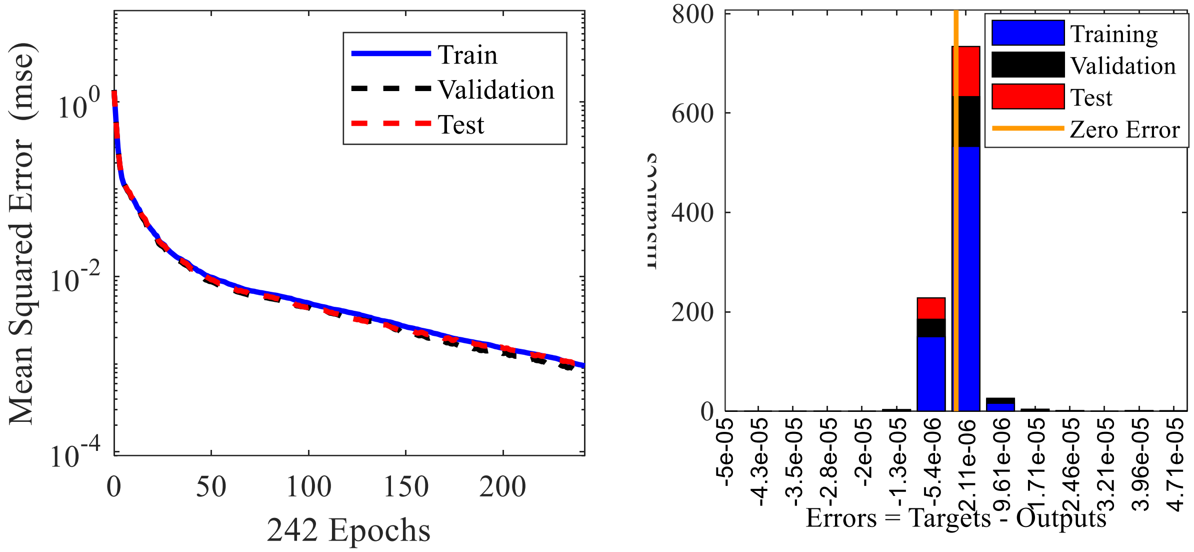

Figure 5.6 The performance of trained classification ANN (a) mean square error (b) histogram of error

As shown in Figure 5.6, even though a large number of training data is used, the error of estimation is significantly higher than that of the regression problem. This is due to the higher non-linearity of the classification problem.

5.7 Use of the trained classification ANN

The trained ANN is used for the estimation of the adhesive elastic moduli of physical SLJs. Even though, the target values (***X$_i$***) hold one or zero, the predictions (output) of ANN is calculated as a real number (<1.00). The calculated numbers are rounded to obtain the corresponding category. The results of the classification of physical SLJs using the trained ANN is given in Table 5.4.

Table 5.4 Classification problem results

Physical adhesive Elastic Modulus (GPa)	The Predictions [X]	Category
1.5	[0,1,0,0,0,0]	B
1	[0,0,1,0,0,0]	C (Acceptable)
0.5	[0,0,0,0,1,0]	E
0.4	[0,0,0,0,0,1]	F
0.25	[0,0,0,0,0,1]	F
2	[0,1,0,0,0,0]	B

As shown in Table 5.4, the trained ANN successfully classified the given SLJs into the relevant categories by considering the Lamb wave motion. However, the classification for ***E/Ed*** =2 is erroneous. This is the upper limit of the training data, and therefore insufficient training data around ***E/Ed*** =2 may cause this issue.

5.8 Conclusion of the chapter

In this chapter, the artificial neural networks were used to estimate the cohesive damages /adhesive elastic modulus variation of SLJs. The ANNs were utilized to obtain the solutions for two distinct problem types; regression and classification. In regression, the ANNs were trained with the WSFE SLJ model generated Lamb wave motion. The transverse velocity of the Lamb wave motions generated for SLJs with randomly selected adhesive elastic moduli were given as the input for the ANN. The corresponding adhesive layer elastic moduli were given as the target value for ANN training. The Bayesian regularization back propagation network training function was employed in the network training. The trained ANN successfully estimated the elastic modulus of the SLJs when the WSFE SLJ model generated wave motion data was given as the input. However, due to the slight variation between the WSFE SLJ model generated wave motion and the physical SLJ wave motion, the trained ANN produced inaccurate estimations for the physical (degraded/damaged) SLJs. The ANN was then modified as a classification problem. Instead of estimating the true value of the adhesive elastic modulus through the inverse problem solution, the modified ANN classifies the given SLJs into the pre-defined categories depending upon the value of the adhesive elastic modulus. In quality assurance or in-service inspection, the inspector should ultimately make the decision to accept, reject, or rework the SLJ. Hence, the classification of SLJs holds a great practical value over the direct estimation of the adhesive elastic modulus. In this work, the SLJs were categorized into six categories. The transverse velocity of the WSFE SLJ model generated Lamb wave motion was given as the input for the ANN and the corresponding category of the SLJs is given as the targets. Each target value ($\boldsymbol{X}_i$) holds one or zero. Once trained, the ANN successfully classified the given SLJs into categories. Based on the current study, following conclusions are made:

1. Use of WSFE models significantly reduces the computation time required for the generation of large set of training data.
2. The accuracy of the ANN increases with the number of the training data. Thus, the use of WSFE model for the generation of a large set of training data is particularly important.
3. In contrast, the use of large set of training data reduces generality of the ANN and make the ANN very sensitive slight distortion of the Wave motion
4. Slight deviation exists between the WSFE model generated wave motion and the physical Lamb wave motion due to the differences in wave velocities, environment noises,

measuring delays, and approximation in WSFE formulation. Due to these deviations, when prediction the elastic modulus of a physical SLJ, the ANN which is trained with WSFE model generated wave motion produces inaccurate results.

5. The classification ANN successfully classifies a given physical SLJs into pre-defined categories by considering the Lamb wave motion along the physical SLJ.
6. The proposed ANN based classification technique can successfully be used in industry (especially in automated setup) for the quality assurance and in-service inspection of SLJs.
7. The major advantage of use of the trained ANN over the optimization algorithms is that the ANN classifies a given SLJ instantaneously while the optimization algorithms consume a notable amount of time for the estimation.

REFERENCES

[1] Charles Farrar,Michael B. Prime, "Damage Identification and Health Monitoring of Structural and Mechanical Systems From Changes in their Vibration Characteristics: A literature Review," *The Shock and Vibration Digest,* 1996.

[2] Nimesh Jayakody, Ratneshwar Jha, Thomas E Lacy, "Damage Diagnostics of Composite Fan Blades Using the Modified Time Reversal Method," in *ASME 2015 Gas Turbine India Conference. American Society of Mechanical Engineers*, Hyderabad, India, 2015.

[3] V. Giurgiutiu, Structural Health Monitoring with Piezoelectic Wafer Active Sensors, Elsevier, 2008.

[4] V. Giurgiutiu, Structural Health Monitoring: with Piezoelectric Wafer Active Sensors, Elsevier, 2007.

[5] P.D. WILCOX, M.J.S. LOWE AND P. CAWLEY, "Mode and Transducer Selection for Long Range Lamb Wave Inspection," *JOURNAL OF INTELLIGENT MATERIAL SYSTEMS AND STRUCTURES,* vol. 12, 2001.

[6] zhongqing Su, Lin Ye, Ye Lu, "Guided lamb waves for identification of damage in composite structures: A review," *Journal of Sound and Vibration ,* vol. 295, pp. 753-780, 2006.

[7] Sang Jun Lee, Navneet Gandhi, Jennifer E. Michaels, and Thomas E. Michaels, "Comparison of the Effects of Applied Loads and Temperature," *Quantitative Nondestructive,* vol. 30, 2011.

[8] Ashkan Khalili, Ratneshwar Jha, and Nimesh Jayakody, "Structural Health Monitoring of Skin-Stiffener Structures Using WSFE-based User Defined Elements in Abaqus," in *25th AIAA/AHS Adaptive Structures Conference, AIAA SciTech Forum*, Grapevine, Texas, 2017.

[9] Nimesh Jayakody, Ratneshwar Jha, Ashkan Khalili and Dulip Samaratunga, "Assessment of Adhesively Bonded Joint Health Status using Wavelet Spectral Finite Element Method," in *25th AIAA/AHS Adaptive Structures Conference, AIAA SciTech Forum*, Grapevine, Texas, 2017.

[10] Nimesh Jayakody, Ratneshwar Jha and Dulip Samaratunga, "Wavelet Spectral Finite Element Modeling for Health Monitoring of Adhesively Bonded Joints," in *24th AIAA/AHS Adaptive Structures Conference, AIAA SciTech Forum*, San Diego, California, USA, 2016.

[11] M. Fink, "Time Reversal of Ultrasonic Fields-Part I: Basic Principles," *IEEE TRANSACTIONS ON ULTRASONICS, FERROELECTRICS,ANDFREQUENCYCONTROL,* vol. 39, no. 5, pp. 555-566, 1992.

[12] Francois Wu, Jean-Louis Thomas, and Mathias Fink, "Time Reversal of Ultrasonic Fields-Part 11:Experimental Results," *IEEE TRANSACTIONS ON ULTRASONICS, FERROELECTRICS, AND FREQUENCY CONTROL,* vol. 39, no. 5, pp. 567-578, 1992.

[13] Mathias Fink, Didier Cassereau, Arnaud Derode, Claire Prada, Philippe Roux, Mickael Tanter,Jean-Louis Thomas and Fran¸cois Wu, "Time-reversed acoustics," *Reports on Progress in Physics,* vol. 63, pp. 1933-1995, 2000.

[14] Hyun Woo Park, Seung Bum Kim, Hoon Sohn, "Understanding a time reversal process in Lamb wave propagation," *Wave Motion,* vol. 46, pp. 451-467, 2009.

[15] Ros K. Ing and Mathias Fink, "Time recompression of dispersive lamb waves using a time reversal mirror. Application to flaw detection in thin plates," in *1996 IEEE ULTRASONICS SYMPOSIUM*, 1996.

[16] Ros K. Ing and Mathias Fink, "Time-Reversed Lamb Waves," *ieee transactions on ultrasonics, ferroelectrics, and frequency control,* vol. 45, no. 4, pp. 1032-1043, 1998.

[17] L. R. F. Rose and C. H. Wang, "Mindlin plate theory for damage detection: Source solutions," *The Journal of the Acoustical Society of America,* vol. 116, no. 1, pp. 154-171, 2004.

[18] Chun H Wang, James T Rose and Fu-Kuo Chang, "A synthetic time-reversal imaging method for structural health monitoring," *SMART MATERIALS AND STRUCTURES,* vol. 13, p. 415–423, 2004.

[19] R. Gangadharan, C.R.L. Murthy, S. Gopalakrishnan, M.R. Bhat, "Time reversal technique for health monitoring of metallic structure using Lamb waves," *Ultrasonics,* vol. 49, pp. 696-705, 2008.

[20] Hoon Sohn; Hyun Woo Park; Kincho H. Law; and Charles R. Farrar, "Damage Detection in Composite Plates by Using an Enhanced Time Reversal Method," *JOURNAL OF AEROSPACE ENGINEERING,* vol. 20, no. 3, pp. 141-151, 2007.

[21] Buli Xu and Victor Giurgiutiu, "Single Mode Tuning Effects on LambWave Time Reversal with Piezoelectric Wafer Active Sensors for Structural Health Monitoring," *Journal of Nondestructive Evaluation,* vol. 26, pp. 132-134, 2007.

[22] Hyunwoo Park, Hoon Sohn and Kincho H. Law, "Damage Detection in Composite Plates by Using Time Reversal Active Sensing".

[23] Ryan Watkins and Ratneshwar Jha, "A modified time reversal method for Lamb wave based diagnostics of composite structures," *Mechanical Systems and Signal Processing,* vol. 31, pp. 345-354, 2012.

[24] Sang Jun Lee, Hoon Sohn and Jung-Wuk Hong, "Time Reversal Based Piezoelectric Transducer Self-diagnosis Under Varying Temperature," *Journal of Nondestructive Evaluation,* vol. 29, pp. 75-91, 2010.

[25] Lei Qiu, Shenfang Yuan, Xiaoyue Zhang and YuWang, "A time reversal focusing based impact imaging method and its evaluation on complex composite structures," *Smart Materials and Structures,* vol. 20, 2011.

[26] Wang Tao, Liu Shaopeng, Shao Junhua and Li Yourong, "Health monitoring of bolted joints using the time reversal method and piezoelectric transducers," *Smart Materials and Structures,* vol. 25, 2016.

[27] Yabin Liang, Dongsheng Li, Qingzhao Kong, and Gangbing Song, "Load Monitoring of the Pin-Connected Structure Using Time Reversal Technique and Piezoceramic Transducers—A Feasibility Study," *IEEE SENSORS JOURNAL,* vol. 16, no. 22, pp. 7958-7966, 2016.

[28] Guofeng Du1, Qingzhao Kong, Fanghong Wu, Jiabiao Ruan and Gangbing Song, "An experimental feasibility study of pipeline corrosion pit detection using a piezoceramic time reversal mirror," *Smart Materials and Structures,* vol. 25, 2016.

[29] Jian Cai, Lihua Shi, Shenfang Yuan and Zhixue Shao, "High spatial resolution imaging for structural health monitoring based on virtual time reversal," *SMART MATERIALS AND STRUCTURES,* vol. 20, 2011.

[30] Zenghua Liu, Hongtao Yu, Junwei Fan, Yanan Hu, Cunfu He and Bin Wu, "Baseline-free delamination inspection in composite plates by synthesizing noncontact air-coupled Lamb wave scan method and virtual time reversal algorithm," *Smart Materials and Structures,* vol. 24, 2015.

[31] "RSV-150 Remote Sensing Vibrometer," polytec, 30 May 2017. [Online]. Available: http://www.polytec.com/us/products/vibration-sensors/special-application-vibrometers/rsv-150-remote-sensing-vibrometer/.

[32] V. Giurgiutiu, Strucutral Health Montoring with Piezoelectric Wafer Active Sensor, Elsevier, 2008.

[33] Ryan Watkins and Ratneshwar Jha, "A modified time reversal method for lamb wave based diagnostics of compsite structures," *Mechanical Systems and Signal Processing,* vol. 31, pp. 345-354, 2012.

[34] "STEMiNC STEINER & MARTINS, INC," [Online]. Available: http://www.steminc.com/piezo/PZ_property.asp. [Accessed October 2015].

[35] Dulip Samaratunga, Ratan Jha, S. Gopalakrishnan, and A. Messac, "Wavelet spectral finite element modeling for wave propagation in adhesively bonded composite joints," in *23rd AIAA/ASME/AHS Adaptive Structures Conferance, AIAA Science and Technology Forum 2015*, Kissimme, Florida, 2015.

[36] Dulip Samaratunga, Ratneshwar Jha and S. Gopalakrishnan, "Wave propagation analysis in adhesively bonded composite joints using the wavelet spectral finite element method," *Composite Structures,* vol. 122, pp. 271-283, 2015.

[37] Louis C. (Lou) Dorworth and Dr. Giles Dillingham, *Fundamentals of Adhesive Bonding of Composite Materials,* Fort Worth, TX, 2017.

[38] M. J. Santos, J. Perdiga˜o, and P. Faia, "Ultrasonic Guided Waves Scattering Effects From Defects in Adhesively Bonded Lap Joints Using Pitch and Catch and Pulse-Echo Techniques," *The Journal of Adhesion,* vol. 84, pp. 421-438, 2008.

[39] Max Davis, *FAA Workshop on Best Practice in Adhesive Bonding.*

[40] W.H.Ong, N.Rajic, W.K.Chiu, C.Rosalie, "Adhesive material property evaluation for improved Lambwave simulation," *International Journal of Adhesion & Adhesives,* vol. 71, pp. 28-38, 2016.

[41] Juergen Koreck ,Christine Valle, Jianmin Qu and Laurence J. Jacobs, "Computational Characterization of Adhesive Layer Properties Using Guided Waves in Bonded Plates," *J Nondestruct Eval,* vol. 26, p. 97–105, 2007.

[42] M. R. Karim, A. K. Mal, and Y. Bar-Cohen, "Inversion of leaky Lamb wave data by simplex algorithm," *The Journal of the Acoustical Society of America,* vol. 88, 1990.

[43] Francesco Lanza Di Scalea, Howard Matt, Ivan Bartoli, Stefano Coccia, Gyuhae Park and Charles Farrar, "Health Monitoring of UAV Wing Skin-to-spar Joints using Guided Waves and Macro Fiber Composite Transducers," *Journal of Intelligent Material Systems And Structures,* vol. 18, pp. 373-388, 2007.

[44] Howard Matt, Ivan Bartoli, and Francesco Lanza di Scalea, "Ultrasonic guided wave monitoring of composite wing skin-to-spar bonded joints in aerospace structures," *Journal of Acoustical Society of America,* vol. 118, pp. 2240-2252, 2005.

[45] Camille Gauthie, Mounsif Ech-Cherif El-Kettani, Jocelyne Galy, Mihai Predoi, Damien Leduc, Jean-Louis Izbicki, "Lamb waves characterization of adhesion levels in aluminum/epoxy bi-layers with different cohesive and adhesive properties Adhesives," *International Journal of Adhesion and Adhesives,* vol. 74, pp. 15-20, 2017.

[46] Sun Hong-Xiang, Xu Bai-Qiang, Zhang Hua, Gao Qian and Zhang Shu-Yi, "Influence of adhesive layer properties on laser-generated ultrasonic waves in thin bonded plates," *Chin. Phys. B,* vol. 22, p. 014302, 2011.

[47] Wern Hann Ong, Nik Rajic, Wing Kong Chiu and Cedric Rosalie, "Lamb wave–based detection of a controlled disbond in a lap joint," *Structural Health Monitoring,* vol. 17, pp. 668-683, 2018.

[48] Yoji Okabe1, Junichiro Kuwahara, Kazuki Natori,Nobuo Takeda, Toshimichi Ogisu, Seiji Kojima and Shinji Komatsuzaki, "Evaluation of debonding progress in composite bonded structures using ultrasonic waves received in fiber Bragg grating sensors," *SMART MATERIALS AND STRUCTURES,* vol. 16, pp. 1370-1378, 2007.

[49] Fucai Li1, Hideaki Murayama, Kazuro Kageyama,Guang Meng, Isamu Ohsawa and Takehiro Shirai, "Debonding detection using a self-calibration sensor network," *SMART MATERIALS AND STRUCTURES,* vol. 19, 2010.

[50] Paul A. Cooper and James Wayne Sawyer, "Critical Examination of Stress in an Elastic Single Lap Joint," *NASA Tehcnical PAper 1507,* 1979.

[51] Tien-Cuong Nguyen, Yu Bai, Xiao-Ling Zhao, Riadh Al-Mahaidi, "Durability of steel/CFRP double strap joints exposed to sea water, cyclictemperature and humidity," *Composite Structures,* vol. 94, 2012.

[52] A.D. Crocombe, D.A. Bigwood and G. Richardson, "Analysing joints for structural adhesive failure," *INT.J.ADHESION AND ADHESIVES,* vol. 10, no. 2, 1990.

[53] L. TONG, "STRENGTH OF ADHESIVEL Y BONDED SINGLELAP AND LAP-SHEAR JOINTS," *1nl. J. Solids Struclure,* vol. 35, no. 20, 1998.

[54] M.S. Kafkalidis and M.D. Thouless, "The effects of geometry and material properties on the fracture of single lap-shear joints," *International Journal of Solids and Structures,* vol. 39, p. 4367–4383, 2002.

[55] Fabrice Lapique, Keith Redford, "Curing effects on viscosity and mechanical properties of a commercial epoxy resin adhesive," *International Journal of Adhesion & Adhesives,* vol. 22, pp. 337-346, 2002.

[56] Omar Moussa, Anastasios P. Vassilopoulos, Julia de Castro, Thomas Keller, "Early-age tensile properties of structural epoxy adhesives subjected tolow-temperature curing," *International Journal of Adhesion & Adhesives,* vol. 35, 2012.

[57] W.K. Loh, A.D. Crocombe, M.M. Abdel Wahab, I.A. Ashcroft, "Environmental degradation of the interfacial fracture energy in an adhesively bonded joint," *Engineering Fracture Mechanics,* vol. 69, pp. 2113-2128, 2002.

[58] P. Daviesa, L. Sohier, J.-Y. Cognard, A. Bourmaud, D. Choqueuse, E. Rinnert and R.Créac'hcadec, "Influence of adhesive bond line thickness on joint strength," *International Journal of Adhesion and Adhesives,* vol. 29, pp. 724-736, 2009.

[59] Nimesh Jayakody, Ratneshwar Jha, Thomas E Lacy, "Damage Diagnostics of Composite Fan Blades Using The Modified Time Reversal Method," in *ASME 2015 Gas Turbine India Conference, American Society of Mechanical Engineers*, Hyderabad, India, 2015.

[60] K.B. Katnam, J.P.J.Stevenson,W.F.Stanley,M.Buggy,T.M.Young, "Tensile strengthoftwo-partepoxypasteadhesives:Influenceofmixing technique andmicro-voidformation," *International JournalofAdhesion&Adhesives,* vol. 31, 2011.

[61] Charles P. D. Todd and Richard E. Challis, "Quantitative Classification of Adhesive Bondline Dimensions Using Lamb Waves and Artificial Neural Networks," *IEEE TRANSACTIONS ON IJLTRASONICS, FERROELECTRICS, AND FREQUENCY CONTROL,* vol. 46, no. 1, 1999.

[62] Chenhui Su, Mingshun Jiang , Shanshan Lv, Shizeng Lu, Lei Zhang, Faye Zhang , and Qingmei Sui, "Improved Damage Localization and Quantification of CFRP Using Lamb Waves and Convolution Neural Network," *IEEE SENSORS JOURNAL,* vol. 19, 2019.

[63] Bo Feng , Dario Jerónimo Pasadas, Artur Lopes Ribeiro, and Helena Geirinhas Ramos, "Locating Defects in Anisotropic CFRP Plates Using ToF-Based Probability Matrix and Neural Networks," *IEEE TRANSACTIONS ON INSTRUMENTATION AND MEASUREMENT,* vol. 68, 2019.

[64] "trainbr - Bayesian regularization backpropagation," [Online]. Available: https://www.mathworks.com/help/deeplearning/ref/trainbr.html.

[1] Charles Farrar,Michael B. Prime, "Damage Identification and Health Monitoring of Structural and Mechanical Systems From Changes in their Vibration Characteristics: A literature Review," *The Shock and Vibration Digest,* 1996.

[2] Nimesh Jayakody, Ratneshwar Jha, Thomas E Lacy, "Damage Diagnostics of Composite Fan Blades Using the Modified Time Reversal Method," in *ASME 2015 Gas Turbine India Conference. American Society of Mechanical Engineers*, Hyderabad, India, 2015.

[3] V. Giurgiutiu, Structural Health Monitoring with Piezoelectic Wafer Active Sensors, Elsevier, 2008.

[4] V. Giurgiutiu, Structural Health Monitoring: with Piezoelectric Wafer Active Sensors, Elsevier, 2007.

[5] P.D. WILCOX, M.J.S. LOWE AND P. CAWLEY, "Mode and Transducer Selection for Long Range Lamb Wave Inspection," *JOURNAL OF INTELLIGENT MATERIAL SYSTEMS AND STRUCTURES,* vol. 12, 2001.

[6] zhongqing Su, Lin Ye, Ye Lu, "Guided lamb waves for identification of damage in composite structures: A review," *Journal of Sound and Vibration ,* vol. 295, pp. 753-780, 2006.

[7] Sang Jun Lee, Navneet Gandhi, Jennifer E. Michaels, and Thomas E. Michaels, "Comparison of the Effects of Applied Loads and Temperature," *Quantitative Nondestructive,* vol. 30, 2011.

[8] Ashkan Khalili, Ratneshwar Jha, and Nimesh Jayakody, "Structural Health Monitoring of Skin-Stiffener Structures Using WSFE-based User Defined Elements in Abaqus," in *25th AIAA/AHS Adaptive Structures Conference, AIAA SciTech Forum*, Grapevine, Texas, 2017.

[9] Nimesh Jayakody, Ratneshwar Jha, Ashkan Khalili and Dulip Samaratunga, "Assessment of Adhesively Bonded Joint Health Status using Wavelet Spectral Finite Element Method," in *25th AIAA/AHS Adaptive Structures Conference, AIAA SciTech Forum*, Grapevine, Texas, 2017.

[10] Nimesh Jayakody, Ratneshwar Jha and Dulip Samaratunga, "Wavelet Spectral Finite Element Modeling for Health Monitoring of Adhesively Bonded Joints," in *24th AIAA/AHS Adaptive Structures Conference, AIAA SciTech Forum*, San Diego, California, USA, 2016.

[11] M. Fink, "Time Reversal of Ultrasonic Fields-Part I: Basic Principles," *IEEE TRANSACTIONS ON ULTRASONICS, FERROELECTRICS,ANDFREQUENCYCONTROL,* vol. 39, no. 5, pp. 555-566, 1992.

[12] Francois Wu, Jean-Louis Thomas, and Mathias Fink, "Time Reversal of Ultrasonic Fields-Part 11:Experimental Results," *IEEE TRANSACTIONS ON ULTRASONICS, FERROELECTRICS, AND FREQUENCY CONTROL,* vol. 39, no. 5, pp. 567-578, 1992.

[13] Mathias Fink, Didier Cassereau, Arnaud Derode, Claire Prada, Philippe Roux, Mickael Tanter,Jean-Louis Thomas and Fran¸cois Wu, "Time-reversed acoustics," *Reports on Progress in Physics,* vol. 63, pp. 1933-1995, 2000.

[14] Hyun Woo Park, Seung Bum Kim, Hoon Sohn, "Understanding a time reversal process in Lamb wave propagation," *Wave Motion,* vol. 46, pp. 451-467, 2009.

[15] Ros K. Ing and Mathias Fink, "Time recompression of dispersive lamb waves using a time reversal mirror. Application to flaw detection in thin plates," in *1996 IEEE ULTRASONICS SYMPOSIUM*, 1996.

[16] Ros K. Ing and Mathias Fink, "Time-Reversed Lamb Waves," *ieee transactions on ultrasonics, ferroelectrics, and frequency control,* vol. 45, no. 4, pp. 1032-1043, 1998.

[17] L. R. F. Rose and C. H. Wang, "Mindlin plate theory for damage detection: Source solutions," *The Journal of the Acoustical Society of America,* vol. 116, no. 1, pp. 154-171, 2004.

[18] Chun H Wang, James T Rose and Fu-Kuo Chang, "A synthetic time-reversal imaging method for structural health monitoring," *SMART MATERIALS AND STRUCTURES,* vol. 13, p. 415–423, 2004.

[19] R. Gangadharan, C.R.L. Murthy, S. Gopalakrishnan, M.R. Bhat, "Time reversal technique for health monitoring of metallic structure using Lamb waves," *Ultrasonics,* vol. 49, pp. 696-705, 2008.

[20] Hoon Sohn; Hyun Woo Park; Kincho H. Law; and Charles R. Farrar, "Damage Detection in Composite Plates by Using an Enhanced Time Reversal Method," *JOURNAL OF AEROSPACE ENGINEERING,* vol. 20, no. 3, pp. 141-151, 2007.

[21] Buli Xu and Victor Giurgiutiu, "Single Mode Tuning Effects on LambWave Time Reversal with Piezoelectric Wafer Active Sensors for Structural Health Monitoring," *Journal of Nondestructive Evaluation,* vol. 26, pp. 132-134, 2007.

[22] Hyunwoo Park, Hoon Sohn and Kincho H. Law, "Damage Detection in Composite Plates by Using Time Reversal Active Sensing".

[23] Ryan Watkins and Ratneshwar Jha, "A modified time reversal method for Lamb wave based diagnostics of composite structures," *Mechanical Systems and Signal Processing,* vol. 31, pp. 345-354, 2012.

[24] Sang Jun Lee, Hoon Sohn and Jung-Wuk Hong, "Time Reversal Based Piezoelectric Transducer Self-diagnosis Under Varying Temperature," *Journal of Nondestructive Evaluation,* vol. 29, pp. 75-91, 2010.

[25] Lei Qiu, Shenfang Yuan, Xiaoyue Zhang and YuWang, "A time reversal focusing based impact imaging method and its evaluation on complex composite structures," *Smart Materials and Structures,* vol. 20, 2011.

[26] Wang Tao, Liu Shaopeng, Shao Junhua and Li Yourong, "Health monitoring of bolted joints using the time reversal method and piezoelectric transducers," *Smart Materials and Structures,* vol. 25, 2016.

[27] Yabin Liang, Dongsheng Li, Qingzhao Kong, and Gangbing Song, "Load Monitoring of the Pin-Connected Structure Using Time Reversal Technique and Piezoceramic Transducers—A Feasibility Study," *IEEE SENSORS JOURNAL,* vol. 16, no. 22, pp. 7958-7966, 2016.

[28] Guofeng Du1, Qingzhao Kong, Fanghong Wu, Jiabiao Ruan and Gangbing Song, "An experimental feasibility study of pipeline corrosion pit detection using a piezoceramic time reversal mirror," *Smart Materials and Structures,* vol. 25, 2016.

[29] Jian Cai, Lihua Shi, Shenfang Yuan and Zhixue Shao, "High spatial resolution imaging for structural health monitoring based on virtual time reversal," *SMART MATERIALS AND STRUCTURES,* vol. 20, 2011.

[30] Zenghua Liu, Hongtao Yu, Junwei Fan, Yanan Hu, Cunfu He and Bin Wu, "Baseline-free delamination inspection in composite plates by synthesizing noncontact air-coupled Lamb wave scan method and virtual time reversal algorithm," *Smart Materials and Structures,* vol. 24, 2015.

[31] "RSV-150 Remote Sensing Vibrometer," polytec, 30 May 2017. [Online]. Available: http://www.polytec.com/us/products/vibration-sensors/special-application-vibrometers/rsv-150-remote-sensing-vibrometer/.

[32] V. Giurgiutiu, Strucutral Health Montoring with Piezoelectric Wafer Active Sensor, Elsevier, 2008.

[33] Ryan Watkins and Ratneshwar Jha, "A modified time reversal method for lamb wave based diagnostics of compsite structures," *Mechanical Systems and Signal Processing,* vol. 31, pp. 345-354, 2012.

[34] "STEMiNC STEINER & MARTINS, INC," [Online]. Available: http://www.steminc.com/piezo/PZ_property.asp. [Accessed October 2015].

[35] Dulip Samaratunga, Ratan Jha, S. Gopalakrishnan, and A. Messac, "Wavelet spectral finite element modeling for wave propagation in adhesively bonded composite joints," in *23rd AIAA/ASME/AHS Adaptive Structures Conferance, AIAA Science and Technology Forum 2015*, Kissimme, Florida, 2015.

[36] Dulip Samaratunga, Ratneshwar Jha and S. Gopalakrishnan, "Wave propagation analysis in adhesively bonded composite joints using the wavelet spectral finite element method," *Composite Structures,* vol. 122, pp. 271-283, 2015.

[37] Louis C. (Lou) Dorworth and Dr. Giles Dillingham, *Fundamentals of Adhesive Bonding of Composite Materials,* Fort Worth, TX, 2017.

[38] M. J. Santos, J. Perdiga˜o, and P. Faia, "Ultrasonic Guided Waves Scattering Effects From Defects in Adhesively Bonded Lap Joints Using Pitch and Catch and Pulse-Echo Techniques," *The Journal of Adhesion,* vol. 84, pp. 421-438, 2008.

[39] Max Davis, *FAA Workshop on Best Practice in Adhesive Bonding.*

[40] W.H.Ong, N.Rajic, W.K.Chiu, C.Rosalie, "Adhesive material property evaluation for improved Lambwave simulation," *International Journal of Adhesion & Adhesives,* vol. 71, pp. 28-38, 2016.

[41] Juergen Koreck ,Christine Valle, Jianmin Qu and Laurence J. Jacobs, "Computational Characterization of Adhesive Layer Properties Using Guided Waves in Bonded Plates," *J Nondestruct Eval,* vol. 26, p. 97–105, 2007.

[42] M. R. Karim, A. K. Mal, and Y. Bar-Cohen, "Inversion of leaky Lamb wave data by simplex algorithm," *The Journal of the Acoustical Society of America,* vol. 88, 1990.

[43] Francesco Lanza Di Scalea, Howard Matt, Ivan Bartoli, Stefano Coccia, Gyuhae Park and Charles Farrar, "Health Monitoring of UAV Wing Skin-to-spar Joints using Guided Waves and Macro Fiber Composite Transducers," *Journal of Intelligent Material Systems And Structures,* vol. 18, pp. 373-388, 2007.

[44] Howard Matt, Ivan Bartoli, and Francesco Lanza di Scalea, "Ultrasonic guided wave monitoring of composite wing skin-to-spar bonded joints in aerospace structures," *Journal of Acoustical Society of America,* vol. 118, pp. 2240-2252, 2005.

[45] Camille Gauthie, Mounsif Ech-Cherif El-Kettani, Jocelyne Galy, Mihai Predoi, Damien Leduc, Jean-Louis Izbicki, "Lamb waves characterization of adhesion levels in aluminum/epoxy bi-layers with different cohesive and adhesive properties Adhesives," *International Journal of Adhesion and Adhesives,* vol. 74, pp. 15-20, 2017.

[46] Sun Hong-Xiang, Xu Bai-Qiang, Zhang Hua, Gao Qian and Zhang Shu-Yi, "Influence of adhesive layer properties on laser-generated ultrasonic waves in thin bonded plates," *Chin. Phys. B,* vol. 22, p. 014302, 2011.

[47] Wern Hann Ong, Nik Rajic, Wing Kong Chiu and Cedric Rosalie, "Lamb wave–based detection of a controlled disbond in a lap joint," *Structural Health Monitoring,* vol. 17, pp. 668-683, 2018.

[48] Yoji Okabe1, Junichiro Kuwahara, Kazuki Natori,Nobuo Takeda, Toshimichi Ogisu, Seiji Kojima and Shinji Komatsuzaki, "Evaluation of debonding progress in composite bonded structures using ultrasonic waves received in fiber Bragg grating sensors," *SMART MATERIALS AND STRUCTURES,* vol. 16, pp. 1370-1378, 2007.

[49] Fucai Li1, Hideaki Murayama, Kazuro Kageyama,Guang Meng, Isamu Ohsawa and Takehiro Shirai, "Debonding detection using a self-calibration sensor network," *SMART MATERIALS AND STRUCTURES,* vol. 19, 2010.

[50] Paul A. Cooper and James Wayne Sawyer, "Critical Examination of Stress in an Elastic Single Lap Joint," *NASA Tehcnical PAper 1507,* 1979.

[51] Tien-Cuong Nguyen, Yu Bai, Xiao-Ling Zhao, Riadh Al-Mahaidi, "Durability of steel/CFRP double strap joints exposed to sea water, cyclictemperature and humidity," *Composite Structures,* vol. 94, 2012.

[52] A.D. Crocombe, D.A. Bigwood and G. Richardson, "Analysing joints for structural adhesive failure," *INT.J.ADHESION AND ADHESIVES,* vol. 10, no. 2, 1990.

[53] L. TONG, "STRENGTH OF ADHESIVEL Y BONDED SINGLELAP AND LAP-SHEAR JOINTS," *1nl. J. Solids Struclure,* vol. 35, no. 20, 1998.

[54] M.S. Kafkalidis and M.D. Thouless, "The effects of geometry and material properties on the fracture of single lap-shear joints," *International Journal of Solids and Structures,* vol. 39, p. 4367–4383, 2002.

[55] Fabrice Lapique, Keith Redford, "Curing effects on viscosity and mechanical properties of a commercial epoxy resin adhesive," *International Journal of Adhesion & Adhesives,* vol. 22, pp. 337-346, 2002.

[56] Omar Moussa, Anastasios P. Vassilopoulos, Julia de Castro, Thomas Keller, "Early-age tensile properties of structural epoxy adhesives subjected tolow-temperature curing," *International Journal of Adhesion & Adhesives,* vol. 35, 2012.

[57] W.K. Loh, A.D. Crocombe, M.M. Abdel Wahab, I.A. Ashcroft, "Environmental degradation of the interfacial fracture energy in an adhesively bonded joint," *Engineering Fracture Mechanics,* vol. 69, pp. 2113-2128, 2002.

[58] P. Daviesa, L. Sohier, J.-Y. Cognard, A. Bourmaud, D. Choqueuse, E. Rinnert and R.Créac'hcadec, "Influence of adhesive bond line thickness on joint strength," *International Journal of Adhesion and Adhesives,* vol. 29, pp. 724-736, 2009.

[59] Nimesh Jayakody, Ratneshwar Jha, Thomas E Lacy, "Damage Diagnostics of Composite Fan Blades Using The Modified Time Reversal Method," in *ASME 2015 Gas Turbine India Conference, American Society of Mechanical Engineers*, Hyderabad, India, 2015.

[60] K.B. Katnam, J.P.J.Stevenson,W.F.Stanley,M.Buggy,T.M.Young, "Tensile strengthoftwo-partepoxypasteadhesives:Influenceofmixing technique andmicro-voidformation," *International JournalofAdhesion&Adhesives,* vol. 31, 2011.

[61] Charles P. D. Todd and Richard E. Challis, "Quantitative Classification of Adhesive Bondline Dimensions Using Lamb Waves and Artificial Neural Networks," *IEEE TRANSACTIONS ON IJLTRASONICS, FERROELECTRICS, AND FREQUENCY CONTROL,* vol. 46, no. 1, 1999.

[62] Chenhui Su, Mingshun Jiang , Shanshan Lv, Shizeng Lu, Lei Zhang, Faye Zhang , and Qingmei Sui, "Improved Damage Localization and Quantification of CFRP Using Lamb Waves and Convolution Neural Network," *IEEE SENSORS JOURNAL,* vol. 19, 2019.

[63] Bo Feng , Dario Jerónimo Pasadas, Artur Lopes Ribeiro, and Helena Geirinhas Ramos, "Locating Defects in Anisotropic CFRP Plates Using ToF-Based Probability Matrix and Neural Networks," *IEEE TRANSACTIONS ON INSTRUMENTATION AND MEASUREMENT,* vol. 68, 2019.

[64] "trainbr - Bayesian regularization backpropagation," [Online]. Available: https://www.mathworks.com/help/deeplearning/ref/trainbr.html.